DESIGN AND OPTIMIZATION OF MULTIPORT ELECTRICAL MACHINES AND SYSTEMS

JIANG MINGYUAN

PhD

The Hong Kong Polytechnic University

2024

The Hong Kong Polytechnic University

Department of Electrical and Electronic Engineering

Design and Optimization of Multiport Electrical Machines and Systems

JIANG Mingyuan

A thesis submitted in partial fulfillment of the requirements

for the degree of Doctor of Philosophy

01/2024

CERTIFICATE OF ORIGINALITY

I hereby declare that this thesis is my own work and that, to the best of my knowledge and belief, it reproduces no material previously published or written, nor material that has been accepted for the award of any other degree or diploma, except where due acknowledgment has been made in the text.

Signature:

Name of Student: JIANG Mingyuan

Abstract of dissertation entitled:

Design and Optimization of Multiport Electrical Machines and System

Submitted

by JIANG Mingyuan

for the degree of Doctor of Philosophy in

Electrical Engineering

at The Hong Kong Polytechnic University in (01/2024)

Abstract

Multiport electrical machines are widely utilized for energy distribution and combination, aiming to enhance overall efficiency, power factor, and speed/torque of transmission ports. These machines have gained increasing importance in transportation electrification and power generation due to their compact structure, design flexibility, and high efficiency. A comprehensive literature review is conducted, analyzing fundamental principles, advanced controlling strategies, and existing multiport topologies. The pros and cons of these topologies are evaluated, along with discussions on challenges and future trends. The review identifies two key research gaps: unsatisfactory torque performance and weaker flux controllability.

To improve torque performance, a novel brushless dual-electrical-port dual-mechanical-port machine (BLDDM) is proposed. This design incorporates high-order harmonic modulation, artificially enhancing the third-harmonic component of the airgap flux density in the inner airgap while maintaining the fundamental component in the outer airgap. Comparative analysis with conventional designs of the same dimensions demonstrates that the proposed BLDDM achieves a 50% higher back electromotive force (EMF) in the modulation winding and a 45.7% larger torque density. Experimental testing of a machine prototype validates the feasibility and advantages of the proposed design.

For reducing energy consumption in control windings and enhancing overall efficiency in Variable Speed Constant Frequency (VSCF) applications, a novel brushless dual-electrical-port dual-mechanical-port doubly fed machine (BLDD-

DFM) is developed. This design incorporates high-order harmonic modulation, amplifying the third-harmonic component in the inner airgap of the magnetomotive force (MMF) while maintaining the fundamental component in the outer airgap. By employing high-order harmonic modulation, the slip ratio is reduced, resulting in energy savings. Finite element analysis and comparative studies confirm the effectiveness of the proposed design, and a prototype further validates its feasibility and advantages.

To achieve improved flux weakening performance, a novel mechanical flux-weakening design for a spoke-type permanent magnet generator is proposed. This design allows effective adjustment of the total induced voltage and the amplitude of the back EMF vector sum by mechanically controlling the position of an adjustable modulator ring. Consequently, Variable Speed Constant Amplitude Voltage Control (VSCAVC) with a wide speed range can be achieved. Compared to the electrical flux weakening method, the mechanical approach offers easier operation without the risk of permanent magnet demagnetization. The proposed design is supported by an analytical model and operating principles, and performance analysis of different stator/rotor pole pair combinations using finite element methods demonstrates the characteristics of VSCAVC.

Finally, a novel hybrid excitation consequent-pole contra-rotating machine with zero-sequence current excitation is introduced to enhance flux weakening ability. This design involves stator windings carrying both the DC field winding current and the AC armature current, resulting in a more compact machine. The flux can be weakened or enhanced without the risk of demagnetization by controlling the zero-sequence current excitation in the integrated winding.

List of Publications

[1] **M. Jiang** and S. Niu*, “Novel Mechanical Flux-Weakening Design of a Spoke-Type Permanent Magnet Generator for Stand-Alone Power Supply,” *Applied Sciences*, vol. 13, no. 4, p. 2689, Feb. 2023, doi: 10.3390/app13042689.

[2] **M. Jiang** and S. Niu*, "A Novel Consequent-Pole Contra-Rotating Machine With Zero-Sequence Current Excitation," in *IEEE Transactions on Magnetics*, vol. 59, no. 11, pp. 1-5, Nov. 2023, Art no. 8101405, doi: 10.1109/TMAG.2023.3272952.

[3] **M. Jiang** and S. Niu*, "A High-Order Harmonic Compound Rotor Based Brushless Dual-Electrical-Port Dual-Mechanical-Port Machine," in *IEEE Transactions on Industrial Electronics*, vol. 71, no. 6, pp. 5463-5473, June 2024, doi: 10.1109/TIE.2023.3294574.

[4] **M. Jiang**, K. Zhao, W. Wang, and S. Niu*, “A Novel Brushless PM-Assisted DC Motor with Compound-Excited Circular Winding,” *Sustainability*, vol. 15, no. 18, p. 13924, Sep. 2023, doi: 10.3390/su151813924.

[5] **M. Jiang** and S. Niu*, "Overview of Dual Mechanical Port Machines in Transportation Electrification," in *IEEE Transactions on Transportation Electrification*, doi: 10.1109/TTE.2023.3324948. (Early access)

[6] W. Wang, S. Niu*, X. Zhao, **M. Jiang** and W. Fu, "A Novel Saturated Differential Inductance-based Position Estimation and Sensorless Startup Control of Non-salient DC Vernier Reluctance Machine," in *IEEE Transactions on Energy Conversion*, doi: 10.1109/TEC.2023.3339188. (Early access)

[7] **M. Jiang** and S. Niu*, " A High-Order-Harmonic Compound-Rotor Based Brushless Doubly-Fed Machine for Variable Speed Constant Frequency Wind Power Generation," in *IEEE Journal of Emerging and Selected Topics in Power Electronics*. (Under review)

[8] **M. Jiang**, S. Niu* and W. Wu, "Design and Analysis of a Novel Dual-Rotor Transverse Flux Permanent Magnet Machine," *IECON 2023- 49th Annual Conference of the IEEE Industrial Electronics Society*, Singapore, Singapore, 2023, pp. 1-6, doi: 10.1109/IECON51785.2023.10311826.

[9] W. Wu, S. Niu* and **M. Jiang**, "Design of a Novel Dual-Rotor Permanent Magnet Multiport Machine with C-Type Stator," *IECON 2023- 49th Annual Conference of*

the IEEE Industrial Electronics Society, Singapore, Singapore, 2023, pp. 1-6, doi: 10.1109/IECON51785.2023.10312670.

[10] W. Wu, S. Niu*, **M. Jiang** and Y. Wang, "Flux-Weakening Capability Enhancement of a Zero-Sequence Current Excitation Based Pole-Changing Permanent Magnet Machine," *2023 26th International Conference on Electrical Machines and Systems (ICEMS)*, Zhuhai, China, 2023, pp. 2739-2743, doi: 10.1109/ICEMS59686.2023.10344530.

[11] W. Wu, S. Niu*, **M. Jiang** and Y. Wang, "Design and Optimization of a Novel Flux Reversal Permanent Magnet Machine with DC Excitation Source," *2023 26th International Conference on Electrical Machines and Systems (ICEMS)*, Zhuhai, China, 2023, pp. 2765-2769, doi: 10.1109/ICEMS59686.2023.10344545.

Acknowledgments

The author would like to express his sincere gratitude to his chief supervisor, Professor Shuangxia Niu, for her invaluable expertise, patient guidance, innovative insights, and unwavering support throughout the duration of the author's doctoral studies. Prof. Niu's invaluable suggestions and words of encouragement have played a significant role in shaping the author's research. The opportunity to study and collaborate with Professor Niu has bestowed upon him an invaluable experience. Her unwavering commitment and dedication to research have left an indelible impression, serving as a perpetual source of inspiration throughout his academic and professional journey.

Additionally, the author wishes to express his heartfelt appreciation to all the PolyU EM Lab colleagues and Department of EEE staffs for their assistance. In particular, the author would like to acknowledge the contributions of Mr. Yanding Bi, Dr. Yuanxi Chen, Dr. Litao Dai, Mr. Ziqi Huang, Ms. Jiahui Huang, Dr. Zhenghao Li, Dr. Hongjian Lin, Mr. Yuxuan Liu, Dr. Yixiao Luo, Ms. Feifan Ni, Dr. Sigao Wang, Dr. Weiyu Wang, Dr. Yao Wang, Mr. Junkai Wen, Mr. H.T. Wong, Dr. Huihuan Wu, Mr. Wenjie Wu, Mr. Longfei Xiao, and Mr. Zhiwei Xue (listed in alphabetical order).

Lastly, the author wishes to express his deep appreciation to his family for their understanding and firm support throughout this academic journey. The author would also like to extend his thanks to Ms. Xiaohong Lu, his girlfriend, for her companionship and assistance in various aspects of his life.

- PER ASPERA AD ASTRA -

Table of Contents

List of Figures

List of Tables

Chapter 1 Introduction

1.1 Research Background

An electric machine is defined as an electric device used for the interconversion between electrical and mechanical energy [1]. Typically, a conventional electrical machine comprises a single electrical port (EP) and a single mechanical port (MP). The EP serves as the input/output (I/O) port for current and voltage, usually represented by the windings of the electric machine, while the MP serves as the I/O port for torque and angular speed, which generally refers to the rotor [2].

When an electric machine has more than one rotating part or winding, this machine is named a multiport machine. Due to the rapid development of power electronics and mechanical engineering in recent decades that have revolutionized the world's energy conversion systems, multiport machines like dual mechanical port (DMP) machines have been increasingly explored in recent days.

In particular, electrification is becoming an increasingly popular topic with increasing environmental protection concerns. This has accelerated development and implementation of multiport technologies in the field of transportation electrification, power generation, and other areas. Today, multiport machines can be widely used in various fields, including but not limited to electric continuously variable transmission (E-CVT) systems for hybrid electric vehicles (EVs), electric marine propulsion systems, electric aviation systems, and robotic actuators. Adopting the multiport topology in electric machines is generally for the following purposes:

1) To increase the overall efficiency and power factor.

2) To increase the torque density for direct drive applications.

3) To distribute or combine the energy from different ports flexibly.

The first multiport concept, i.e., the DMP concept was introduced in the 1920s to improve the performance of the induction motor (IM) [3]. However, at that time, the technology of rare-earth permanent magnet materials was not well developed, and the technology of electronic devices was quite primitive, making it challenging to control the DMP topology. As a result, the dual electrical port (DEP) machine, such as the doubly fed IM, was the main focus of the study.

Since the 1980s, PM material and power electronic technology has developed rapidly. In the 2000s, with the trend of hybrid electric vehicles (HEV) having become a hot spot, the study of multiport machines has gradually become popular because the multiport -based E-CVT system is more compact, which is most suitable for limited space in HEV. In [4], Eriksson and Sadarangani first developed the brushed four-quadrant transducer (4QT), to decouple the speed and torque of two mechanical ports. In [5], Xu first developed the concept of the machine and methodically analyzed the basic structures and operational principles of a sample multiport machine.

Also, with the emergence of magnetic gear around the beginning of the 21st century, flux modulation theory has been actively adopted in the design of multiport machines, which promotes the development of multiport technology. Using the modulation effect, various multiport structures have been designed, such as the pseudo direct-drive machine, bidirectional flux modulation machine, etc. [6, 7]. The applications of the multiport machines involved are not only limited to brushless E-CVT, wind power generation, etc. Extensive research has been conducted on different multiport topologies [8, 9].

1.2 Research Objectives

This thesis proposes novel multiport machine designs to improve the torque density and flux controllability. The objectives are:

- To develop a multiport machine with specialized outer rotor configuration and high order modulation to improve the torque density.
- To develop a multiport doubly fed machine with specialized outer rotor configuration and high order modulation to reduce the energy consumption in the control winding for variable speed constant frequency power generation.
- To design a multiport machine based on magnetic gear with good flux weakening by using mechanical method.
- To propose a multiport contra-rotating machine with extended speed range using one set of winding with zero-sequence-current.

1.3 Methodology

The methodology of this thesis is:

- To build accurate analytical model for each design to conduct preliminary fast computation.
- To analyze the no-load and on-load performances of the proposed designs by finite element method (FEM).
- To validate the analytical and FEM results through experiment results.

1.4 Thesis Outline

The thesis consists of 6 chapters, which is organized as follows.

In Chapter 2, the existed multiport machines' topologies and control methods are reviewed based on the power flow types from the perspective of DMP machines. By analyzing from fundamental principles to advanced controlling strategies, this paper aims to provide a comprehensive overview of existing multiport topologies. The pros and cons of all topologies are analyzed, and their challenges and future trends are discussed. The research gaps are found through the literature review.

In Chapter 3, a novel brushless dual-electrical-port dual-mechanical-port machine (BLDDM) using a high-order harmonic modulation is proposed to improve the torque density of BLDDMs. The key is that the compound outer rotor is artificially designed to enhance the third-harmonic component of airgap flux density in the inner airgap while remaining the fundamental component unchanged in the outer airgap. The presented BLDDM is optimized and compared with the conventional design with the same peripheral dimensions, which shows that the proposed design has 50% higher back EMF in modulation winding and 45.7% larger torque density. The machine prototype is tested, and the experimental results verify the feasibility and advantages of the proposed design.

In Chapter 4, a novel brushless dual-electrical-port dual-mechanical-port doubly fed machine (BLDD-DFM) that incorporates high-order harmonic modulation to reduce the energy consumption in the control winding is proposed for variable speed constant frequency (VSCF) applications. By employing high-order harmonic modulation, the slip ratio can be reduced, resulting in energy savings.

In Chapter 5, a novel mechanical flux-weakening design of a spoke-type permanent magnet generator for a stand-alone power supply is proposed. By controlling the position of the adjustable modulator ring mechanically, the total induced voltage, i.e., the amplitude of the back EMF vector sum can be effectively adjusted accordingly by the modulation effect. Consequently, the variable-speed constant-amplitude voltage control (VSCAVC) with a large speed range can be achieved. Compared to the electrical flux-weakening method, the mechanical flux-weakening method is easier to operate without the risk of PM demagnetization. The analytical model is presented, and the operation principles are illustrated. To analyze the performance of different combinations of stator/rotor pole pairs, four cases are optimized and analyzed using the finite element method for comparison. The characteristics of VSCAVC are analyzed.

In Chapter 6, a novel hybrid excitation consequent-pole contra-rotating machine with zero-sequence current excitation is presented in this paper. The stator windings carry both the DC field winding current and the AC armature current, making the machine more compact. Further, the flux can be weakened or enhanced without the risk of demagnetization by controlling the zero-sequence current excitation in the integrated winding. Finally, the segmented stator can effectively reduce iron loss and simplify the manufacture processing.

In Chapter 7 , the conclusions are made, and the future work of the multiport machines' study are planned.

Chapter 2 Literature review

Fig. 2-1 shows the power flow model of the multiport system. The model of a multiport machine consists of two MPs and one or more EPs. MPs can be regarded as the rotors and EPs can be regarded as the stator windings.

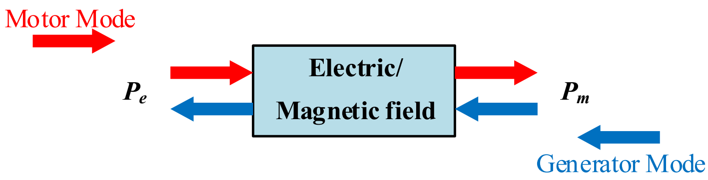

Fig. 2-1. The general power flow and operation modes of the multiport machine.

Generally, in motor mode, the electrical source inputs electrical power (P_e) into the EP. During electromagnetic conversion, MPs deliver mechanical power (P_m) to drive the mechanical load, which is shown in the red arrows in Fig. 2-1. Similarly, the power flow in the generator mode is shown in blue arrows.

As multiport machine involves both single-electrical-port dual-mechanical-port (SEP-DMP) type and dual-electrical-port dual-mechanical-port (DEP-DMP) type, for easy classification, the literature review is given from the perspective of DMP machines.

2.1 Machine Classification

Based on the power flow relationships between the EP and two MPs, DMP machines can be classified into the following three main categories, shown in Fig. 2-2:

1) Series power flow (SPF) type machines, where two MPs and the EPs are connected in series, and the energy transfer between all ports is

unidirectional.

2) Parallel power flow (PPF) type machines, where two MPs are parallelly connected to the EPs, and the energy transfer between all ports is unidirectional.

3) Hybrid power flow (HPF) type machines, where two MPs are parallelly connected to the EPs, and the energy transfer between certain ports is bidirectional.

The following sections will discuss the categories mentioned above in detail.

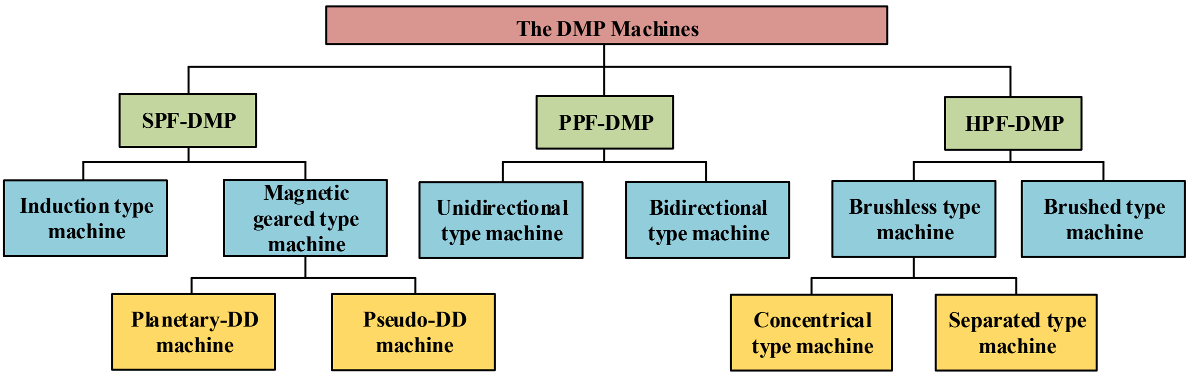

Fig. 2-2. The classification of the DMP machines.

The following sections will discuss the categories mentioned above in detail.

2.2 Series Power Flow Type DMP Machines

Fig. 2-3 shows the model of the SPF-DMP machine, where the EP and two MPs are connected in series. For the SPF-DMP machine, an MP is used as the idle rotor, namely the free rotating rotor, which transfers the energy to the input/output rotor. The input/output rotor, namely the I/O rotor, is connected to the shaft. In Fig. 3, the idle rotor is MP_1 and the I/O rotor is MP_2. As this type of DMP machine only has one MP adopted for the mechanical energy output or input, its function is generally similar to a conventional single mechanical port machine.

The idle rotor is generally used as a cascade bridge for the following purposes:

1) To improve the power factor and efficiency;

2) To transfer the torque.

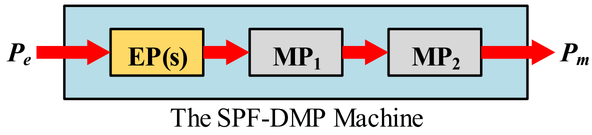

(a)

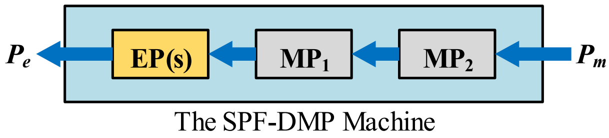

(b)

Fig. 2-3. The model of the SPF-DMP machine. (a) Motor mode. (b) Generator mode.

Different types of machines are used to realize the various functions of the idle rotor, so the SPF-DMP machine can be further classified into the following two subcategories: induction type and magnetic-geared type. The corresponding characteristics are briefly presented in Table 2-1 and will be discussed in detail in the following session.

Table 2-1. Comparison of the SPF-DMP machines

Item	**SPF-DMP-IM**	**SPF-DMP-MGM**
Topology	• One squirrel-cage I/O rotor, one PM-excited idle rotor • One stator	• One PM-excited I/O rotor, one PM-excited idle rotor • One or more stators
Merits	• Higher power factor than conventional IM • Higher efficiency than conventional IM • Equal performance as the PMSM	• Amplifying the torque for motor mode • Increasing the rotating speed of the magnetic field for generator mode • High torque density and power density
Weakness	• More complex manufacturing process than the PMSM	• More complex manufacturing process than the single MP machine

2.2.1 Induction Type SPF-DMP Machine

For the SPF-DMP induction machine (IM), the I/O rotor is usually a squirrel-cage IM rotor. The idea is to improve the power factor and the efficiency of the IM by reducing the magnetizing current, which is achieved by using an additional idle rotor for field excitation. The equivalent circuit is shown in Fig. 2-4. Compared with the equivalent circuit of conventional IM, an extra field excitation source (E_s) can be found in the magnetizing branch for SPF-DMP-IM. The relationships between speed and pole pair number are as follows:

$$\begin{cases} p_a\omega_a = p_1\omega_1 = p_2\omega_2 \\ p_a = p_1 = p_2 \end{cases} \tag{2-1}$$

where p_a, p_1, p_2 are the pole pair number of the stator winding, idle rotor (MP1), and I/O rotor (MP2), respectively, whereas ω_a, ω_1, and ω_2 are the synchronous speed of stator winding, idle rotor, and I/O rotor.

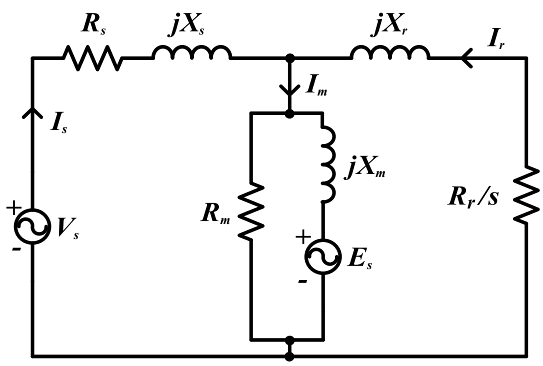

Fig. 2-4. Equivalent circuit of SPF-DMP-IM [10].

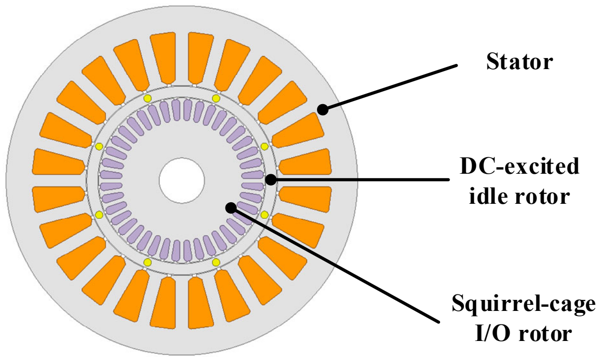

Fig. 2-5. The SPF-DMP-DCIM [3].

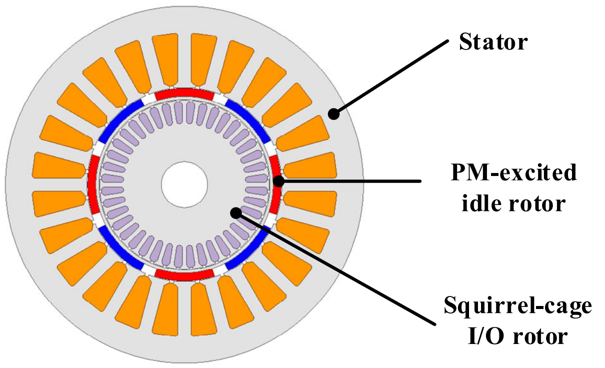

(a)

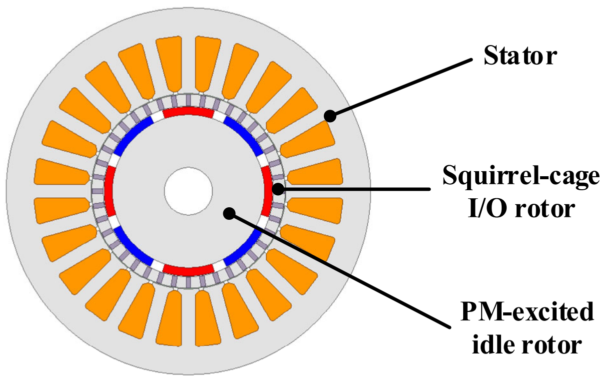

(b)

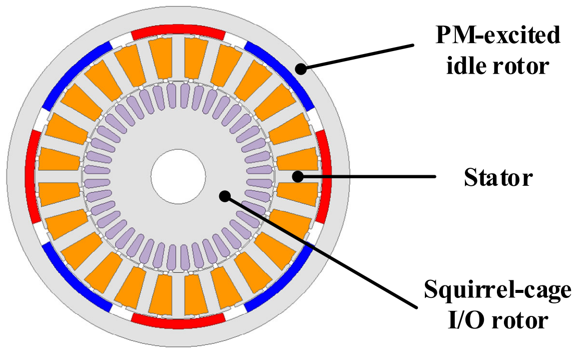

(c)

Fig. 2-6. Three topologies of the SPF-DMP-PMIM.

Punga and Schoen proposed the first single-phase DC induction motor (DCIM) with an idle rotor and DC exciting winding in [3], shown in Fig. 2-5. However, the use of commutators and brushes required for the DC exciting winding is not reliable and requires constant maintenance. To address this issue, the use of permanent magnets (PMs) instead of the DC exciting winding is proposed, resulting in the PM induction motor (PMIM) [10, 11]. Early PMIM designs utilized ferrite and Alnico PMs, which have low energy and are prone to demagnetization. However, modern high-energy PMs have been developed, and a single-phase PMIM with such PMs has been proposed [12]. The placement of the idle rotor in PMIM can be between the stator and the I/O rotor, inside the I/O rotor, or outside the stator, shown in Fig. 2-6. The influence of PM and core material on PMIM performance has been investigated, with PMIM found to have slightly higher efficiency, torque density, and power density than PMSM of the same size and material [13]. Design methods based on analytical approaches have also been investigated for improved PMIM design [14, 15].

The characteristics of the SPF-DMP-IM are summarized as below:

4) The SPF-DMP-IM uses an additional idle excited rotor as an extra field

excitation source in the magnetizing branch to reduce magnetizing current, which improves power factor and efficiency.

5) Early SPF-DMP-DCIM needs commutators and brushes for the winding, which requires constant maintenance.

6) SPF-DMP-PMIM has slightly higher efficiency, torque density, and power density than PMSM of the same size and material, but the structure is more complex.

2.2.2 Magnetic Geared Type SPF-DPM Machine

In the SPF-DMP magnetic geared machine (MGM), the idle rotor operates at high speed and low torque and the I/O rotor operates at low speed and low torque. A stationary modulation ring is placed between the idle rotor and the I/O rotor or between the idle rotor and the stator, based on the different operating principles.

The SPF-DMP MGM can be considered as a combination of the PMSM part and the MG part. The PMSM part includes the stator and idle rotor. The MG part includes the idle rotor, the modulation ring and the I/O rotor [16]. The energy of two parts is transferred through the idle rotor in a cascade.

This type of machine utilizes the flux modulation principle, also known as the magnetic gear effect [17]. A magnetic gear structure consists of three components: the small-pole-pair magnetic field, the modulation segments, and the large-pole-pair magnetic field. In general, two magnetic fields are excited by permanent magnets with different pole pairs on two rotors. The stable torque between these three components can only be generated when certain relationships are met:

$$p_{spp} = n_k - p_{lpp} \tag{2-2}$$

where n_k, p_{spp} and p_{lpp} are the number of modulation segments, the pole pair number of the small-pole-pair magnetic field and the large-pole-pair magnetic field, respectively. The speed and torque relationship can be expressed as

$$\begin{cases} p_{spp}\Omega_{spp} = n_k\Omega_k - p_{lpp}\Omega_{lpp} \\ T_{spp}\Omega_{spp} = T_k\Omega_k - T_{lpp}\Omega_{lpp} \end{cases} \tag{2-3}$$

where Ω_{spp}, Ω_k and Ω_{lpp} are the mechanical rotation speeds of the small-pole-pair magnetic field, the modulation segments and the large-pole-pair magnetic field, T_{spp},T_k and T_{lpp} are the torque generated by the small-pole-pair magnetic field, the modulation segments and the large-pole-pair magnetic field, respectively.

Generally, the magnetic field with a small pole pair is excited by the PMs on the idle rotor. The I/O rotor can be the rotor with a large pole pair number of PMs or the modulation ring, depending on the machine type. As the MG is just a gear structure without an energy source, the armature winding functions as the prime mover to drive one of the rotors, usually the idle rotor. The relationships of the idle rotor and the armature can be expressed as

$$\begin{cases} p_{spp} = p_a \\ p_{spp}\Omega_{spp} = p_a\omega_a \end{cases} \tag{2-4}$$

where p_a and ω_a are the pole pair number and the angular speed of the armature winding. The stator, winding and MG form the magnetic-gear machine (MGM).

2.2.2.1 Planetary direct-drive SPF-DPM MGM

Fig. 2-7 shows the planetary direct drive type configuration. The idle rotor has PMs on both sides. The modulation ring is placed between the I/O rotor and the idle rotor and forms the MG part with them. The I/O rotor is the PM outer rotor, i.e. the rotor with a large pole pair number. The modulation ring is stationary, that is, $\Omega_k = 0$. Based on that, (2-3) can be modified as

$$\begin{cases} p_{spp}\Omega_{spp} = -p_{lpp}\Omega_{lpp} \\ T_{spp}\Omega_{spp} = -T_{lpp}\Omega_{lpp} \end{cases} \tag{2-5}$$

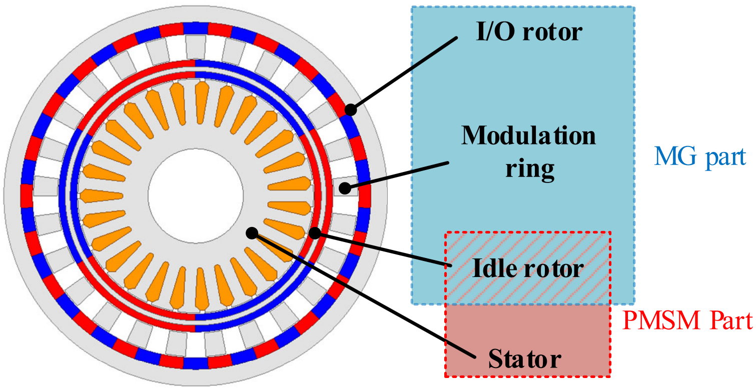

Fig. 2-7. Planetary direct-drive type SPF-DPM-MGM [18].

The operating principle is quite straightforward: the stator winding drives the idle high-speed rotor like a conventional PMSM. After interacting with the modulation ring, the idle rotor then transfers power to the low-speed I/O rotor. The magnetic gearing effect decreases the rotating speed but amplifies the torque, thus improving the overall torque performance compared to conventional PMSM.

In [18], the planetary-type configuration is proposed and suggested to be applied to electric vehicles, with the aim of replacing the gear mechanism and perform direct drive within the limited volume. The 2D FEM shows that this topology can reach a high torque density, around 87 kNm/m^3. However, both designs have the problem that the iron core of the idle rotor is highly saturated, which means that the magnetic field of the PMSM part and the MG part are coupled.

To overcome this issue, an improved version of the planetary model, named the motor-integrated PM gear (MIPMG), is proposed in [19]. By adjusting the PM thickness of the idle rotor, the PMSM part and the MG part of the MIPMG can be magnetically decoupled, which enables the new design to have better flux weakening abilities while the high torque density remains. An experimental evaluation is conducted in [20] and it was found that the rotationally dependent losses were quite excessive, and the solution by modifying the key components (such as the structure of modulation ring) is proposed in [19], where the new model is named MIPMG v.2. In [21], MIPMG v.2 is applied in battery electric vehicles and its experimental data were analyzed, demonstrating that loss is reduced and torque density is improved, namely 99.7 kNm/m^3. Recently, MIPMG has been applied to the conveyor system to replace the conventional system formed by IM and the gearbox [22]. Several topologies are proposed, in which the semi-integrated topology is finally selected and measured at around 142 kNm/m^3.

The planetary direct-drive type model has quite potential performance, but almost no commercial application has yet appeared. The reason may be its manufacturing difficulty (coaxial structure with three airgaps) and its high loss at high speed.

2.2.2.2 Pseudo-direct-drive SPF-DPM MGM

Fig. 2-8 shows a typical pseudo-direct-drive (PDD) type configuration, where the I/O rotor is the modulation ring, which is placed between the stator and the idle rotor. Unlike the planetary-direct-drive type, for the MG part of the pseudo-direct-drive type model, the stationary parts are the PMs with a large pole pair number on the stator, i.e., $\Omega_{lppn} = 0$. On the basis of that, (2) can be modified as

$$\begin{cases} p_{spp}\Omega_{spp} = n_k\Omega_k \\ T_{spp}\Omega_{spp} = T_k\Omega_k \end{cases} \tag{2-6}$$

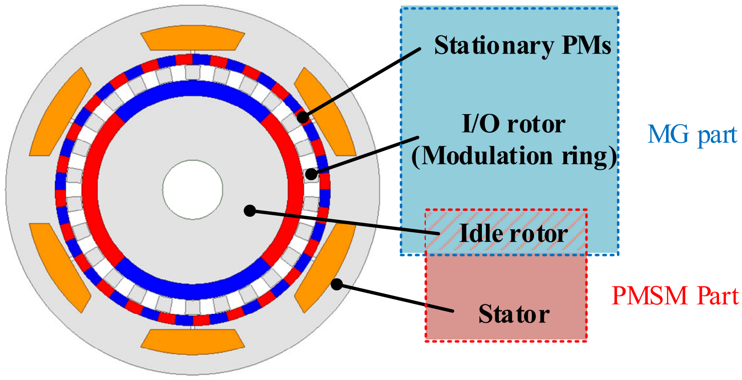

(a)

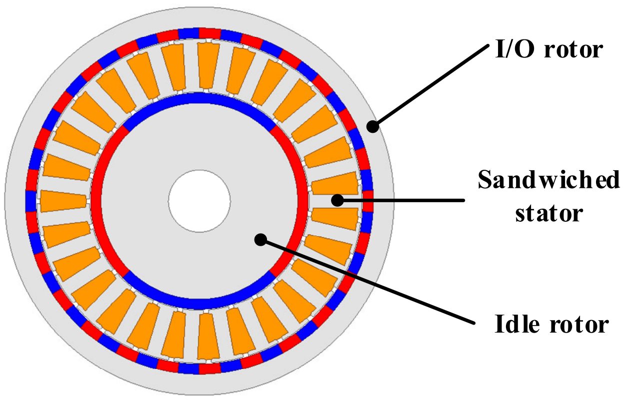

(b)

Fig. 2-8. Pseudo-direct-drive type SPF-DPM-MGM. (a) Outer stator type [23]. (b) Sandwiched stator type [24, 25].

The operating principle is as follows: the stator winding interacts with the PMs on the idle rotor in the innermost. The idle rotor then interacts with the stationary PMs and transfers the power to the I/O rotor. Based on (5), the torque of the I/O rotor is also amplified.

The first PDD machine shown in Fig. 2-8(a) is proposed in [6]. A prototype was made and tested, showing that the PDD machine has a high torque density (>60 kNm/m ^{3}) and high power factor (>0.9). The PDD machine with the V-shaped idle rotor for robustness is proposed in [26] for ship propulsion. However, because PMs are mounted at the tip of the teeth, which increases the air gap between the stator and the idle rotor, the torque generated by the stator winding is relatively low. To overcome this problem, a new structure is proposed, whose winding is arranged on the stationary modulator, between the idle rotor and the I/O rotor, namely the sandwiched-stator type PDD machine, in [24, 25], shown in Fig. 2-8(b). Alternatively, a new type of PDD machine is proposed in [27], whose PMs are mounted only on the idle rotor. The FEM results showed that the torque generated by the winding increases, but the overall torque decreases as the total amount of PM decreases. Later, this topology was improved by adding PMs to the opening of the stator slot, which turned out to have better performance in low-speed high-torque applications [28]. To reduce PM mass, a PDD machine with a DC-excited idle rotor is proposed, which also has better excitation controllability [29]. A technique for PDD machines with alternative windings is proposed [30], which shows that overall integrity improved with a slight decrease in torque density compared to [23].

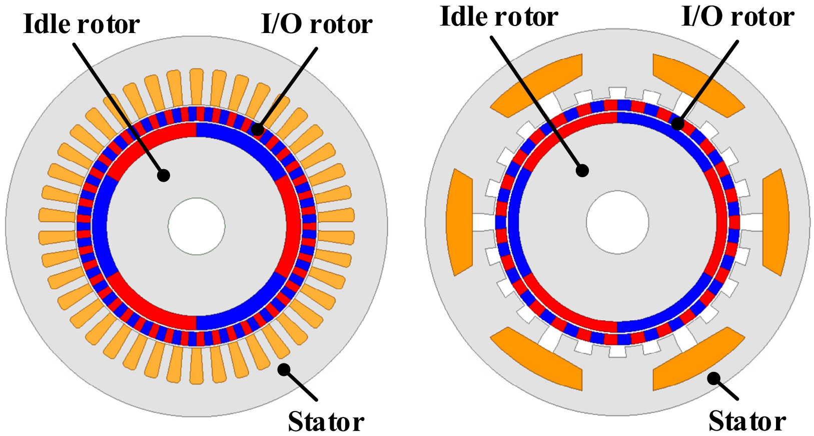

(a) (b)

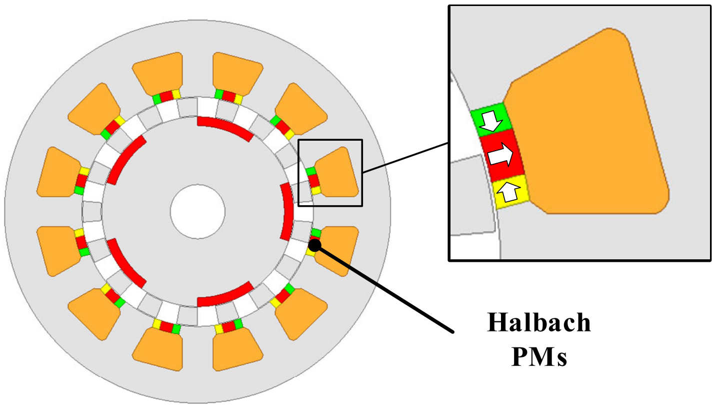

(c)

Fig. 2-9. The variants of PDD machine. (a) Vernier PDD machine[31]. (b) Split-tooth VPDD machine [32]. (c) VPDD machine with Halbach array [33].

Based on the original PDD machine in [23], many variants have been designed. A linear PDD machine is proposed to improve efficiency and power density [34]. Another kind of variant is vernier PDD (VPDD) machine. Vernier machine is developed from the magnetic gear. For the vernier machine, the small-pole-pair magnetic field is excited by the stator winding and the large-pole-pair magnetic field is excited by PMs on the rotor. The pole pair number of the modulation segments is usually one or several times of the stator slots. Since the modulation segments are stationary, they can be attached directly to the stator teeth. The relationship can be summarized as

$$\begin{cases} n_k = kZ, k = 1,2,3 \ldots \\ |n_k - p_r| = p_a \\ p_a \omega_a = p_r \Omega_r \end{cases} \tag{2-7}$$

where Z is the number of stator slots, p_r and Ω_r are the pole pair number and the rotation speed of the rotor.

In [31], the VPDD machine is proposed, whose I/O rotor is a PM ring, shown in Fig. 2-9(a). For the machine in [33], the stator teeth and the I/O rotor form a vernier machine. The VPDD machine has a high torque density (91.8 kNm/m ^{3}), low torque ripple (0.08%) and high power factor (0.94). Later, the author noticed that the amount of PM usage is high for VPMM, so the VPDD machine with the split-tooth stator is then designed to reduce overall PM usage. Split-tooth design can remain the high power factor, with a slight decrease in torque density [35]. [32] followed the study of [35] and proposed the split-tooth VPDD machine with the concentrated coil and optimized with the goal of high torque per coil length, which is shown in Fig. 2-9(b). [33] also followed the work in [31] and further improved the torque density to 137.4 kNm/m^3 by applying the Halbach PM structure on the idle rotor. In [36], the Halbach PM arrays are applied in the opening of the stator slot and the consequent pole structure is applied in the idle rotor, which can have the same performance as [33], shown in Fig. 2-9(c).

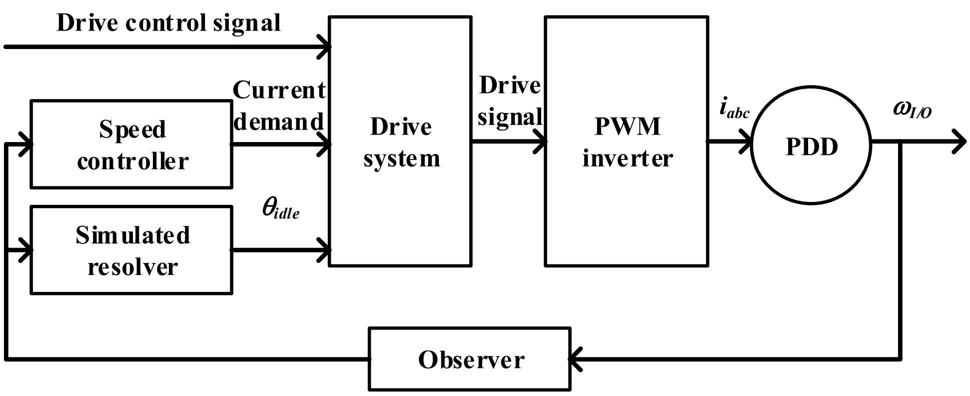

Fig. 2-10. Schematic of close-loop speed control system of PDD machine using only I/O rotor sensor [37].

For the controlling aspect of the PDD machine, because it lacks damping in the system, conventional field oriented control (FOC) is not suitable, as there is a torsional oscillation between the idle rotor and the I/O rotor. Full-state feedback control based on observed feedback is proposed to overcome this issue in [38], which turned out to be effective but difficult to adjust state feedback gains for better performance. In [39], a state feedback controller with a reduced-order observer tuned by the genetic algorithm (GA) is proposed. The author further proposed a novel technique to control the PDD machine with a single quipped sensor on the I/O rotor, shown in Fig. 2-10, which achieves the same effect as two sensors and greatly simplified the construction, since the idle rotor is difficult to equip the sensor due to its innermost position [37].

The characteristics of the SPF-DMP-MGM are summarized as below:

1) The planetary direct-drive type SPF-DMP-MGM uses an idle rotor with PMs on both sides and a modulation ring between the I/O rotor and the idle rotor to improve torque performance compared to conventional PMSM.

2) The motor-integrated PM gear (MIPMG) overcomes the issue of highly saturated iron core in the idle rotor by magnetically decoupling the PMSM part and the MG part, resulting in better flux weakening abilities and high torque density.

3) The pseudo-direct-drive (PDD) type SPF-DMP-MGM places the I/O rotor as the modulation ring between the stator and the idle rotor and has been developed into many variants with different structures and PM configurations to improve performance in low-speed high-torque applications.

4) To overcome the issue of torsional oscillation between the idle rotor and the I/O rotor, various techniques for full-state feedback control, state feedback control with reduced-order observer tuned by the genetic algorithm, and single-sensor-based control have been proposed for the PDD machine.

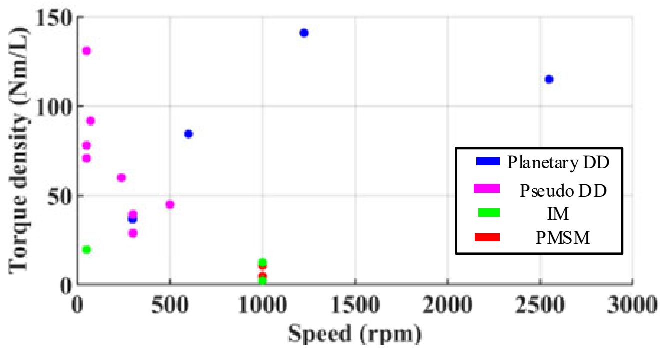

Fig. 2-11. Distribution of the SPF-DMP machines in torque density and speed.

Fig. 2-11 summarizes the torque densities per volume and rotary speeds of different SPF-DMP machines at rated condition in [13-15, 18-20, 22, 23, 28, 31-33, 36]. As shown in Fig. 2-11, the induction type is about equivalent torque density as the conventional PMSM. Because there is only one airgap between the stator and the idle rotor, and there is a complete magnetic gear structure, the planetary direct-drive type structures are applied in HEVs due to the high speed and high torque density. The PDD structures have two airgaps, which can be applied in ships or EVs with direct drive motor because they require high torque density rather than high speed. As seen from the present research results, the PDD structure is the most promising SPF-DMP topology due to its relatively simple structure, high torque density, and high power factor.

2.3 Parallel Power Flow Type DMP Machines

Fig. 2-12 shows the model of the PPF-DMP machine. Two MPs are parallelly connected to the EP through the electromagnetic field. Both MPs work as I/O rotors, which are connected to mechanical loads or sources directly. On the basis of the relative rotating directions of two MPs, the PPF-DMP machine can be further divided into the following two subcategories: the unidirectional (UD) type and the bidirectional (BD) type. Their characteristics are briefly listed in Table II.

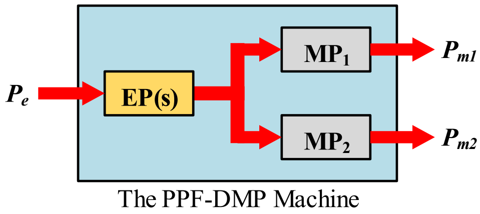

(a)

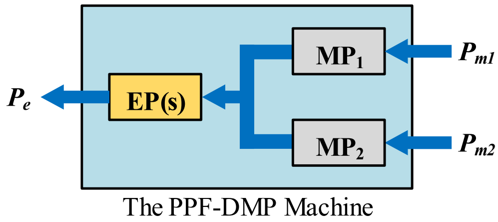

(b)

Fig. 2-12. The model of the PPF-DMP machine. (a) Motor mode. (b) Generator mode.

Table 2-2. Comparison of the PPF-DMP machines

Item	PPF-DMP-UDM	PPF-DMP-BDM
Topology	• One stator sandwiched by two rotors with the same speed • With, or without PMs on the rotors • One electrical port	• Two rotors with the same or different speed • With PMs on the rotors • One or more electrical port.
Merits	• High torque density and power density	• High efficiency for the propulsion system • Increase the frequency for direct-drive wind turbines
Weakness	• Complex manufacturing process for cup-shaped double rotor structure	• Complex manufacturing process • Special consideration of the interaction between two electrical ports

2.3.1 Unidirectional Type PPF-DMP Machine

The topology of the dual rotor radial flux toroidally wound UD machine (UDM) is proposed in [40], shown in Fig. 2-13. The author later presented its design procedure and optimization method in [41]. This topology can be regarded as the combination of two separate PM machines because the magnetic flux paths of two MPs are in parallel, shown in the bottom right corner of Fig. 2-13. The purpose of using the toroidal coil is to effectively reduce the length of the end winding, thus reducing the copper loss and improving the efficiency. The toroidal coil is later widely used for this type of machine. The comparison between the radial flux type and the axial flux type is presented further in [42] through FEM. The results show that both types have similar performances, but the radial flux type has a higher power loss per airgap area and the axial flux type has a higher material cost due to the additional PMs needed. The effects of different parameters on performance are presented in [43], and the design guideline based on that is given.

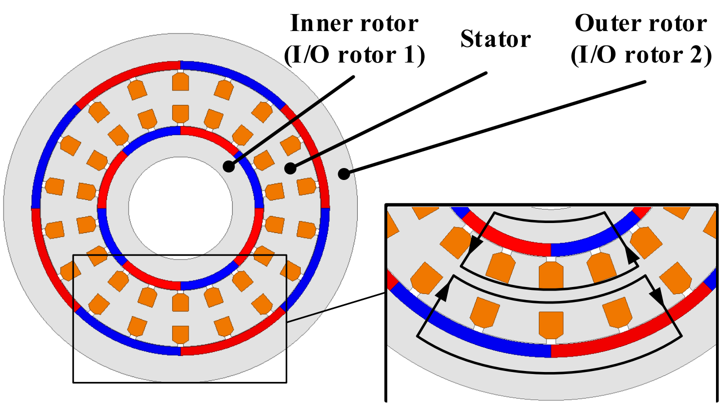

(a)

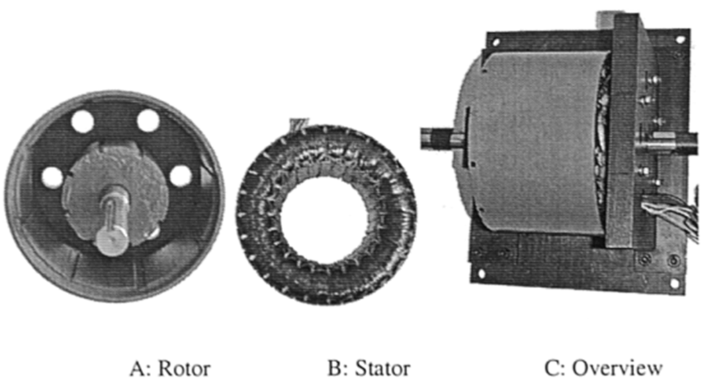

(b)

Fig. 2-13. Dual-rotor radial-flux toroidally-wound PPF-DMP-UDM and its parallel flux path [40]. (a) Machine configuration. (b) Prototype.

In [44], a UDM is presented whose two rotors are separated. In this topology, two sets of radial winding are used to control two MPs independently. In [45], a Halbach version of the separate-rotor UDM is proposed, which shows an improvement of 16% in torque density compared to the non-Halbach version. An equivalent design method is presented in [46] by splitting the machine into two parts based on magnetic paths and individually calculating the performance of each part.

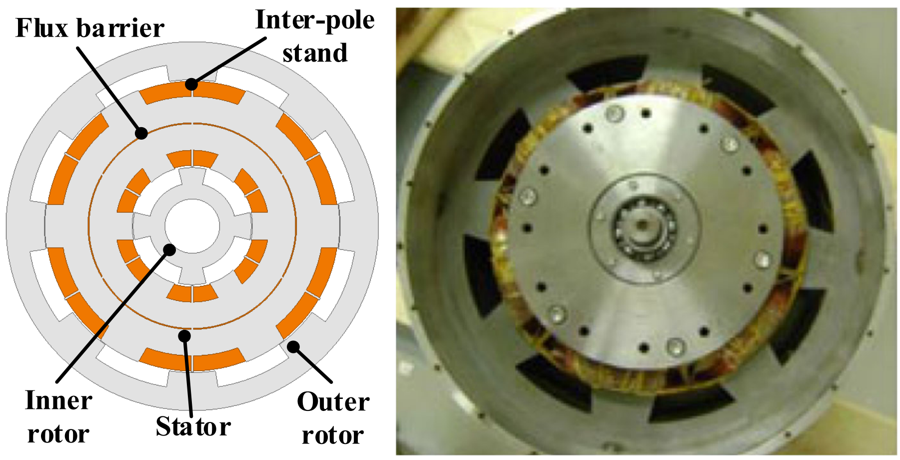

(a)

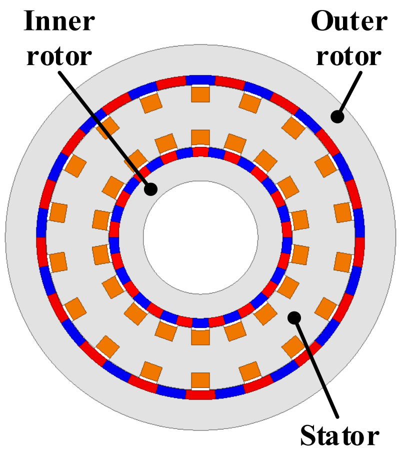

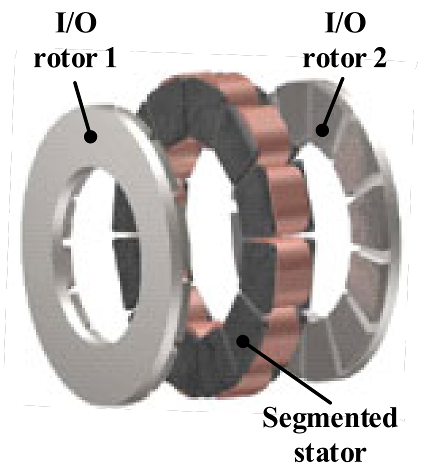

(b) (c)

Fig. 2-14. Variants of the original PPF-DMP-UDM. (a) SRM and its prototype [47]. (b) VM [48]. (c)YASAM [49].

Based on the aforementioned UDM, several kinds of variant topologies are designed. The first type is the switched reluctance machine (SRM), which has the feature of being robust and free-PM and greatly reducing the cost of the material. The rotors are of salient-pole structure. In [50], the UD-SRM with axial-flux toroidal winding is presented, which showed a high fault tolerant capability. A radial-flux UD-SRM with two sets of radial windings for individual control of two rotors is presented in [47], shown in Fig. 2-14(a).

The second variant is the UD vernier machine (VM). In [48], the UD-VM with the toroidal winding and open slot structure is proposed, which is shown in Fig. 2-14(b). The UD-VM is compared with single rotor VM and double stator VM, whose results verified its advantageous performances. A dual-PM UD-VM is proposed based on [48], which further magnifies the torque by the modulation effect of the dual-PM structure [51]. In [52], a UD-VM axial flux is proposed and a quasi-3D method is proposed to shorten the calculation time of the FEM.

The last type is the axial-flux yokeless and segmented armature machine (YASAM). This topology was first proposed in [49], which is shown in Fig. 2-14(c). Unlike previous types, whose magnetic paths of two MPs are in parallel, the magnetic path of two rotors for the YASA type is in series, which makes the common yoke of the stator unnecessary. Thus, the common stator yoke is removed and segmented. This structure significantly shortens the flux path for axial-flux machines and reduces the stator iron loss due to the segmented structure, which makes this type of machine have high efficiency and torque density. However, the YASAM has the problem of overheating. In [53], the air cooling of the YASA machine is investigated, and the author proposed the structure of the aluminium heat transfer fin, which can increase 40% in terms of the achievable continuous current density. In [54], the UD-YASA with Halbach array is proposed for further improvement of the torque density. Its optimization methods are given, which have been proven to be fast and accurate enough. YASAM is commercially produced for electric vehicles.

The characteristics of the PPF-DMP-UDM are summarized as below:

1)The dual rotor radial flux toroidally wound UDM is proposed as a combination of two separate PM machines, with toroidal coil used to reduce the length of the end winding, copper loss, and improve efficiency.

2)Among all variants, YASAM has high efficiency and torque density due to its segmented stator structure, which is commercially produced for EVs, but overheating is a problem. The air cooling and the aluminum heat transfer fin are proposed to improve its continuous current density.

2.3.2 Bidirectional Type PPF-DMP Machine

As the BD machine (BDM), also known as the contra-rotating structure, has been found to have a higher efficiency for fluid turbines than the UD structure, the PPF-DMP-BDM has gradually become an interesting research topic [55]. The PPF-DMP-BDM is generally used for marine propulsion.

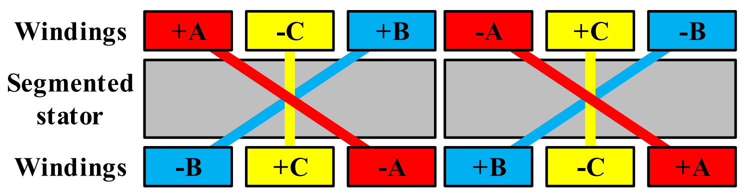

Fig. 2-15. The PPF-DMP-BD-WC machine [56].

The topology is first proposed in [56], shown in Fig. 2-15. In this topology, the pole-pitch-segmented stator is sandwiched and shared by two contra-rotating rotors. The operating principle is quite simple: for a three-phase machine, by swapping two phases' positions while remaining one phase unchanged, the amplitude of the magnetic field for two rotors remains the same, but the rotating direction become opposite, thus the contra-rotation is achieved. This can be regarded as two contra-rotating PMSMs that share the same stator yoke [57]. An optimized vector control method with load torque observer compensation is proposed in [58] for the axial-flux BD-WC machine, which realized the simultaneous control of dual rotor and can eliminate torque and speed tipple under heavy unbalanced loads. Its control diagram is shown in Fig. 2-16.

A BD-WC machine with no segmented radial flux is analyzed in [59], where the flux density of the outer airgap is greater than that of the inner air gap. In [60], a BD-WC machine with an all-segmented stator and two non-segmented stators is proposed. The author later analyzed the inter-rotor interaction through the common stator core in [61] and found that this interaction improved the back EMF.

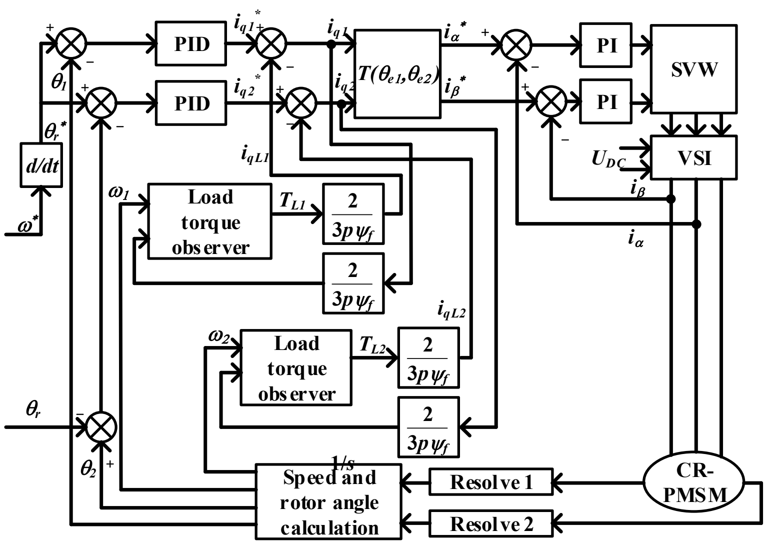

Fig. 2-16. Control diagram of the axial-flux PPF-DMP-BD-WC machine [58].

The characteristics of the PPF-DMP-BDM are summarized as below:

1)The BDM has higher efficiency for fluid turbines than the UDM and the PPF-DMP-BDM has become an interesting research topic, generally used for marine propulsion.

2)The operating principle involves swapping two phases' positions while remaining one phase unchanged to achieve contra-rotation, resulting in two contra-rotating PMSMs sharing the same stator yoke.

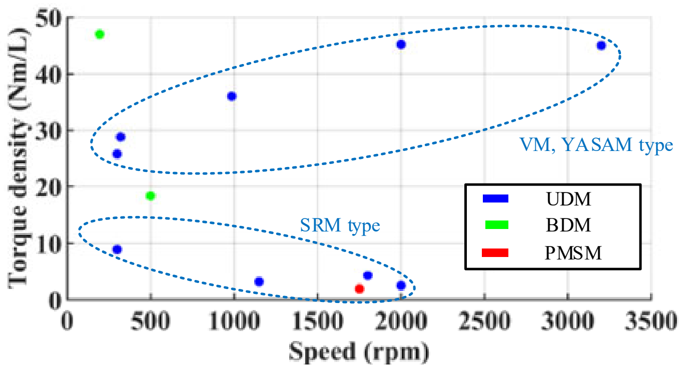

Fig. 2-17. Distribution of the PPF-DMP machines in torque density and speed.

Fig. 2-17 presents a summary of torque densities per volume and rotary speeds for various types of PPF-DMP machines under rated conditions in [40, 43, 44, 46-52, 56, 61]. The torque value is obtained by combining the torques of both mechanical ports. Based on the figure, the SRM type PPF-DMP-UDM exhibits torque density similar to that of conventional PMSM, whereas VM and YASAM type PPF-DMP-UDMs demonstrate relatively high torque density. The PPF-DMP-UDM, with its wide rated speed range, finds applications in direct drive systems such as electric trucks and electric ship propulsion. On the other hand, the PPF-DMP-BDMs offer low speed and high torque density characteristics, making them suitable for ship propulsion. Researchers have shown increased interest in PPF-DMP-UD configurations, with YASAMs already being commercially produced and VMs considered as potential solutions.

2.4 Hybrid Power Type DMP Machines

Fig. 2-18 illustrates the model of the HPF-DMP machine. This type of DMP machine is mostly used in complex power distribution applications, e.g., E-CVT for hybrid EVs (HEVs) to replace the conventional planetary gearbox. For the HPF-DMP machine, an input rotor is connected to the mechanical source (that is, the prime mover like the internal combustion engine) as an input port, which is the MP_1 in Fig. 2-18. Based on the operation status, the I/O rotor (which is MP_2 in Fig. 2-18) and the stator windings (EPs) can work both in motor mode (e.g., speed increase occasion for HEVs) and in generator mode (e.g., regenerative braking for HEVs). An E-CVT need to have the following characteristics:

1) ICE should operate in its high-efficiency speed region;
2) The speed of the I/O rotor can be controlled independently of the speed of ICE;
3) The torque of the I/O rotor can be controlled independently.

Thus, HPF-DMP machines have two sets of windings to control the speed and torque of the I/O rotor independently.

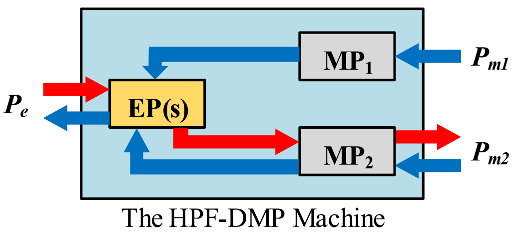

Fig. 2-18. The model of the HPF-DMP machine.

Table 2-3. Comparison of the HPF-DMP machines

Item	HPF-DMP-BM (4QT)	HPF-DMP-BLM
Topology	• One PM-excited outer I/O rotor • One DC-excited inner input rotor with winding	• One PM-excited outer I/O rotor • One inner input rotor, with or without PMs • Two electrical ports placed in the

	• Two electrical ports placed separately • Brush mechanism	stator • Brushless design
Merits	• Flexible flux controllability • Flexible speed and torque regulation • High efficiency	• Compact structure • Flexible speed and torque regulation • High torque density and power density
Weakness	• Regular maintenance needed • Serious cooling problem for the winding on the inner rotor • Complex manufacturing process	• Complex manufacturing process • Special consideration of the interaction between two electrical ports

The HPF-DMP machine is chronologically developed from brushed to brushless type, which will be introduced in the following two subsections. The features of the HPF-DMP machine are briefly shown in Table III.

2.4.1 Brushed Type HPF-DMP Machine

In [4], Eriksson and Sadarangani proposed the four-quadrant (4QT) HEV Drive System. The 4QT system consists of a stator, an outer rotor and an inner rotor. The outer rotor works as the I/O rotor, which is connected to the mechanical load, is in a double-layer or single-layer PM structure. The inner rotor acts as the input rotor, which is connected to the mechanical source and usually consists of windings and slip rings to operate as a normal synchronous machine.

The 4QT system can be considered as the combination of two PMSM parts: the outer rotor and the inner rotor form the first PMSM part, which is also called the double-rotor synchronous machine (DRM) part; the stator and the outer rotor form the second PMSM part, which is also called the single-rotor synchronous machine (SM) part. The inner rotor winding is used to control the speed of the I/O rotor. As the inner rotor is connected to the ICE, the speed of the I/O rotor can be the sum of the speed of the ICE and the magnetic field excited by the inner rotor winding. When the speed is set, the torque generated by the inner rotor winding is also set and cannot be adjusted. Therefore, the stator winding is introduced to achieve better overall torque control. The relationship can be summarized as follows:

$$\begin{cases} \Omega_{I/O} = \Omega_{ICE} + \omega_{irw} \\ T_{\mathrm{I/O}} = T_{irw} + T_{sw} \end{cases} \tag{2-8}$$

where $\Omega_{I/O}$, Ω_{ICE} and ω_{irw} are the rotation speed of the I/O rotor, the ICE and the magnetic field excited by the inner rotor winding, $T_{I/O}$, T_{irw} and T_{sw} are the torque of the I/O rotor, torque generated by the inner rotor winding and the stator winding.

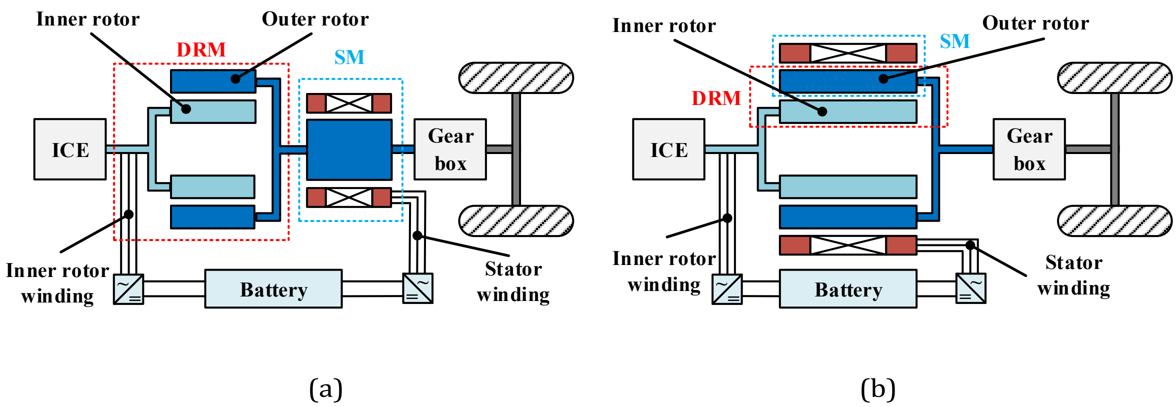

Fig. 2-19. The 4QT system [4]. (a) Separate form. (b) Concentrically combined form.

DRM and SM can be connected separately or concentrically, as shown in Fig. 2-19. Two EPs (stator windings and wound rotor windings) are controlled independently, allowing the ICE to operate efficiently in its optimal region in all four quadrants while still having the ability to adjust output power, thus saving fuel on the order of 40-50% for urbran light cars and 20-30% for heavy vehicles. In [62], a similar structure is proposed for the city bus, but the PM rotor is replaced by the induction rotor with the squirrel cage, whose results show that the fuel efficiency has increased by more than 25% compared to the normal ICE system. In [63], a flux-switching topology is proposed and the multiobjective optimization method is investigated.

In theoretical research, the general theory of DMP machines is proposed in [5]. Using a topology similar to the 4QT machine, the author further illustrates this theory in [64] and its control strategies are presented in [65], which is shown in Fig. 2-20. In [66], the author proposed a four-axis vector control method, which achieved control of both rotors by a single three-leg inverter, whose phasor diagram and control diagram are shown in Fig. 2-21. In [67], the author focused on the magnetic coupling issue of DRM and SM and gave a guideline for the I/O rotor design. A 30kW radial flux 4QT prototype was analyzed, built and tested, which showed that the cooling of the inner rotor is a serious problem due to the high frequency of the winding and the slot configuration [68]. Various analyzes have been performed to solve this problem, such as forced air cooling by introducing an external fan [69], specially designed air holes [70], or water flow cooling [71]. Mechanical design and other multiphysics studies have been conducted in [72, 73], respectively.

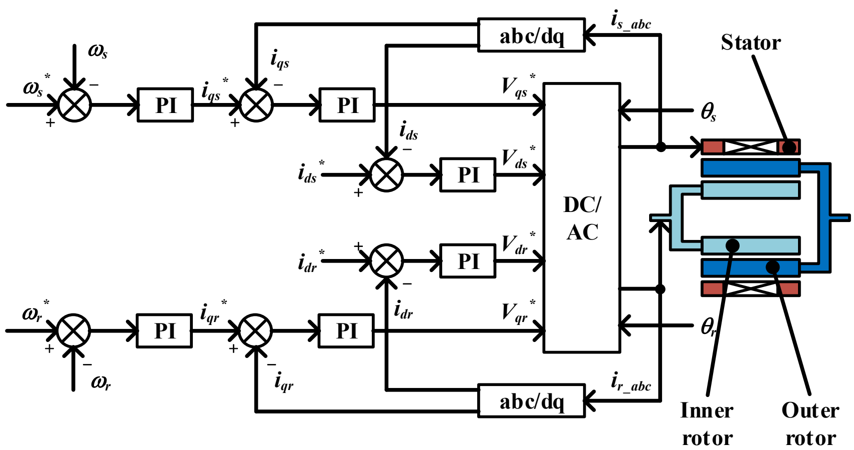

Fig. 2-20. The control diagram of the 4QT machine [65].

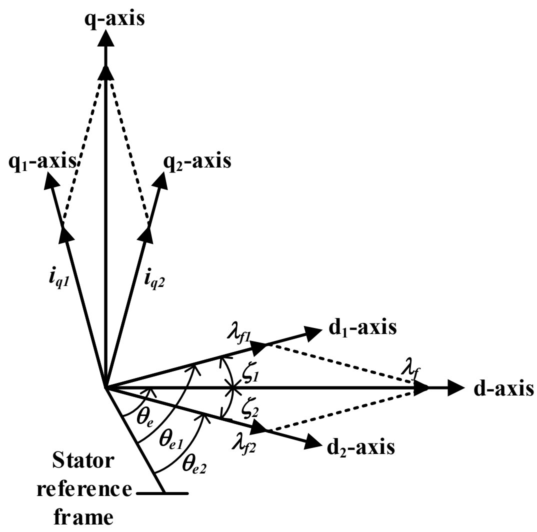

(a)

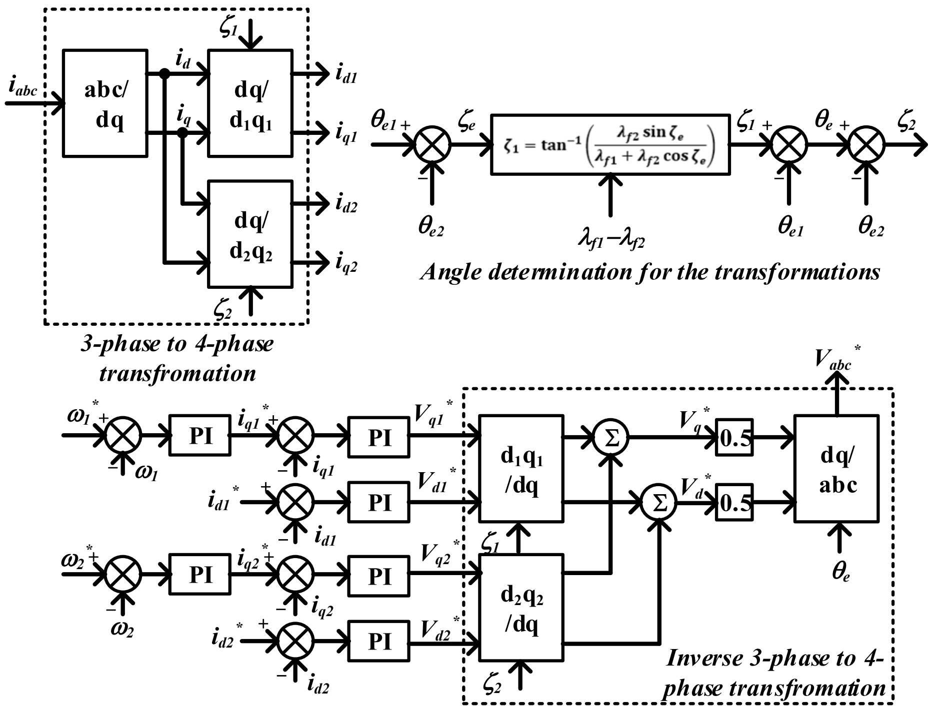

(b)

Fig. 2-21. Phasor diagram and control diagram of four-axis vector control [66]. (a) Phasor diagram. (b) Control diagram.

The characteristics of the brushed type HPF-DMP machine are summarized as below:

1)The brushed type HPF-DMP HEV drive system (4QT system) consists of a stator, an outer rotor, and an inner rotor, with the inner rotor connected to the mechanical source and the outer rotor connected to the mechanical load.

2)The DRM and SM can be connected separately or concentrically, allowing the ICE to operate efficiently in its optimal region in all four quadrants while still having the ability to adjust output power, thus saving fuel.

3)As there is winding on the inner rotor, brushes and slip rings are needed, which requires constant maintenance.

4)The cooling of the 4QT is a serious problem due to the winding on the inner rotor. Various cooling methods have been investigated.

2.4.2 Brushless Type HPF-DMP Machine

2.4.2.1 Separated HPF-DMP-BL machine

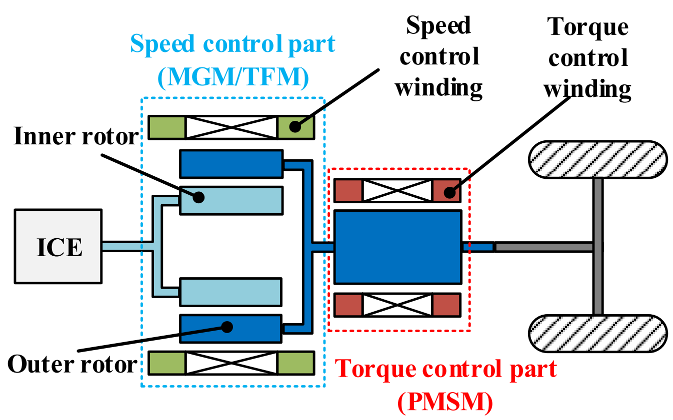

Fig. 2-22. The structure of the separated HPF-DMP-BL machine.

The structure of the separated HPF-DMP-BL machine is shown in Fig. 2-22. The inner rotor is the input rotor and the outer rotor is the I/O rotor. The speed control part and the torque control part are separate, both controlling the outer rotor. The torque control part is usually a PMSM and based on different operating principles, the speed control part can be a magnetic geared machine or a transverse flux machine (TFM).

For the topologies whose speed control part is an MGM, from (2-2), the relationship of pole pair number can be summarized as

$$\begin{cases} p_{scw} = p_{ro-scp} - p_{ri} \\ p_{tcw} = p_{ro-tcp} \end{cases} \tag{2-9}$$

where p_{scw}, p_{tcw}, p_{ro-scp}, p_{ro-tcp}, p_{ri} are the pole pair number of the speed control winding, the torque control winding, the outer rotor of the speed control part, the outer rotor of the torque control part and the inner rotor, respectively. The relationship of speed and torque can be summarized as

$$\begin{cases} p_{ri}\Omega_{ri} + p_{ro-scp}|\Omega_{ro}| = p_{scw}\omega_{scw} \\ p_{ro-tcp}\Omega_{ro} = p_{tcw}\omega_{tcw} \\ T_{ri}\Omega_{ri} + T_{ro-scp}|\Omega_{ro}| = T_{scw}\omega_{scw} \\ T_{ro-tcp}\Omega_{ro} = T_{tcw}\omega_{tcw} \\ T_{ro} = T_{ro-scp} + T_{ro-tcp} \end{cases} \tag{2-10}$$

where ω_{scw}, ω_{tcw}, Ω_{ro}, Ω_{ri} are the rotation speed of the speed control winding field, the torque control winding field, the outer rotor and the inner rotor, T_{scw}, T_{tcw}, T_{ro-scp}, T_{ro-tcp}, T_{ri} are the torque of the speed control winding, the torque control winding, the outer rotor of the speed control part, the outer rotor of the torque control part and the inner rotor, respectively.

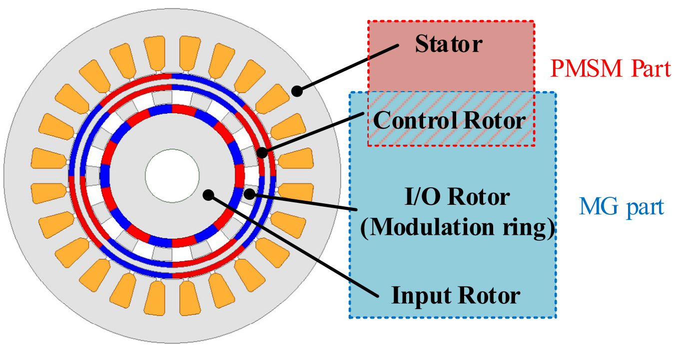

Fig. 2-23. Three-airgap topology [74].

In [74], a three-airgap topology is developed, shown in Fig. 2-23. The input rotor in this topology is the inner PM rotor and the I/O rotor is the modulation ring. Stator winding is used to control the speed. To control the torque, the I/O rotor is connected to another separate PMSM, similar to the structure shown in Fig. 2-19(a). Its operation principle and potential application are explained in [75]. The experiment shows that this topology can achieve high efficiency. However, this topology still involves three rotating parts, making it difficult to produce in mass.

In [76], the author proposed a structure whose outer rotor is the modulation ring and the inner rotor is of the surface mounted PM (SPM) type, shown in Fig. 2-24. In [77], a topology with the inner rotor of the interior PM (IPM) structure is proposed for mechanical robustness, which is shown in Fig. 2-25. In [78], a structure with sinusoidal permeance in the outer rotor is proposed to reduce PM loss, but it has the drawback of poor torque due to tangential flux leakage. In [79], a double-sided separated-type axial flux model is proposed for E-CVT and its characteristics are analyzed. Analytical modeling of the separated HPF-DMP-BL machine is performed in [80] and the results have been compared with the FEM results, showing good agreement.

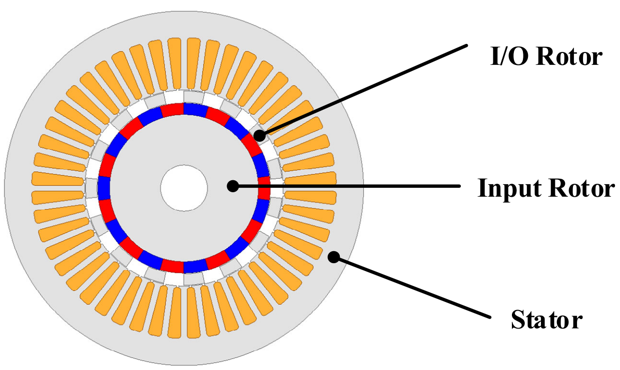

Fig. 2-24. Topology of the speed control part with SPM inner rotor [76].

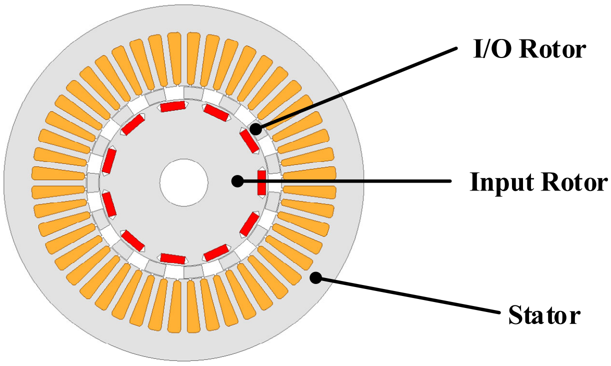

Fig. 2-25. Topology of the speed control part with IPM inner rotor [77].

In addition to the MGM type speed control part, the TFM type also exists. Traditionally, the stator of the TFM consists of two parts, the teeth and yoke, which are linked together. The general idea of the TFM speed control part is to let the teeth in the conventional TFM separate from the stator yoke and become the second I/O rotor. The relationship of the pole pair number can be described as

$$\begin{cases} p_{scw} = p_{ro-scp} = p_{ri} \\ p_{tcw} = p_{ro-tcp} \end{cases} \tag{2-11}$$

The relationship of torque and speed is the same as in (2-10).

In [81], an HPF-DMP-BL machine is proposed with the TFM type speed control part, whose I/O rotor is in claw shape, shown in Fig. 2-26(b), it can be observed that two adjacent claw-pole teeth have 180 electrical degree variation, making the flux varies when rotating. Three single phases are placed axially with a phase shift of 120 degrees and form the entire model, as shown in Fig. 2-26(c). A similar topology is proposed in [82], whose I/O rotor is of normal segmented shape. The flux path is shown in Fig. 2-27.

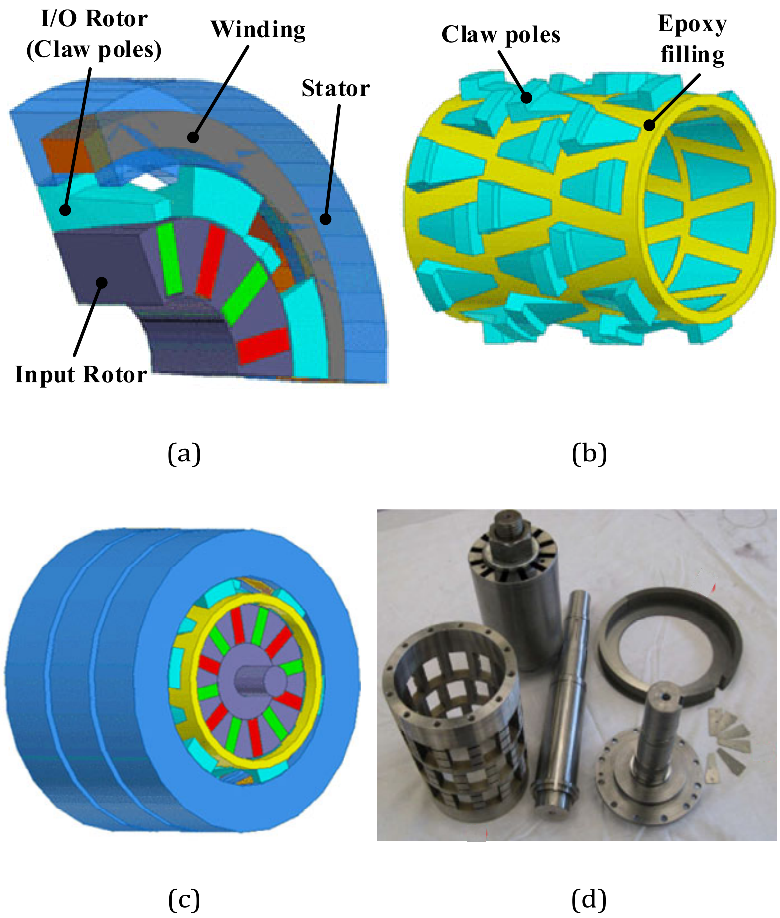

Fig. 2-26. TFM-speed-control claw-pole rotor type HPF-DMP-BL machine [81]. (a) Single phase. (b) Claw-pole rotor. (c) Whole motor after assembly. (d) Prototype.

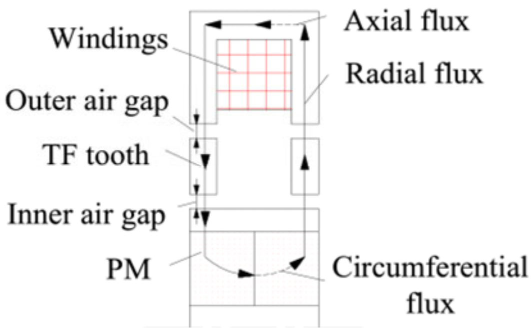

Fig. 2-27. The flux path of TFM-speed-control claw-pole rotor type HPF-DMP-BL machine [82].

2.4.2.2 Concentrical HPF-DMP-BL machine

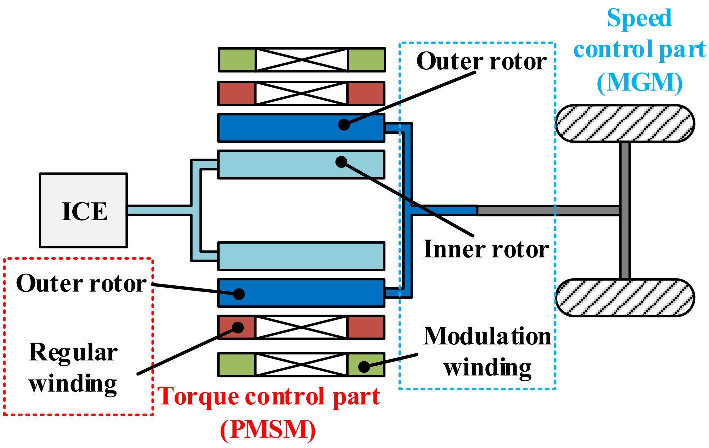

Fig. 2-28. The structure of the concentrical HPF-DMP-BL machine.

The structure of the concentrical HPF-DMP-BL machine is shown in Fig. 2-28, where the speed control part and the torque control part are concentrically integrated, making the whole machine more compact. As two sets of windings are placed in the same winding, the relationship of the pole pair number should be given as

$$\begin{cases} p_{mw} = p_{ro} - p_{ri} \\ p_{rw} = p_{ro} \end{cases} \tag{2-12}$$

where p_{mw}, p_{rw}, p_{ro} and p_{ri} are the pole pair number of modulation winding, regular winding, outer rotor and inner rotor. The relationship of speed and torque can be given as

$$\begin{cases} p_{ro}\Omega_{ro} - p_{ri}\Omega_{ri} = p_{mw}\omega_{mw} \\ p_{ro}\Omega_{ro} = p_{rw}\omega_{rw} \\ T_{ro-mw}\Omega_{ro} - T_{ri}\Omega_{ri} = T_{mw}\omega_{mw} \\ T_{ro-rw}\Omega_{ro} = T_{rw}\omega_{rw} \\ T_{ro} = T_{ro-mw} + T_{ro-rw} \end{cases} \tag{2-13}$$

where ω_{mw}, ω_{rw}, Ω_{ro} and Ω_{ri} are the rotation speed of the modulation winding field, the regular winding field, the outer rotor and the inner rotor, T_{mw}, T_{rw}, T_{ro-mw}, T_{ro-rw} and T_{ri} are the torque generated by the modulation winding, the regular winding, the modulation winding part of the outer rotor and the regular winding part of the inner rotor.

In [83, 84], an HPF-DMP-BL topology with four airgaps is proposed, shown in Fig. 2-29. This topology can be considered as the combination of two PMSM parts and a magnetic gear part. The modulating ring is the input rotor and the outer PM rotor is the I/O rotor. The winding of the inner stator controls the speed and the winding of the outer stator controls the torque. This topology has two problems: first, there are too many air gaps, which makes it difficult to maintain a uniform air gap length in manufacturing. Second, both PM rotors are double-layer structures. PMs on both sides of the rotor need to be magnetically decoupled for better performance and the yoke needs to be specially designed.

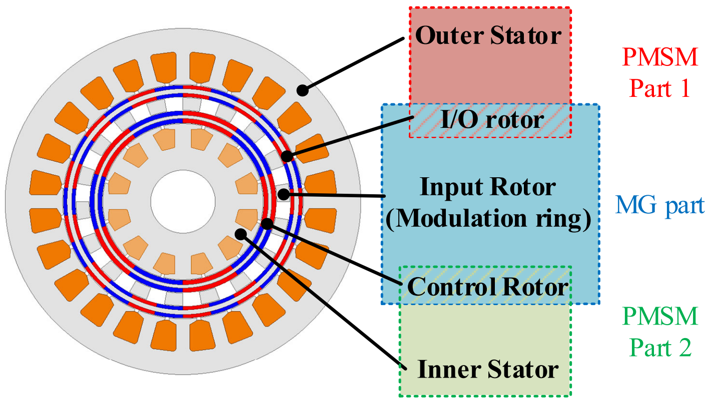

(a)

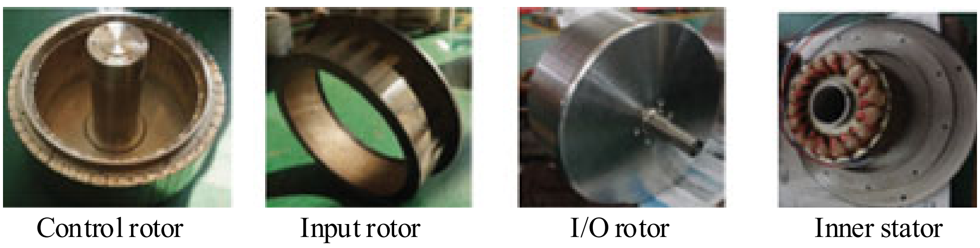

(b)

Fig. 2-29. Four-airgap topology [83, 84]. (a) Machine configuration. (b) Prototype.

In [85], a double-stator double-rotor structure is presented, shown in Fig. 2-30. This topology can be considered as the combination of a vernier machine (VM) and an MGM. In [86, 87], the authors further simplified the topology to a single-stator double-rotor dual-airgap structure, shown in Fig. 2-31, which is achieved by using two sets of windings (that is, EP). The modulated winding, the outer stator and the inner stator form the MGM part and the regular winding and the outer rotor form the PMSM part. Both PM rotors adopt the consequent pole structure. Two sets of windings are placed on the same stator in a way that makes the structure more compact. An axial flux model is presented in [88], where the power flows of different operating modes and general working concepts are illustrated.

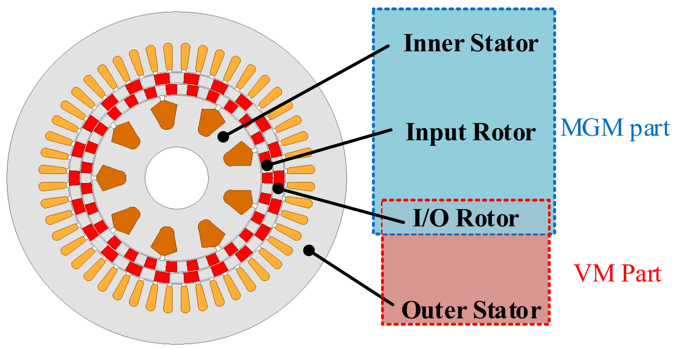

Fig. 2-30. Double-stator double-rotor topology [85].

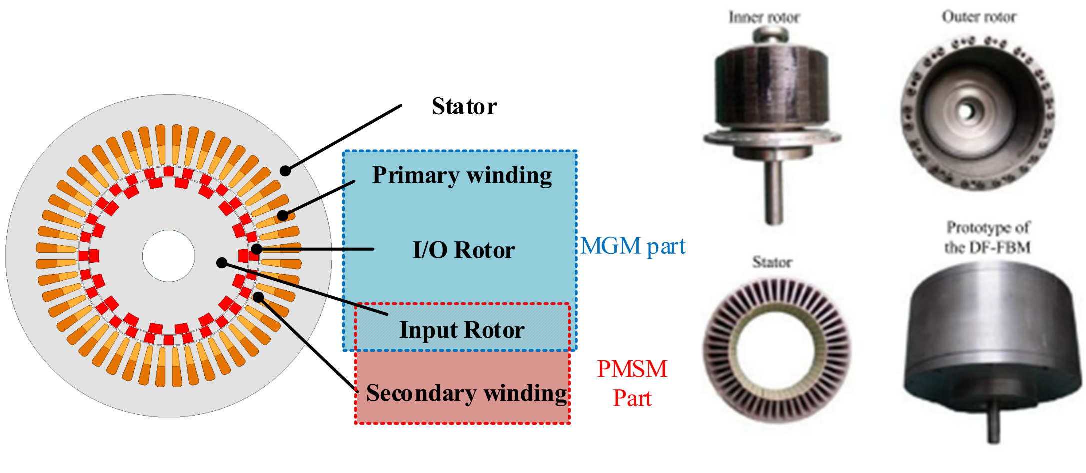

(a) (b)

Fig. 2-31. Single-stator double-rotor topology [86, 87]. (a) Machine configuration. (b) Prototype.

The HPF-DMP-BL machine generally has the problem of asymmetric phase back-EMF and high cogging torque due to asymmetric magnetic circuits for three-phase windings. To solve this problem, in [89], a complementary structure is proposed in which both rotors shifted a certain angle with each other, as shown in Fig. 2-32. The general design technique and its FOC control are introduced in [89]. The functionality and performance of the complementary structure were evaluated in [90].

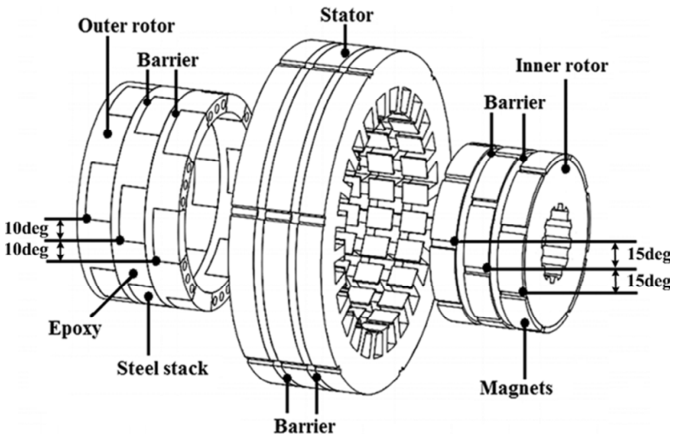

(a)

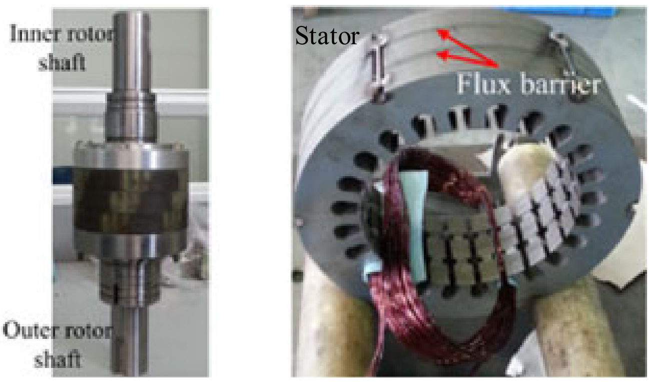

(b)

Fig. 2-32. The complementary type BL-HPF-DMP machine [89]. (a) Machine configuration. (b) Prototype.

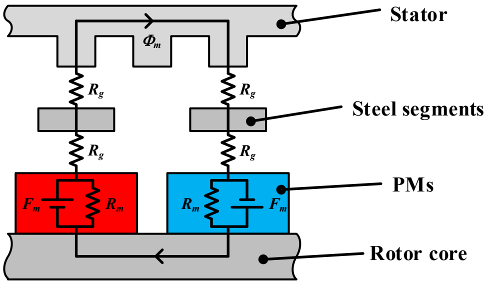

(a)

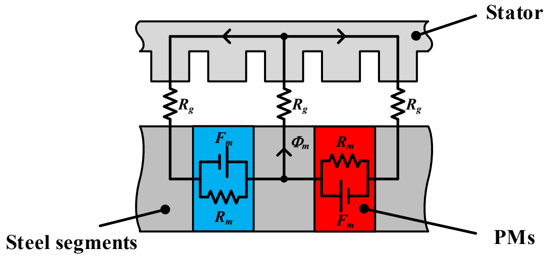

(b)

Fig. 2-33. The magnetic circuit of the PMSM part [91]. (a) Consequent-pole structure. (b) Spoke-array structure.

As the flux of the outer PM rotor in the consequent-pole structure needs to pass two airgaps to form a close loop, the torque of the PMSM part is relatively weak, as shown in Fig. 2-33(a). To enhance the torque of the PMSM part, a topology with spoke-PMs in the outer rotor is proposed in [91, 92]. With this configuration, the torque component is enhanced because the flux only needs to pass one airgap, which is shown in Fig. 2-33(b). The flux-focusing effect is another merit. This structure adopts the stator of the auxiliary teeth, where two sets of windings are placed on the main teeth and the auxiliary teeth, as shown in Fig. 2-34(a).

In [93, 94], a topology with the inner rotor of the salient pole is proposed, shown in Fig. 2-34(b), with the aim of reducing eddy current losses in PMs by modulating components of harmonic flux less unworking in the airgap. The mechanical structure of the inner rotor is also much simpler. The design process of the spoke-PM-type model is introduced in [95], where the sizing equations have been deduced to reduce the design time.

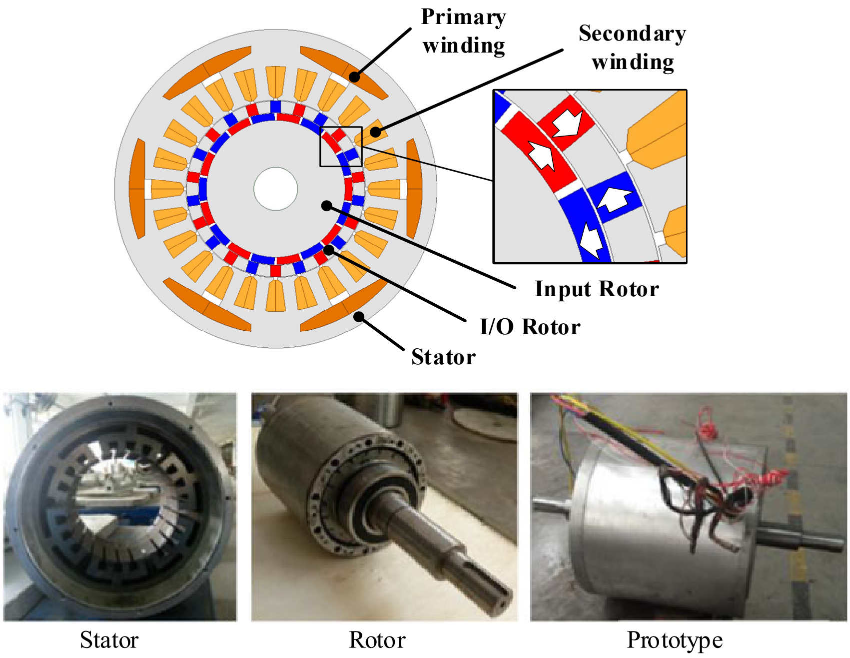

(a)

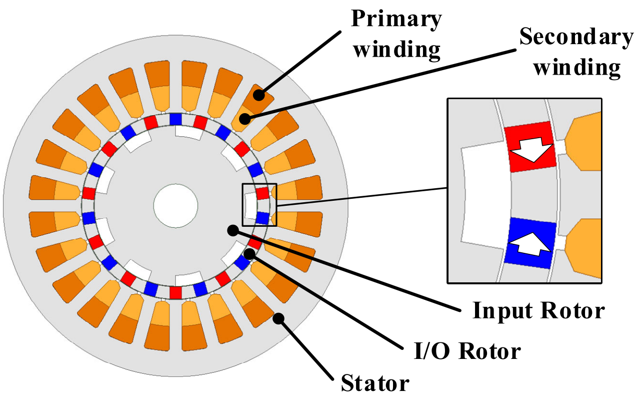

(b)

Fig. 2-34. The spoke-array type BL-HPF-DMP machine. (a) Split-teeth type [91, 92]. (b) Salient-pole-inner-rotor type [93, 94].

To boost the torque density of the HPF-DMP-BLM, several variants are proposed. A variant with open slot configuration is proposed in [96], which can be considered as the combination of a VM and MGM. With the vernier structure, this type of machine has higher torque generation ability, but its torque ripple is higher than conventional HPF-DMP-BL machine. In [97], a variant using high-order harmonic modulation is proposed to improve the torque density of the HPF-DMP-

BL machine. Its compound outer rotor is artificially designed to enhance the third harmonic component of airgap flux density in the inner airgap while remaining the fundamental component unchanged in the outer airgap.

In [98], an integrated winding is proposed that replaces the original two sets of windings with a single winding configuration driven by two inverters. Compared to the conventional two-set independent winding configuration, the integrated winding configuration has the merit of lower copper loss and a simple manufacturing process. The methods of how to configure the winding using different phase belt is presented in [99]. The mathematical model and the drive method considering the coupling effect and the winding asymmetry of the integrated winding structure are developed in [100].

For the analysis of characteristics and analytical modelling of the HPF-DMP-BL machine, the working principles of the double rotor model are discussed in [101, 102]. The analytical modelling of the double-rotor multi-winding machine is presented in [9] and the analytical method of determining the d-q axis was illustrated in [102]. The problem of magnetic coupling between two sets of windings is discussed in [103] and a guideline for choosing the pole pair combination is introduced in [104]. In [105], the characteristics of HPF-DMP-BL machine speed, torque and power flow are analyzed using diagrammatic methods. Investigation of the HPF-DMP-BL machine power factor (PF) is carried out in [106], where the control strategy to improve the PF is presented.

The coupling of two electrical ports for the HPF-DMP machines are very essential, as it may cause unintended harmonics generated which may affect the performance. In [92, 107], the authors give the decoupling principle according to the periodicity of the slot number and two rotors, giving a method of verifying whether two windings are decoupled according to the greatest common divisors of slot number and rotor pole pair. In [108], the authors categorizes the topologies of existing HPF-DMP machines into five types and presents a systematic decoupling analysis with a developed simple indicator to fast identify the coupling type.

For the control strategies, the conventional field oriented control is discussed in [109], shown in Fig. 2-35. A sensorless control based on the dual slide model observer (SMO) estimator was discovered in [110], which is shown in Fig. 2-36.

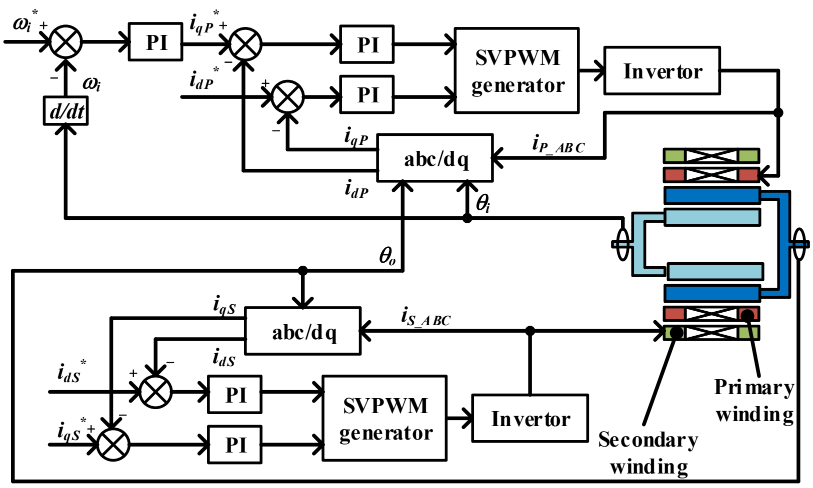

Fig. 2-35. Diagram of conventional FOC control for HPF-DMP-BL machine [108].

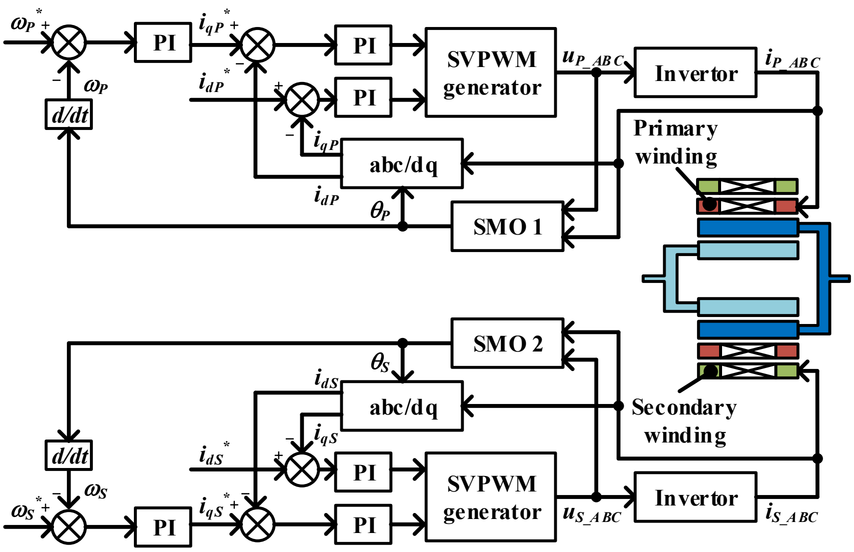

Fig. 2-36. Diagram of dual-SMO estimator-based sensorless control for HPF-DMP-BL machine [109].

Due to the complexity of the double-rotor structure, optimizing the parameters using conventional analytical methods is time-consuming. Various optimization methods, such as the leveling genetic algorithm (GA) in [8] and [111], the adaptive differential evolution algorithm (ADE) in [112], are used for this topology.

The energy flow relationship of different ports under different working modes is the most important issue for HPF-DMP machine. A general showing schematic of the power flow diagram of the HPF-DMP-BL machine can be simplified and shown with block diagram form in Fig. 2-37. The power flow under different working modes can be generally concluded in Fig. 2-38 [9, 113]. For the application of aviation propulsion, the working modes in Fig. 2-38(a), (b), (d) and (e) are usually adopted. All eight modes are used for the applications of electric vehicles.

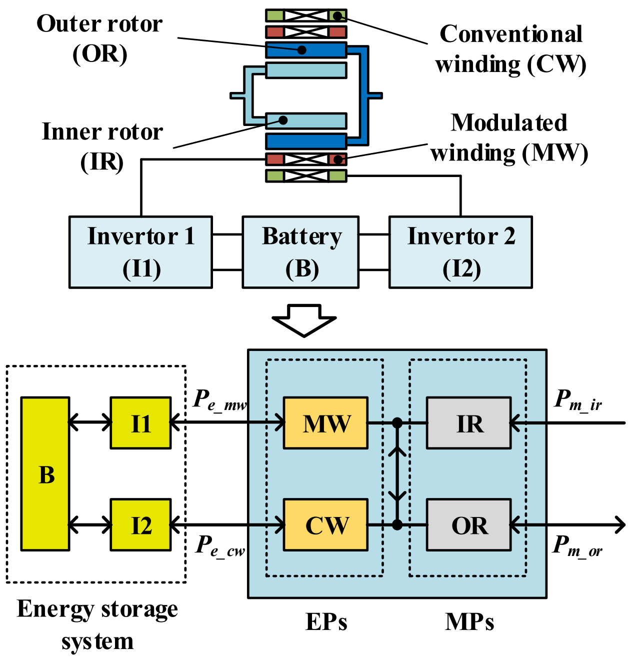

Fig. 2-37. Showing schematic of the relationships between the HPF-DMP-BL machine and the power flow diagram.

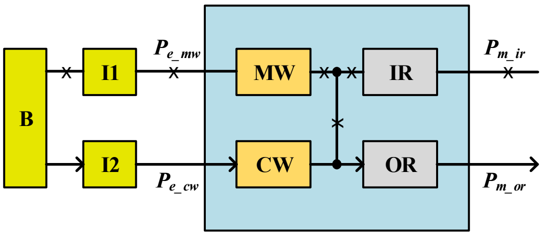

(a)

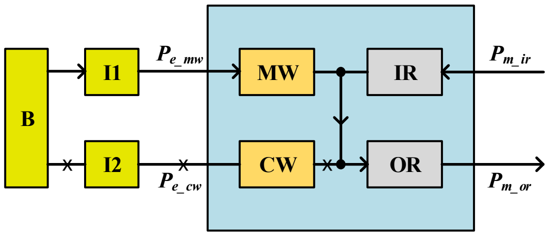

(b)

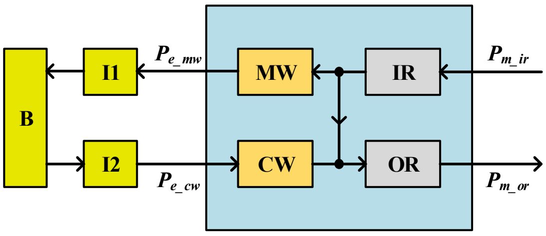

(c)

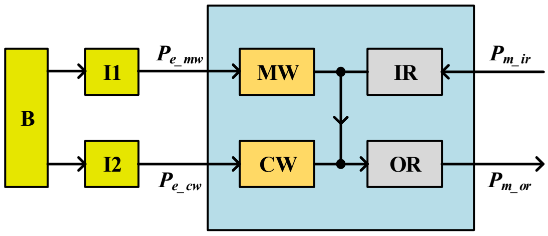

(d)

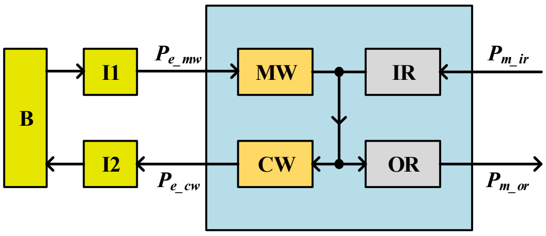

(e)

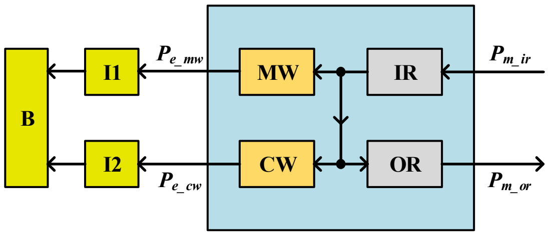

(f)

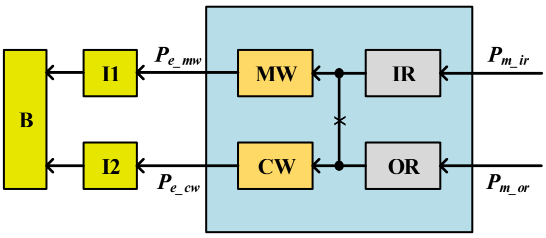

(g)

Fig. 2-38. Power flow diagrams of different working modes for the HPF-DMP-BL machine [9, 113]. (a) Pure electrical drive. (b) Pure engine drive. (c) Reduced speed and increased torque. (d) Increased speed and increased torque (Hybrid mode). (e) Increased speed and reduced torque (Battery charging mode). (f) Reduced speed and reduced torque. (g) Regenerative braking.

The characteristics of the brushless type HPF-DMP machine are summarized as below:

1)The speed control part and torque control part of the brushless type HPF-DMP machine are separate, both controlling the outer rotor.

2)The speed control part consists of both rotors and the modulation winding, which can be regarded as an MGM or a TFM. The torque control part consists of the regular winding and the outer rotor, which can be regarded as a PMSM.

3)The complementary structure is proposed to solve the problem of asymmetric phase back-EMF and high cogging torque due to asymmetric magnetic circuits for three-phase windings.

4)The spoke-PM-type model is proposed to enhance the torque of the PMSM part of the machine with a shorter magnetic circuit.

5)An integrated winding configuration is proposed to replace the conventional two-set independent winding configuration in the HPF-DMP-BL machine, offering lower copper loss and a simpler manufacturing process.

6)Various optimization methods, such as the leveling GA and ADE are used for this topology. Control strategies such as the FOC and sensorless control based on the dual SMO estimator have been discussed for the HPF-DMP-BL machine.

2.5 Challenges and Future Trends

The DMP machines possess promising development prospects in transportation electrification. However, many challenges remain in moving from theory to application. The main challenges and future trends of DMP machines can be summarized as follows:

2.5.1 Structural Simplification

The complexity of the manufacturing process is a significant challenge for the widespread adoption of DMP machines. Simplifying the construction of DMP machines is crucial to overcome this limitation. One potential approach to address this issue is the adoption of modular design, which offers the possibility of easier construction and assembly. Embracing modular design could become a prominent trend in future DMP machine designs.

2.5.2 Winding Coupling

The DMP machines generally exhibit high pole pairs and abundant magnetic field harmonics, leading to increased frequency and greater iron and copper loss. Additionally, their control becomes more challenging. To address these issues, it is necessary to explore suitable DMP structures by leveraging advancements in technologies such as PM materials of high and low coercivity, aiming to reduce the loss at high speeds and enhance the practicality.

2.5.3 Temperature Field Analysis

Most existing literatures focused on the electromagnetic field and ignored the issue of temperature rise. For application, the analysis in temperature is essential, especially for the DMP machines which have multiple airgaps and have numerous PMs. Therefore, adopting joint simulation of multi-physical fields can establish a rapid and effective method for analyzing and predicting temperature rises in each component, guiding further improvements in the cooling system.

2.5.4 Torque Density

For the hybrid DMP machine, as a new type of multifunctional integrated system, it exhibits weaker torque and power output capacities compared to the combination of multiple independent machines and gearsets. Notably, the torque density of brushless hybrid DMP topologies remain lower than that of brushed topologies. Therefore, the design of novel structured brushless hybrid DMP topologies is required to further enhance torque density and power density.

2.5.5 Power Factor

Because most kind of DMP machines is based on the principle of flux modulation, they all have the issue of lower power factors compared to the conventional non-flux modulated machines. In practical applications, lower power factor leads to larger power capacity control devices, which results in increased system size and weight, thereby reducing practicality. Therefore, the design of novel structured DMP topologies is required to further enhance power factor.

2.5.6 Dynamic Performance and Fault Tolerance in the Control System

Hybrid DMP machines can generally be regarded as the combination of two machines, which consist of two rotors, two sets of windings, and two air gaps, leading to significant electromagnetic coupling and complex changes in motor parameters. As the integration of the DMP machine progresses, internal electromagnetic coupling becomes more serious. Consequently, improvements in the driving circuit and control algorithms are necessary to decouple two machine parts, viz. two EPs, thereby enhancing system dynamic response. Moreover, in applications like hybrid power systems, higher reliability is required. Therefore, research on control strategies, such as position sensor fault tolerance methods, sensorless control, and current control methods under open winding conditions, are essential to provide the system with robust fault tolerance capabilities.

2.6 Summary

This paper provides an extensive literature review of multiport machines from the perspective of DMP machines, discussing their working principles and different topologies. The three types of multiport machines based on power flow relationships, namely SPF-DMP machines, PPF-DMP machines, and HPF-DMP machines, are examined in terms of their advantages and challenges.

- SPF-DMP machines utilize an excited idle rotor connected through electromagnetic coupling, enhancing performance with variations in functionality across machine types. SPF-DMP-IM improves efficiency and power factor, while SPF-DMP-MGM amplifies torque, functioning as single-mechanical port machines. Pseudo-direct-drive machines demonstrate high torque density and power factor potential.
- PPF-DMP machines employ parallel-connected I/O rotors, with unidirectional machines having rotors on the same shaft for identical rotation speeds. PPF-DMP-UDM function as high torque density single MP machines, while PPF-DMP-BDM face challenges in mass production despite their straightforward working principle.
- HPF-DMP machines comprise an input MP and an I/O MP, commonly used in E-CVT applications. The HPF-DMP brushed machine (4QT system) explores the topology but encounters issues with brushed structure and cooling for the inner wound rotor. The HPF-DMP-BL structure employs modulation and dual EPs for independent control of torque and speed, representing the prevailing research trend.

- DMP machines offer compactness, high efficiency, and torque density, suitable for E-CVT and contra-rotating propulsion. However, the dual airgap structure complicates manufacturing compared to single MP machines, limiting current applications. Scholars propose simplified or enhanced structures to overcome this challenge, while technological advancements in mechanical and material technologies will facilitate broader utilization of DMP machines.

The literature review reveals several research gaps in the field:

- The torque performance of multiport machines remains unsatisfactory, especially for the magnetic geared part. The designs presented in Chapter 3 and Chapter 4 address this specific research gap.
- In comparison to conventional machines, the flux controllability of existing multiport machine designs is diminished due to the presence of two airgaps in magnetic-geared machines. The designs presented in Chapter 5 and Chapter 6 specifically target this research gap.

Chapter 3 A High-Order-Harmonic Compound Rotor Based Brushless Dual-Electrical-Port Dual-Mechanical-Port Machine

3.1 Introduction

With growing concerns about environmental pollution and the energy crisis, the substitution of transportation that consumes fossil fuel with hybrid energy have become a popular trend. Nowadays, hybrid electrical transportation technology has received more attention and gained rapid development, including hybrid electric vehicles [87], hybrid electric ships [26], and hybrid electric aircraft [9]. Among all hybrid electrical devices, the power-split-type hybrid electrical devices have attracted the most attention due to their increased fuel economy, high control flexibility, and high efficiency [94].

For power-split-type hybrid electrical devices, the crucial component is the continuously variable transmission (CVT) system. The CVT system can realize the power combination and distribution from the mechanical input, the electrical port, and the battery system. It can also decouple input speed, output speed, and torque. However, the commercial CVT uses mechanical planetary gear, which has the problem of low compactness, vibration, and noise [102]. In addition, the planetary gear suffers from mild wear under prolonged, high-load operating conditions, because the gear teeth are in direct physical contact with each other, hence needing regular maintenance.

To address the mechanical structure-related issues in the CVT system, the electrical CVT (E-CVT) is developed, which is designed with two mechanical ports (MPs) and two electrical ports (EPs) for decoupling the torque and the speed. Generally, the inner rotor is connected with the internal combustion engine (ICE) as input MP, and the outer rotor is connected with the load, like wheels for vehicles as input/output MP. Two EPs control the speed and torque of the input/output MP, respectively.

In [4, 68, 69], the four-quadrant (4QT) E-CVT system is proposed. The 4QT system can be considered as a combination of a dual-rotor synchronous machine (DRM) and a single-rotor synchronous machine (SM), which improved the compactness. However, as the DRM winding is wound on the inner rotor, the 4QT system has serious cooling problems [70]. Brushes and slip-rings also increase the unreliability of the whole system.

Recently, with the development of flux modulation theory, brushless E-CVTs have been developed, namely, the brushless dual-electrical-port dual-mechanical-port machine (BLDDM). The BLDDM can be classified into two categories according to the operating principle. The first type is the transverse-flux (TF) type, which can be considered as a combination of the transverse-flux machine (TFM) part and the permanent magnet synchronous machine (PMSM) part [82, 114]. Nevertheless, the TFM suffers from increased difficulty in manufacture, which limits its wide application. The second type is the magnetic-geared (MG) type, which consists of the magnetic-geared machine (MGM) part and a PMSM part. The dual-PM bidirectional flux modulation BLDDM with two consequent-pole PM rotors is first proposed and analyzed in [87, 101]. In [91] and [115], the authors replaced the radial PM on the outer rotor with the spoke PM, which shortens the flux path and increases the torque density of the PMSM part.

In [98] and [116], an integrated winding is proposed that combines two sets of windings into one, which further reduces the copper loss. Unfortunately, the MGM part in BLDDM usually suffers low torque density for the limited utilization of flux harmonics, which does not have much attention in the industry.

In [117], a novel high-order harmonic winding design is proposed for the vernier reluctance machine. It breaks the traditional winding design principle based on the modulation effect with the fundamental harmonic of excitation. Instead, the authors design a novel winding using the harmonics higher than the fundamental one, i.e., the high-order harmonic winding. This design principle can be used in BLDDM to further enhance the torque density of the MGM part while maintaining the same amount of PM material.

In this paper, a novel BLDDM structure is proposed using a high-order harmonic modulation to improve the torque density. The key is that the compound outer rotor is artificially designed to enhance the third-harmonic component of airgap flux density in the inner airgap while remaining the fundamental component unchanged in the outer airgap. Both components can be fully used by two windings in this design. The paper is organized as follows. In Sections 3.2 and 3.3, the machine structure and the operating principle are introduced. In Section 3.4, an initial model is built to verify the validity of the principles, and then the optimization of the geometrical parameters is introduced. In Section 3.5, the proposed BLDDM is compared with the conventional design in other literature in terms of the torque and working principle. In Section 3.6, a prototype is made, and the experiment results verify the feasibility and advantages of the proposed design. Finally, conclusions are drawn in Section 3.7.

3.2 Machine Structure

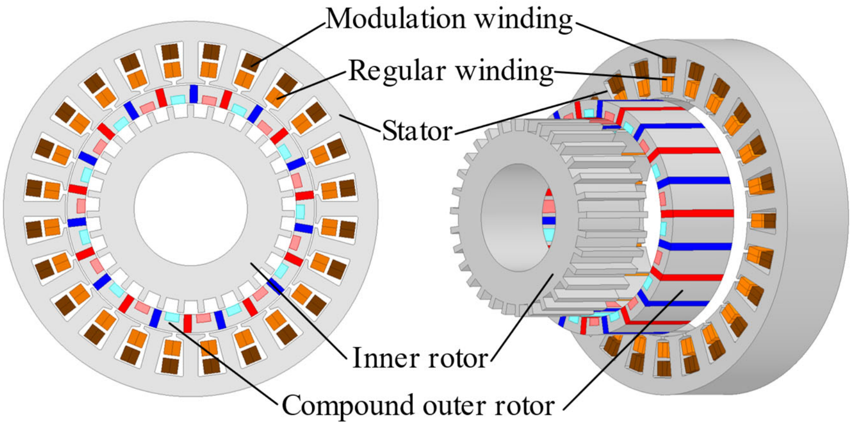

(a)

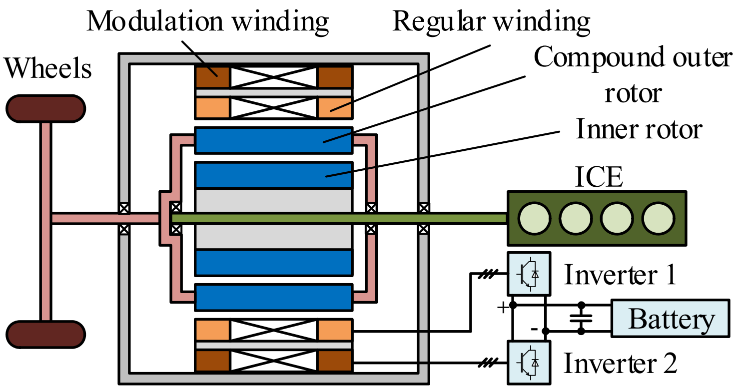

(b)

Fig. 3-1. The configuration of the proposed BLDDM based E-CVT system. (a) Proposed BLDDM structure. (b) Schematic of the E-CVT.

Fig. 3-1(a) shows the structure of BLDDM. The stator has 24 slots, where the 2-pole-pair modulation winding and the 11-pole-pair regular winding are placed inside. Each rotor is connected to a shaft individually, shown in Fig. 3-1(b). The modulation winding and two rotors constitute an MGM which accounts for the speed and torque distribution between the two rotors. The regular winding and the outer rotor form a PMSM which enhances the compound outer rotor torque during acceleration or driving uphill.

The compound outer rotor is composed of 11 pole pairs of spoke-type PMs and 11 pole pairs of radial-magnetized PMs, shown in Fig. 3-2. The iron core of the outer rotor is placed between two adjacent spoke PMs, and the radial-magnetized PM is placed in the duct along the inner side of the outer rotor. The radial-magnetized PMs are used to enhance the third harmonic component magnetomotive force (MMF) in the inner airgap while remaining the fundamental component in the outer airgap. As the MMF in the outer airgap is used for the interaction with the regular winding and the MMF in the inner airgap is used for the flux modulation with the inner rotor, both harmonic components can all be fully used in this design. The inner rotor consists of only 31 iron teeth, which shows good mechanical robustness.

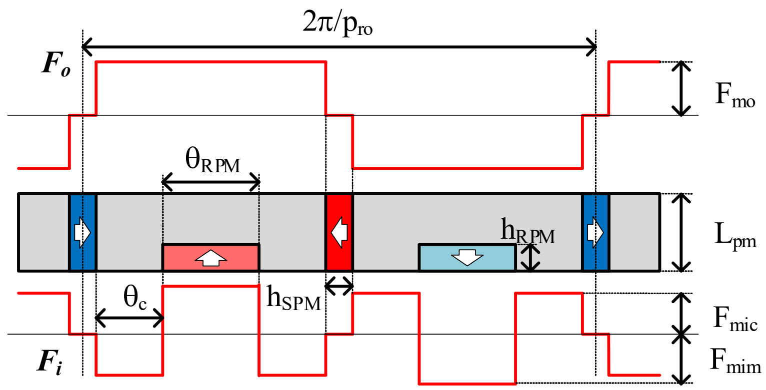

Fig. 3-2. The configuration of the compound outer rotor and the dual-pole-pair MMF in the inner and outer airgap.

3.3 Operating Principle

3.3.1 MMF Analysis

The magnetomotive force (MMF) waveforms excited by the PMs in the inner and outer airgap with the notations are shown in Fig. 3-3. To quantitively analyse the MMF waveform, when neglecting the magnetic resistance in the iron core, the magnetic equivalent circuit (MEC) can be drawn in Fig. 3-3 [118], where R_o, R_{ic}, and R_{im} are the magnetic resistance of outer airgap, inner airgap under the iron core section, and inner airgap under the PM section, R_s and R_r are the internal magnetic resistance of spoke-type PM and radially-magnetized PM, F_s and F_r are the MMF of spoke-type PM and radially-magnetized PM. For the convenience of analysis, the magnetic potential of the outer iron ring is set as zero.

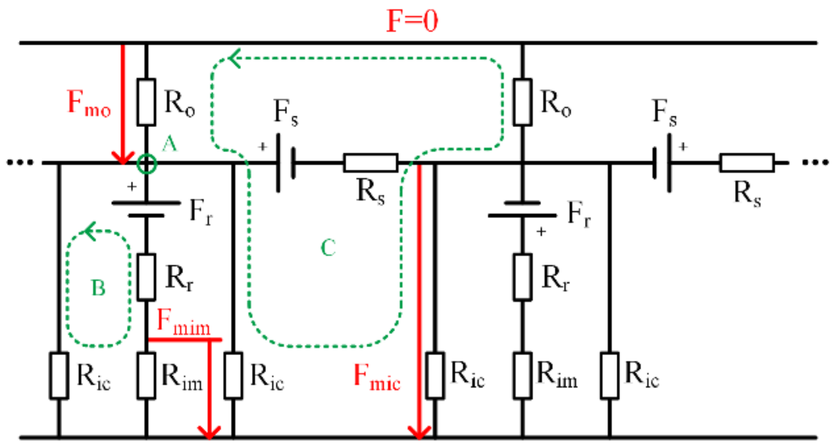

Fig. 3-3. The magnetic circuit of outer rotor.

The magnetic circuit with the node and loops for calculation is shown in the green lines in Fig. 3-3. Based on Kirchhoff's first law, the following relationship of node A can be obtained

$$\frac{F_{mo}}{R_o} + 2\frac{F_{mic}}{R_{ic}} - \frac{F_{mim}}{R_{im}} - 2\frac{F_s - 2F_{mo}}{R_s} = 0 \tag{3-1}$$

Based on Kirchhoff's second law, the following relationships of loop B and C can be given as

$$F_r - F_{mic} - F_{mim} - \frac{R_r}{R_{im}} F_{im} = 0 \tag{3-2}$$

$$2F_{mo} - 2F_{ic} = 0 \tag{3-3}$$

Therefore, (3-1)-(3-3) can be written in the matrix form $\mathbf{AF} = \mathbf{B}$, where $\mathbf{A}$ is the magnetic resistance matrix, $\mathbf{F}$ is the unknown MMF matrix, and $\mathbf{B}$ is the known MMF matrix:

$$\begin{bmatrix} \frac{1}{R_0}+\frac{4}{R_s} & \frac{2}{R_{ic}} & -\frac{1}{R_{im}} \\ 0 & 1 & 1+\frac{R_r}{R_{im}} \\ 2 & -2 & 0 \end{bmatrix} \begin{bmatrix} F_{mo} \\ F_{mic} \\ F_{mim} \end{bmatrix} = \begin{bmatrix} \frac{2F_s}{R_s} \\ F_r \\ 0 \end{bmatrix} \tag{3-4}$$

Consequently, **F** can be calculated:

$$\mathbf{F} = \begin{bmatrix} F_{mo} \\ F_{mic} \\ F_{mim} \end{bmatrix} = \mathbf{A}^{-1}\mathbf{B} = \frac{1}{R_{sum}} \cdot \begin{bmatrix} R_{ic}R_o(2F_sR_{im} + F_rR_s + 2F_sR_r) \\ R_{ic}R_o(2F_sR_{im} + F_rR_s + 2F_sR_r) \\ R_{im}(4F_rR_{ic}R_o - 2F_sR_{ic}R_o + F_rR_{ic}R_s + 2F_rR_oR_s) \end{bmatrix} \tag{3-5}$$

$$R_{sum} = \frac{R_{ic}R_{im}R_oR_s}{2}\det(\mathbf{A}) \tag{3-6}$$

From Fig. 3-2, the MMF in the inner and outer airgap can be expressed by Fourier series as

$$F_i(\theta,t) = \sum_{n=1,odd}^{+\infty} F_{in}\cos(np_{ro}(\theta+\Omega_{ro}t)+\varphi) \tag{3-7}$$

$$F_o(\theta,t) = \sum_{m=1,odd}^{+\infty} F_{om}\cos(mp_{ro}(\theta+\Omega_{ro}t)+\varphi) \tag{3-8}$$

where p_{ro} is the pole pair number (PPN) of the outer rotor, which is also the PPN for both radially-magnetized and spoke-type PMs on the outer rotor, Ω_{ro} is the rotating speed of the outer rotor, φ is the initial angle of the outer rotor. F_{in} and F_{on} are the corresponding magnitude of the n-th and m-th MMF components in inner and outer airgaps, which can be further expressed by means of Fourier decomposition as

$$F_{in} = \frac{8F_{mic}}{n\pi}\sin\left(np_{ro}\frac{\theta_c}{2}\right)\cos\left(np_{ro}\frac{\theta_{RPM}+\theta_c}{2}\right) - \frac{4F_{mim}}{n\pi}\sin\left(np_{ro}\frac{\theta_{RPM}}{2}\right) \tag{3-9}$$

$$F_{om} = \frac{4F_{mo}}{m\pi}\sin\left(mp_{ro}\frac{2\theta_c+\theta_{RPM}}{2}\right) \tag{3-10}$$

3.3.2 MGM Part Analysis

The MGM part is composed of the modulation winding, the outer rotor, and the inner rotor. The permeance waveform of the inner rotor in the inner airgap is shown in Fig. 3-4, which can be given as

$$\Lambda(\theta,t)=\frac{\Lambda_0}{2}+\sum_{k=1}^{+\infty}\Lambda_k\cos\left(kp_{ri}(\theta+\Omega_{ri}t)\right) \tag{3-11}$$

where p_{ri} is the number of the inner rotor's salient poles, Ω_{ri} is the rotating speed of the inner rotor, and Λ_k is the magnitude of the k-th permeance component, which can be expressed by Fourier decomposition as

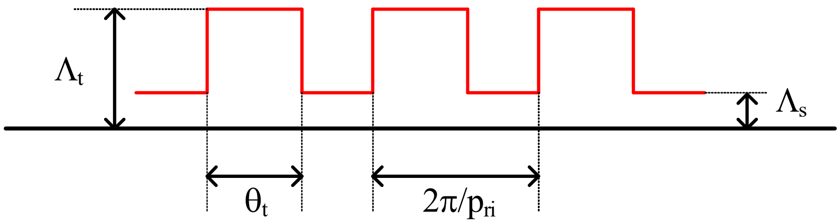

Fig. 3-4. Permeance waveform of the inner rotor.

$$\Lambda_k=\begin{cases}2\Lambda_s+\frac{\theta_t p_{ri}}{\pi}(\Lambda_t-\Lambda_s), & k=0\\ \frac{2(\Lambda_t-\Lambda_s)}{k\pi}\sin\left(\frac{kp_{ri}\theta_t}{2}\right), & k>0\end{cases} \tag{3-12}$$

The airgap flux density of the MGM part equals to the product of F_i and Λ, which can be expressed as

$$\begin{aligned}B_{MGM}(\theta,t)&=F_i(\theta,t)\Lambda(\theta,t)\\&=\sum_{n=1,odd}^{+\infty}\sum_{l=-\infty}^{+\infty}\frac{F_{in}\Lambda_l}{2}\cos((np_{ro}+lp_{ri})\\&\times\left(\theta+\frac{np_{ro}\Omega_{ro}+lp_{ri}\Omega_{ri}}{np_{ro}+lp_{ri}}t\right)+\varphi)\end{aligned} \tag{3-13}$$

where

$$l=\pm k,\Lambda_l=\Lambda_{-l} \tag{3-14}$$

According to (3-13), the PPN and the speed of each modulated harmonic can be calculated as

$$PPN_{MGM(n,l)}=|np_{ro}+lp_{ri}| \tag{3-15}$$

$$\Omega_{MGM(n,l)}=\frac{np_{ro}}{np_{ro}+lp_{ri}}\Omega_{ro}+\frac{lp_{ri}}{np_{ro}+lp_{ri}}\Omega_{ri} \tag{3-16}$$

The PPN of the modulation winding p_{wm} should match the PPN of the modulated harmonic that generates the corresponding back EMF for maximum steady torque transformation. Conventionally, p_{wm} is selected as the component that is modulated by the fundamental component (i.e., $PPN_{MGM(1,-1)} = |p_{ro} - p_{ri}|$) because the fundamental component is generally much higher than the rest of the harmonics. However, in this proposed design p_{wm} is selected as the component that is modulated by the third harmonic, because the flux density and the speed of the $PPN_{MGM(3,-1)}$-th component are both higher than that of the $PPN_{MGM(1,-1)}$ one. The PPN and the speed of the modulated winding can be expressed as

$$p_{wm} = PPN_{MGM(3,-1)} = 3p_{ro} - p_{ri} \tag{3-17}$$

$$\Omega_{wm} = \Omega_{MGM(3,-1)} = \frac{3p_{ro}\Omega_{ro} - p_{ri}\Omega_{ri}}{3p_{ro} - p_{ri}} \tag{3-18}$$

The detailed explanation and calculation are presented in Section 3.4.1.

3.3.3 PMSM Part Analysis

The PMSM part is composed of the regular winding and the outer rotor. The spoke-type PMs enable the flux to get through only the outer airgap, which has greatly decreased the magnetic reluctance [94]. The configuration of PMs on the outer rotor also has the flux-focusing effect, which increases the flux density in the airgap.

As the stator can be considered a slotless iron core, its permeance only consists of the average component Λ_{st0}. Thus, the airgap flux density of the PMSM part can be expressed as the following based on (3-8):

$$B_{PMSM}(\theta, t) = \sum_{m=1,odd}^{+\infty} F_{om}\Lambda_{st0}\cos(mp_{ro}(\theta + \Omega_{ro}t) + \varphi) \tag{3-19}$$

According to (3-19), the PPN and the speed of each component can be calculated as

$$PPN_{PMSM} = mp_{ro} \tag{3-20}$$

$$\Omega_{PMSM} = \Omega_{ro} \tag{3-21}$$

From (3-10) and (3-19), the largest component can be obtained when $m = 1$. Based on (3-21), the rotating speed remains constant. For generating the largest back EMF, the PPN and the speed of the regular winding should satisfy

$$p_{wr} = p_{ro} \tag{3-22}$$

$$\Omega_{wr} = \Omega_{PMSM} = \Omega_{ro} \tag{3-23}$$

For shortening the end winding and reducing the cogging torque, the fractional-slot configuration with coil pitch of one slot is often used, where the following relationship of p_{ro} and the slot number of stator Z is often used:

$$p_{ro} = p_{wr} = \frac{Z}{2} \pm 1 \tag{3-24}$$

3.3.4 Power/Torque Split

When neglecting the losses and defining the reference direction of torque and speed as the counter-clockwise direction, according to the law of energy conservation, the power and torque relationships of the outer rotor can be given as follows:

$$T_{wm}\Omega_{wm} + T_{rom}\Omega_{ro} + T_{ri}\Omega_{ri} = 0 \tag{3-25}$$

$$T_{wm} + T_{rom} + T_{ri} = 0 \tag{3-26}$$

where T_{wm} is the electromagnetic torque produced by the modulated winding, T_{rom} is the outer rotor torque produced by the modulated winding, and T_{ri} is the inner rotor torque. With (3-17), (3-18), (3-25), and (3-26), the following torque-PPN relationship can be obtained as

$$T_{wm}: T_{rom}: T_{ri} = p_{wm}: (-3p_{ro}): p_{ri} \tag{3-27}$$

The overall torque of the outer rotor T_{ro} can be calculated as

$$T_{ro} = T_{rom} + T_{ror} \tag{3-28}$$

where T_{ror} is the outer rotor torque produced by the regular winding.

3.3.5 Winding Decoupling Design

For dual-electrical-port machines, avoiding the coupling between two sets of winding is very essential, especially when two windings are placed in the same slots. The most effective way of decoupling is to use the winding factor as a filter. When the winding factor of one winding's PPN is zero for the other winding, two windings are decoupled [107]. In this design, the slot/pole combination of 24/2 for modulation winding and 24/11 for regular winding are chosen. The winding factors of the working harmonics in two sets of winding are calculated based on the method in [119] and listed in Table 3-1. It can be observed that the modulation winding can effectively eliminate the harmonics from the regular winding, and vice versa. Therefore, two sets of winding can work independently without influencing each other.

Table 3-1. Winding factors of two sets of windings in BLDDM.

Harmonic order	k_w for modulation winding	k_w for regular winding
2	0.9659	0
13	0	0.9459

3.4 Primitive Case Study and Geometrical Parameter Optimization

In this section, an initial model is first designed and analysed using both analytical methods and finite element method (FEM) to prove the validity of the principles in Section 3.3. Then, the initial model is further optimized by the FEM combining NSGA-II. The parameters of the model are listed in Table 3-2 and are labelled in Fig. 3-5.

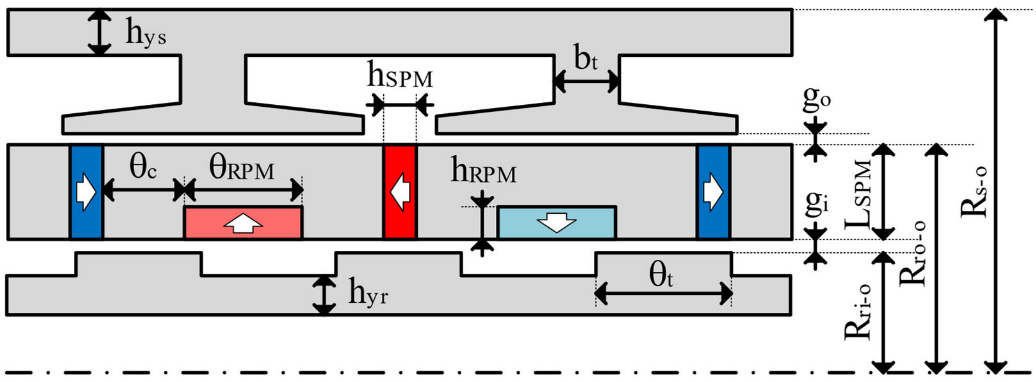

Fig. 3-5. Notation of the geometrical parameters of the design.

Table 3-2. Parameters of the models

Item	Notation	Type	Initial design	Optimal design
Stator radius	R_{s-o}	Constant	105 mm	
Outer rotor radius	R_{ro-o}	Variable	72 mm	69 mm
Inner rotor radius	R_{ri-o}	Variable	60 mm	58 mm
Outer airgap length	g_o	Constant	1 mm	
Inner airgap length	g_i	Constant	1 mm	
Stator tooth width	b_t	Variable	10 mm	8 mm
Stator yoke width	h_{ys}	Variable	15 mm	12 mm
Rotor yoke width	h_{yr}	Variable	10 mm	20 mm
Radial-PM angle	θ_{RPM}	Variable	6 °	7.2 °
Radial-PM thickness	h_{RPM}	Variable	5.3 mm	4.5 mm
Outer rotor core angle	θ_c	Variable	3.41 °	2.5 °
Spoke-PM thickness	h_{SPM}	Variable	3.4 mm	4.3 mm
Spoke-PM width	L_{SPM}	Variable	11 mm	10 mm
Inner rotor tooth angle	θ_t	Variable	5.81 °	3.72 °
Stack length	L_{stk}	Constant	50 mm	

3.4.1 Analytical analysis

As mentioned in Section 3.3.2, $PPN_{MGM(3,-1)} = (3p_{ro} - p_{ri})$, because $E_{(3,-1)} > E_{(1,-1)}$. For explaining the principle of the design reasonably, we can observe the back EMF of designs, which can be expressed as the following form when neglecting the iron core saturation:

$$E_{(n,l)} = \frac{\sqrt{2}}{2} D L_{stk} N_t \left(k_{w(n,l)} B_{(n,l)} \Omega_{(n,l)} \right) \tag{3-29}$$

where D is the diameter of the outer airgap circumference, N_t is the number of turns in one phase, $k_{w(n,l)}$ and $B_{(n,l)}$ are the winding factor and the amplitude of the flux density of the $(np_{ro} + lp_{ri})$-th component. In (3-29), except for the variables in the bracket, the other variables are all fixed by the dimensions of the machine.

The winding factors of two designs can be freely configured, and they are usually close to 1, thus the winding factor of two designs can be considered as equal. Therefore, the product of the flux density amplitude and the rotating speed will determine the amplitude of the back EMF. According to (3-13), the ratio of two flux density amplitudes can be given by

$$\frac{B_{(3,-1)}}{B_{(1,-1)}} = \frac{F_3\Lambda_1}{F_1\Lambda_1} = \frac{F_3}{F_1} \tag{3-30}$$

By substituting the dimensions of the initial design from Table 3-2 into (3-5), (3-9), and (3-29), the ratio between two harmonics can be calculated as

$$\frac{B_{(3,-1)}}{B_{(1,-1)}} \approx 4.28 \tag{3-31}$$

From (3-31), it can be observed that the flux density of the proposed design is much higher than that of the conventional one. This is because of the proposed design's outer rotor configuration. When a radially magnetized PM is inserted into the middle of the iron pole, the amplitude of the $(3p_{ro} - p_{ri})$-th harmonic has been greatly increased and even exceeded that of the conventional $(p_{ro} - p_{ri})$-th harmonic.

From (3-16), since two rotors rotate in opposite directions, $\Omega_{MGM(3,-1)} > \Omega_{MGM(1,-1)}$. Therefore, as the amplitude of the flux density and the rotation speed of $PPN_{MGM(3,-1)}$ are both higher than those of $PPN_{MGM(1,-1)}$, $(3p_{ro} - p_{ri})$ should be selected as the PPN for the modulation winding.

3.4.2 FEM Validation

To validate the analysis mentioned above, an initial model is built and analysed by FEM based on the above assumptions. The dimensions are labelled in Fig. 3-5. Notation of the geometrical parameters of the design., and the initial parameters are listed in Table II. The flux density waveforms of the inner and outer airgap and their harmonics based on fast Fourier analysis are shown in Fig. 3-6(a) and Fig. 3-6(b), respectively.

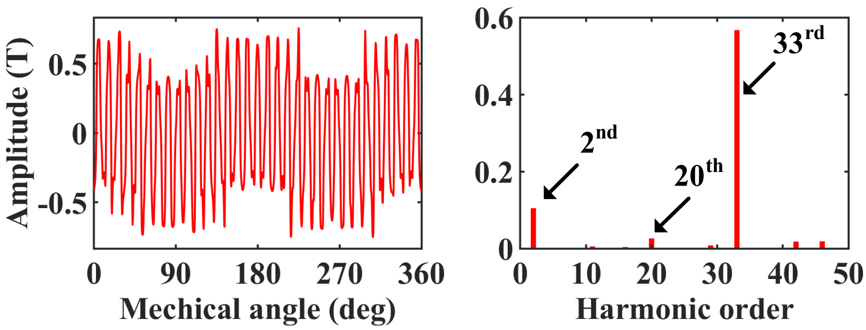

(a)

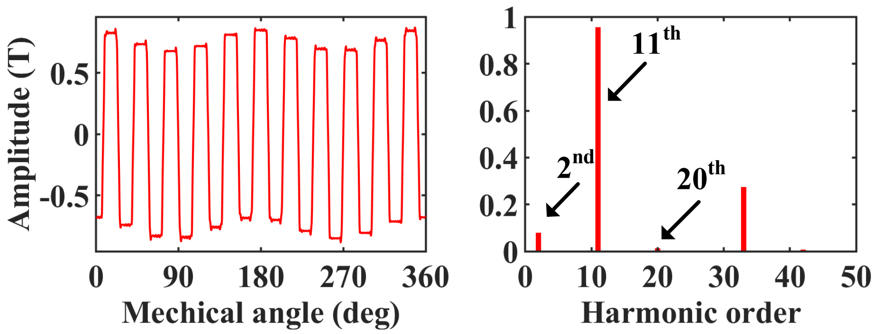

(b)

Fig. 3-6. Flux density of the initial design. (a) Inner airgap. (b) Outer airgap.

It can be observed that the third harmonic component, namely 33rd component dominates the inner airgap field, and the fundamental component, namely 11th component dominates the outer airgap. This has validated the principle of the outer rotor configuration.

The amplitude of the two working harmonics is listed in Table III, where $B_{(1,-1)}$ and $B_{(3,-1)}$ are the amplitudes of the 20th and 2nd components. The ratio of $B_{(3,-1)}$ and $B_{(1,-1)}$ in the inner airgap is 4.16, which agrees with the result of the analytical analysis in (3-31).

Table 3-3. The amplitude of the main working harmonic components in both airgaps

Item	$B_{(1,-1)}$	$B_{(3,-1)}$	$\frac{B_{(3,-1)}}{B_{(1,-1)}}$
Inner airgap	0.025 T	0.104 T	4.16
Outer airgap	0.013 T	0.079 T	6.07

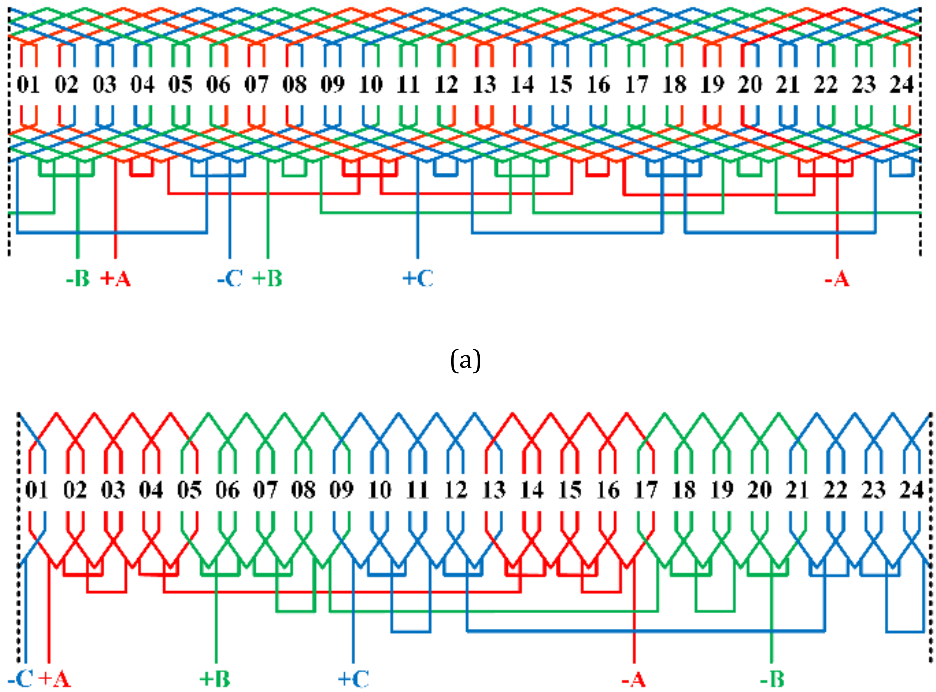

(a)

(b)

Fig. 3-7. The winding diagram. (a) Modulation winding. (b) Regular winding.

Both $B_{(1,-1)}$ and $B_{(3,-1)}$ attenuated in the outer airgap. As the PPN of $B_{(3,-1)}$ is small, more $B_{(3,-1)}$ flux goes into the stator core due to the flux barrier effect in the outer rotor [120, 121]. $B_{(1,-1)}$ attenuated more because its PPN is closer to the number of the iron core of the outer rotor, which can cause more flux leakage. Therefore, the ratio of two components in the outer airgap is greater than that of the inner airgap. The winding diagram is shown in Fig. 3-7.

3.4.3 Optimization

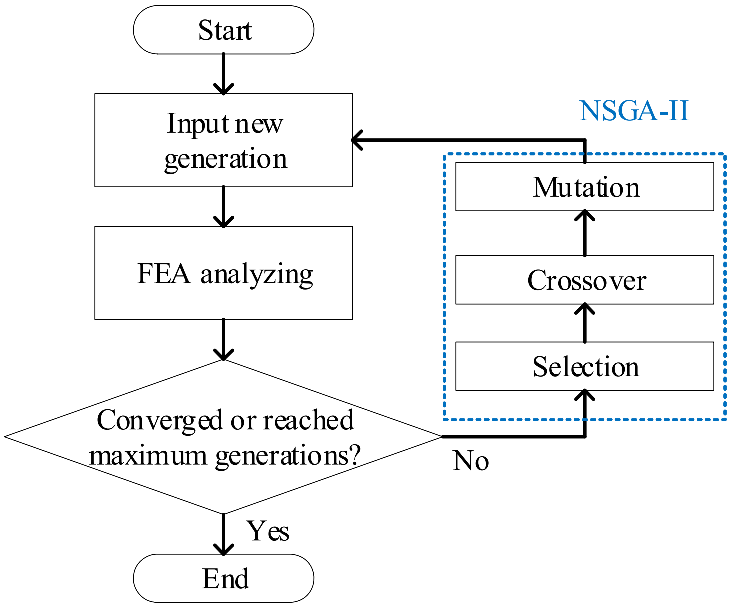

Fig. 3-8. The optimization flowchart using FEA and NSGA-II.

To obtain better electromagnetic performance for the proposed design, the geometric parameter of the BLDDM model is optimized. The optimization goals are to maximize the output torque density K_T and minimize the maximum torque ripple ratio T_{rip}, where K_T and T_{rip} are defined as

$$K_T = \frac{T_{ro-avg}}{V} \tag{3-32}$$

$$T_{rip} = \frac{\max(T_{rip-o}, T_{rip-i})}{T_{ro-avg}} \tag{3-33}$$

where T_{ro-avg} is the average torque of the outer rotor, V is the electromagnetic part volume of the machine, T_{rip-o} and T_{rip-i} are the peak-to-peak torque ripple of outer and inner rotor, respectively. As this is a multi-objective optimization, in this paper, FEM is used combining the non-dominated sorting genetic algorithm II (NSGA-II). The flowchart of the optimization process is shown in Fig. 3-8.

The optimization in this model has 20 generations, with 100 designs in each generation as a trade-off between reaching the global optimization and shorter calculation time. The current density of the modulation and regular winding is 6A/mm ^{2}. All Pareto fronts of optimization are shown in Fig. 3-9, with the colour showing the generation of each sample. From Fig. 3-9, it can be observed that the results are becoming more concentrated in a single line from the previous scattered form when the generation increases. The Pareto fronts of the last five generations increase very little and lie basically on the same line, and the results are more concentrated, thus the optimization is converged and successful. The circled design is selected considering the trade-off between torque density and ripple. The optimized parameters are listed in Table 3-2. Parameters of the models, and the results are shown in Table 3-4. Performance comparison of the initial and optimal models. Compared to the initial design, the output torque density has increased 33% and the maximum torque ripple has decreased 15%.

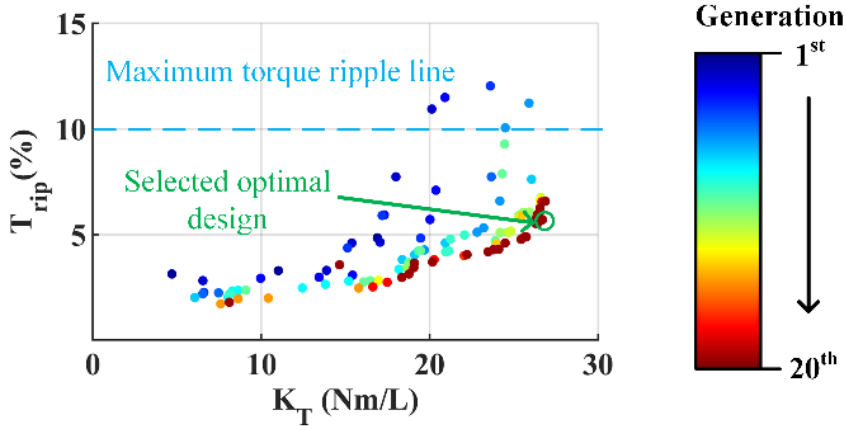

Fig. 3-9. The Pareto fronts of the proposed design's optimization.

Table 3-4. Performance comparison of the initial and optimal models

Item	Initial design	Optimal design
K_T	20.04 Nm/L	26.64 Nm/L
T_{rip}	6.77%	5.72%

3.5 Performance Comparison and Analysis

To showcase the improvement of the proposed BLDDM, a conventional model based on [94] is designed and optimized, and the electromagnetic performances of two optimized machines are compared by FEM. For a fair comparison, the winding design, PM volume, and machine volume of two designs are the same. The main dimensions of two models are listed in Table V. For the labels in the following figures, "prop." and "conv." refer to the proposed and conventional designs, respectively. The pareto fronts of the conventional designs is shown in Fig. 3-10. The optimization configuration and procedure of the conventional and the proposed design are the same.

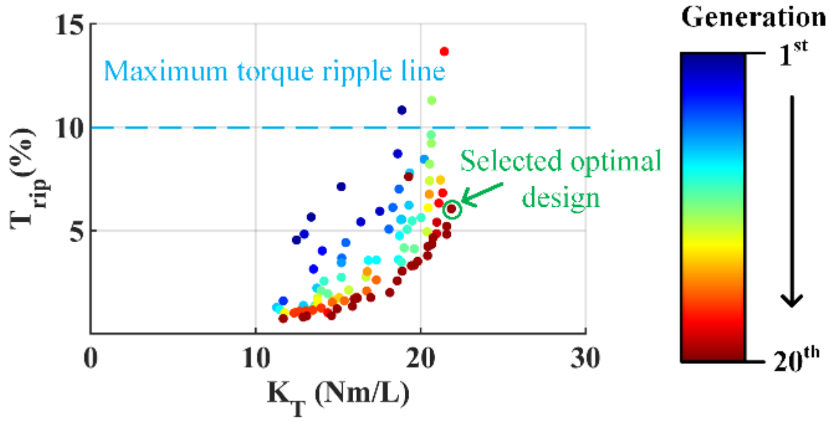

Fig. 3-10. The Pareto fronts of the conventinoal design's optimization.

Table 3-5. Main dimensions of the proposed design and conventional design

Item	Prop. BLDDM	Conv. BLDDM
Stator outer diameter	210 mm	
Stack length	50 mm	
Airgap length	1 mm	
Slot number (Z)	24	
PPN of outer rotor spoke-PMs (p_{ro})	11	
PPN of outer rotor radial-PMs	11	N/A
No. of inner rotor teeth (p_{ri})	31	9
PPN of modulation winding	2	
PPN of regular winding	11	
PM volume	86.5 cm ^{3}	

Outer rotor speed	200 rpm
Inner rotor speed	-300 rpm
Modulation winding turns	22
Regular winding turns	22
Rated current density	6 A/mm ^{2}
Power level	~2kW
Magnet material	N40UH
Silicon steel sheet	35WW300

3.5.1 No-load Comparison and Analysis

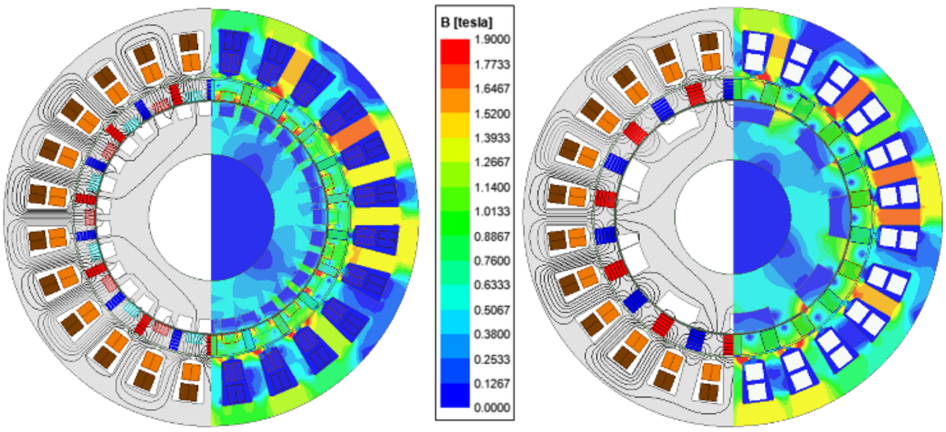

(a) (b)

Fig. 3-11. Comparison of no-load flux line distribution and on-load flux density map. (a) Proposed design. (b) Conventional design.

The flux line distributions are shown in the left portion of Fig. 3-11. A 2-pole-pair modulated field can be observed in the inner rotor. The flux line in the stator is the mixture of a 2-pole-pair and an 11-pole-pair field.

Fig. 3-12 shows the airgap flux density waveforms and the harmonic distribution of the proposed and conventional designs in the outer airgap. The back EMF waveforms and their harmonic distributions of the proposed and conventional designs for the regular and modulation windings are shown in Fig. 3-12 and Fig. 3-13, respectively.

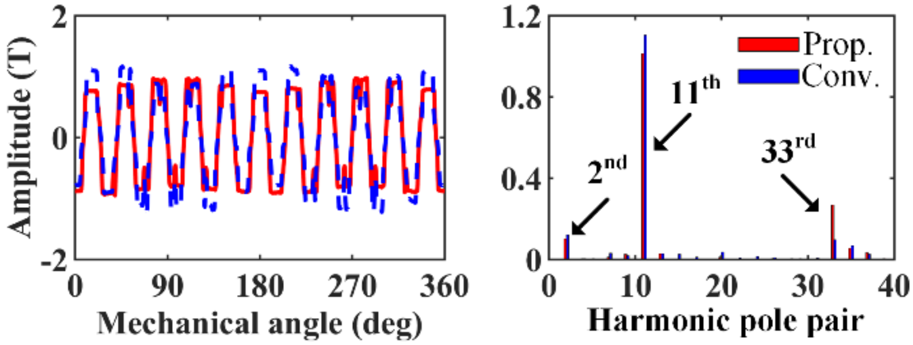

Fig. 3-12. Comparison of the outer airgap flux density.

From Fig. 3-12, the 2^{nd} and 11^{th} components are the dominant components that match the modulation winding and the regular winding. The 11^{th} flux density component of the proposed design is 7% marginally smaller than that of its conventional counterpart. As their field rotation speed is the same, the back EMF of the proposed design is just 5% smaller than that of the conventional design, shown in Fig. 3-13.

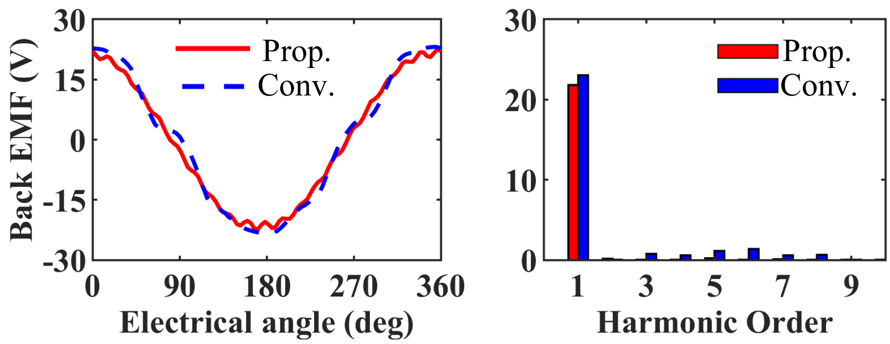

Fig. 3-13. Comparison of regular winding back EMF.

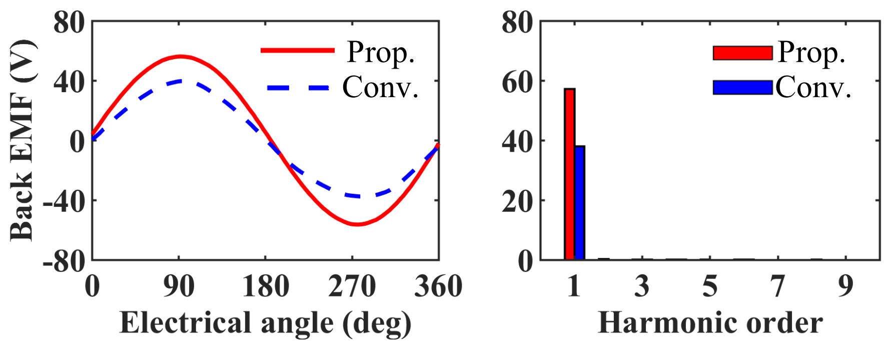

Fig. 3-14. Comparison of modulation winding back EMF.

The amplitude of the 2nd component in the proposed design is 0.08T, which is also slightly lower than that of the conventional design 0.13T. However, the field rotation speed of the proposed design is three times higher than its conventional counterpart because it is the third-harmonic component that is modulated with the salient teeth. Therefore, the back EMF of the proposed design is 50% higher than that of the conventional design, shown in Fig. 3-14.

The amplitude of the 2nd component in the proposed design is 0.08T, which is also slightly lower than that of the conventional design 0.13T. However, the field rotation speed of the proposed design is three times higher than its conventional counterpart because it is the third-harmonic component that is modulated with the salient teeth. Therefore, the back EMF of the proposed design is 50% higher than that of the conventional design, shown in Fig. 3-14.

Although there is a relatively high 33rd component, which is the third harmonic of the 11th component, shown in Fig. 3-12, as the regular winding is a three-phase Y-connected winding, all the 3k-th components are eliminated. It will also not affect modulation winding due to winding factor filtering, as mentioned in Section 3.3.5.

3.5.2 On-load Comparison and Analysis

The knee point of the irreversible demagnetization is about for N40UH magnets at 120˚C is -0.27T, which means that when PMs are demagnetized, the direction of the flux density vector is opposite to the original magnetization direction. From Fig. 3-15, it is shown that all flux density vectors are in the same directions as the PMs, thus no demagnetization exists.

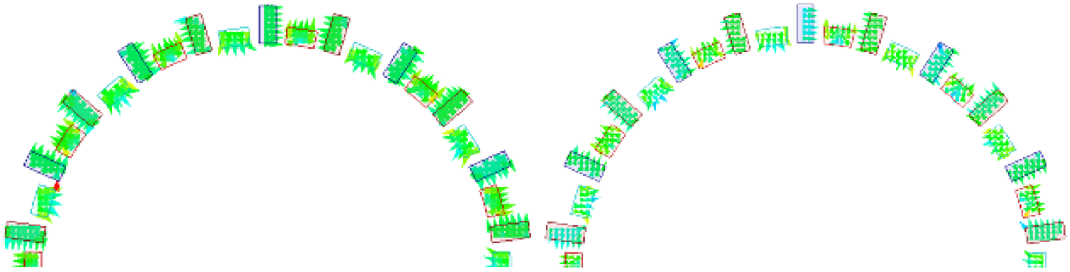

(a) (b)

Fig. 3-15. Flux density vectors at no load and full load condition. (a) No load. (b) Full load.

Fig. 3-15 presents the flux density vectors at no load and full load condition. The flux density map of the two designs is presented in the right portion of Fig. 3-11. The current density of both windings is 6A/mm ^{2}, which is suitable for air cooling. The maximum flux density of the stator teeth body and the yoke in both designs is below 1.7T, which is lower than the knee point of the silicon steel sheet. There are some local saturation areas on the tooth tips that the flux density due to the trade-off between limited tip geometry size and larger slot area. As the saturation area is relatively small, its impact on the main flux is limited, thus can be neglected.

The average torque and the torque ripple of both the proposed and conventional designs under the rated conditions are sorted in Table 3-6. Comparison of the rated output torque. When only the regular winding is injected, the output torque of the PMSM portion in the proposed design is just 5.5% lower than that of the conventional design. When only the modulation winding is injected, the output torque of the MGM portion in the proposed design is 45.7% higher than that of the conventional design. When regular and modulation windings are both injected, the overall output torque of the proposed design is 13.6% higher than that of the conventional design. Although the torque ripple for the PMSM and MGM portions is relatively large in both the proposed and conventional design, the overall torque ripple is relatively small, which is less than 10% of the average torque.

Table 3-6. Comparison of the rated output torque

Item	Proposed design		Conventional design	
	Average	Ripple	Average	Ripple
PMSM portion	22.72 Nm	1.89 Nm	24.04 Nm	2.62 Nm
MGM portion	25.22 Nm	3.28 Nm	17.31 Nm	1.57 Nm
Overall	45.39 Nm	2.53 Nm	39.94 Nm	1.98 Nm

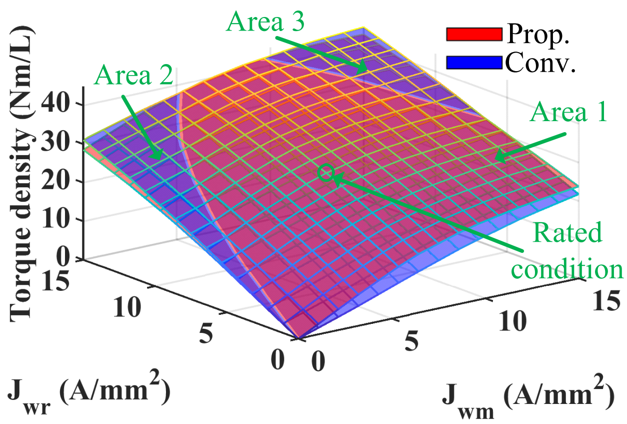

Fig. 3-16. Comparison of the outer rotor torque density.

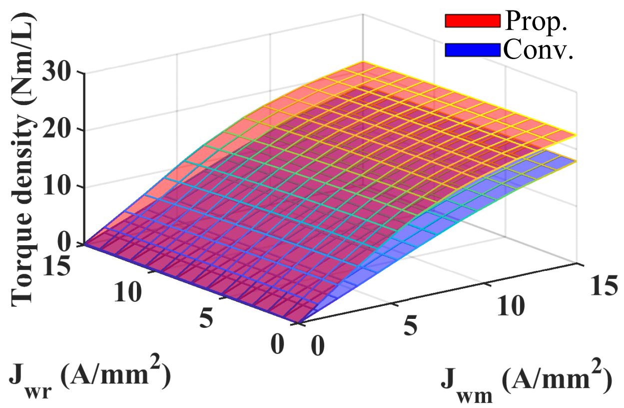

Fig. 3-17. Comparison of the inner rotor torque density.

Under different current injections in the regular and modulation windings, the torque density of the outer and inner rotors for the proposed and conventional designs are shown in Fig. 3-16 and Fig. 3-17, where J_{wr} and J_{wm} are the current densities of the regular and modulation windings. From Fig. 3-16, area 1 covers the rated and most conditions. It can be observed that the torque density of the proposed design is higher than that of the conventional design in this area. The torque improvement reaches its maximum variation of 58.70% in area 1 near the rated condition. For area 2, the MGM portion of the torque is relatively small due to low J_{wm}. As the MGM portion torque plays an important role in the overall torque of the proposed design, the torque density of the proposed design is lower than that of the conventional design. For area 3, when both windings are injected with high current, the outer rotor of the proposed design is more saturated, and thus the torque density of the conventional design is higher than that of the counterpart in certain overload condition. However, the maximum variation is 8.24% in area 2 and 4.28% in area 3, which is relatively small compared to the maximum variation in area 1.

From Fig. 3-17, it can be noticed that the torque density of the proposed design is higher than that of the conventional counterpart under various J_{wm}. As J_{wr} only controls the torque of the PMSM portion of the outer rotor, it is not related to the torque of the inner rotor.

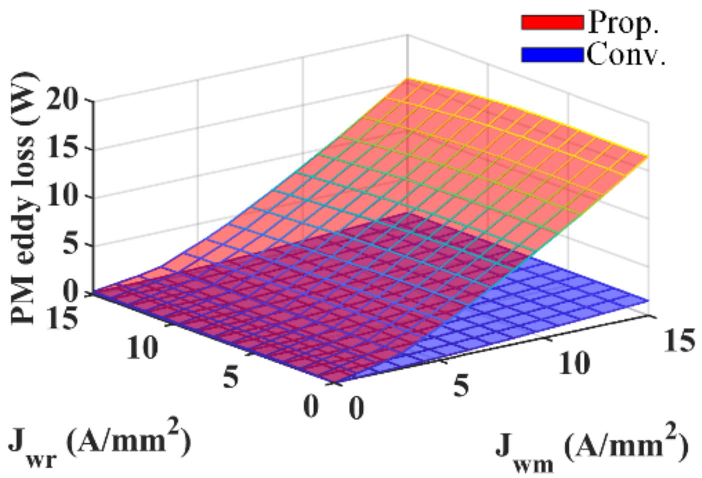

Fig. 3-18. Comparison of PM eddy current loss.

The comparison of PM eddy loss between the proposed and conventional designs under the rated speed is shown in Fig. 3-18. Compared to the regular winding current, the modulation winding current plays a dominant role in the PM eddy loss. Because the flux density of both designs is almost equal, and the frequency of the proposed design's modulation winding is 3.24 times of the conventional one, the PM eddy loss of the proposed design is about 10 times of the conventional design. The comparison of the output power is shown in Fig. 3-19, where it can be calculated that the PM eddy loss of both designs is less than 1% of the output power, which has minor effect to the performance of PMs. The comparison of the efficiency is shown in Fig. 3-20. In the rated condition, the efficiency of the proposed and conventional designs is 92% and 94%, respectively.

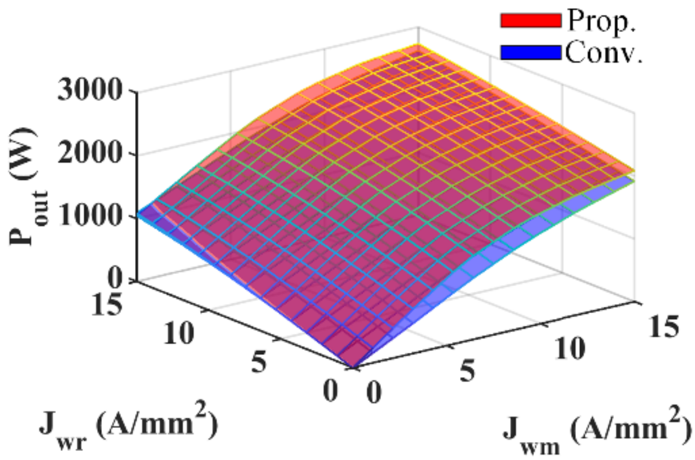

Fig. 3-19. Comparison of the output power.

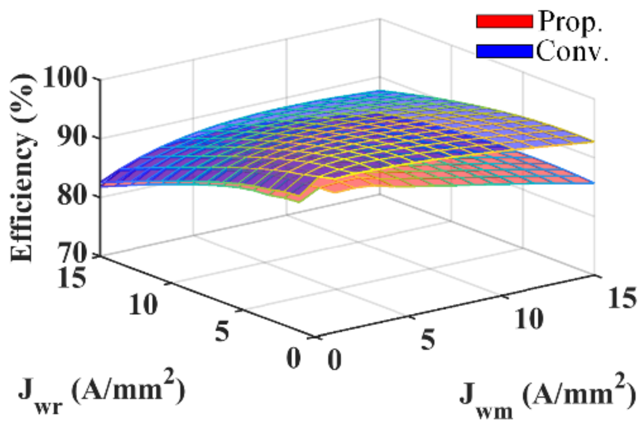

Fig. 3-20. Comparison of the efficiency.

3.6 Experiment Validation

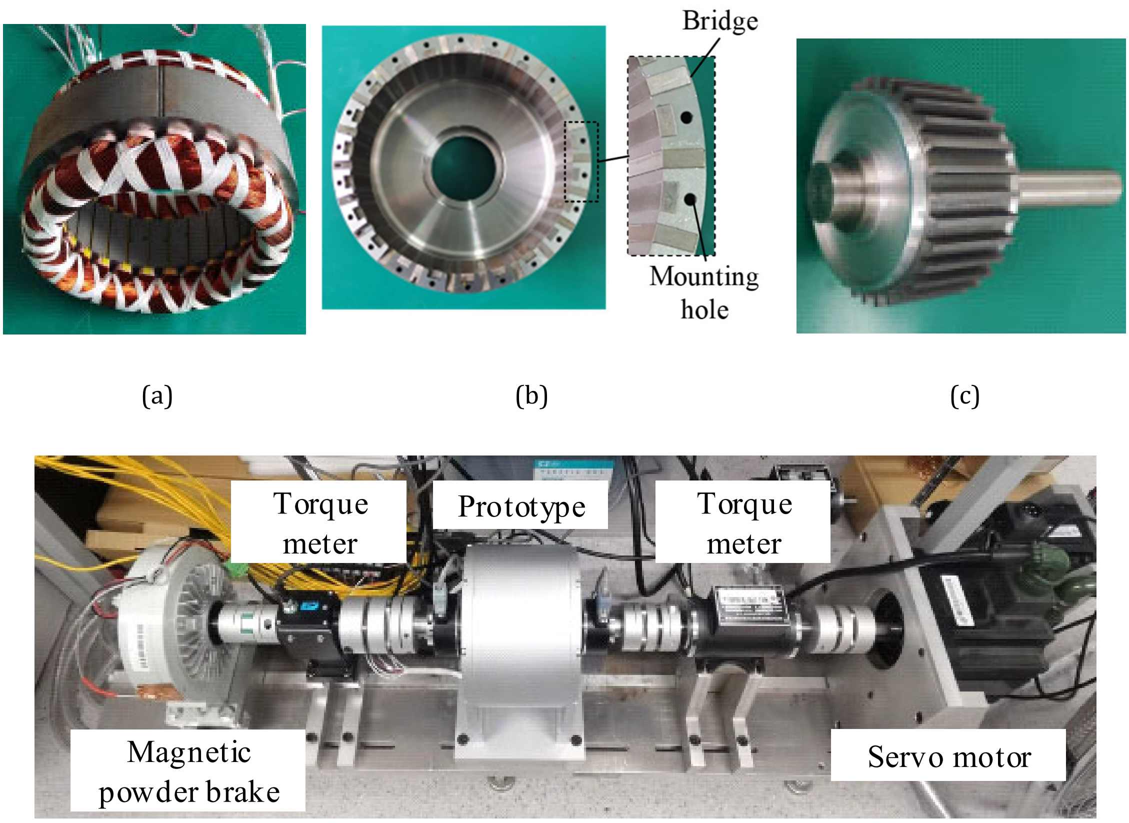

(a) (b) (c)

(d)

Fig. 3-21. Photos of the prototype. (a) Stator. (b) Outer rotor. (c) Inner rotor. (d) On-load test bench.

A prototype is built to validate the feasibility of the proposed BLDDM, shown in Fig. 3-21. To enhance the mechanical strength of the outer rotor, mounting holes and the flux bridge are added to make the airgap uniform incase the eccentricity caused by the PMs on the outer rotor happens. As the iron bridge is easily saturated, it has minor effect on the proposed design. Fig. 3-21(d) shows the on-load test bench. The experiment setup is shown in Fig. 3-22. The inverters are fed by the DC power supply and controlled by controller, which can output power to the prototype according to the control strategy. The servo driver is also controlled by controller and output power to the servo motor. It is connected to the inner rotor, which simulates the prime mover in this scenario. The brake controller can be freely adjusted through controller. The magnetic powder brake is connected to the outer rotor, which enables it to work as the load. The control diagram is shown in Fig. 3-23. This machine uses the conventional field-oriented control.

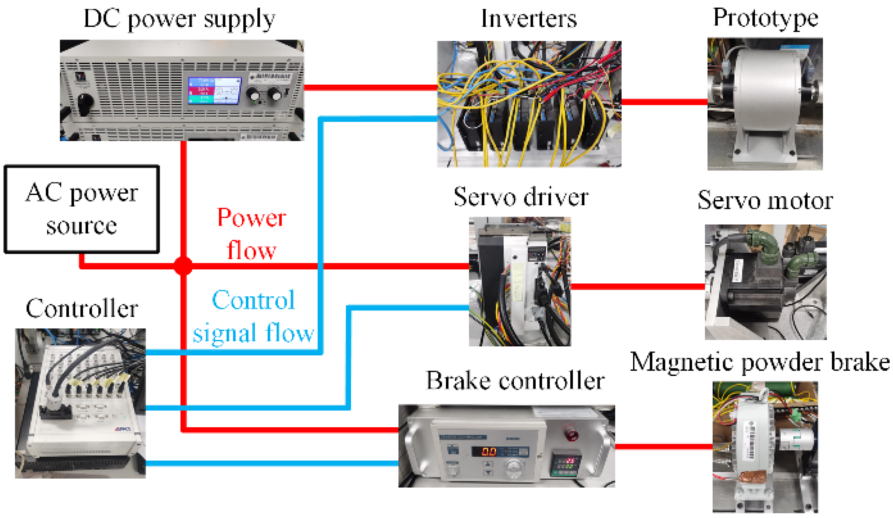

Fig. 3-22. Schematic of experiment setup.

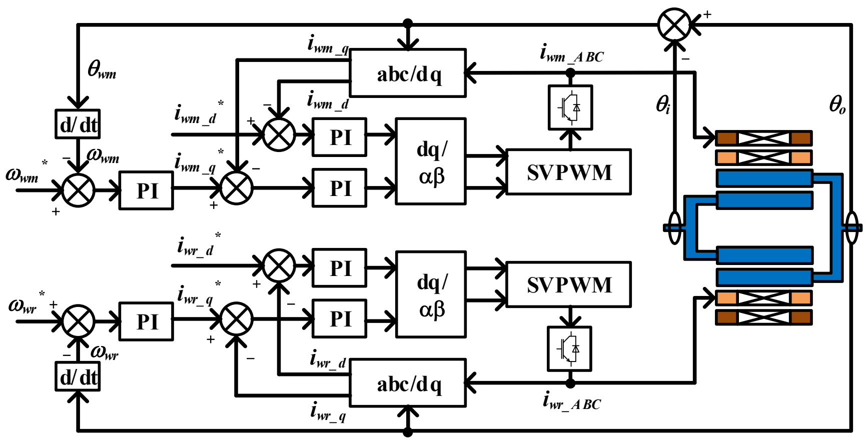

Fig. 3-23. Control diagram of the proposed BLDDM.

Table 3-7. Comparison of the FEM and experimental back EMF amplitude

Ω_{ro}	Ω_{ri}	Modulation winding		Regular winding	
		FEM	Exp.	FEM	Exp.
100 rpm	0 rpm	13.61 V	13.06 V	11.11 V	10.97 V
100 rpm	-100 rpm	23.19 V	22.11 V	11.12 V	11.01 V
75 rpm	-300 rpm	41.57 V	41.60 V	7.64 V	7.61 V
200 rpm	-300 rpm	58.39 V	56.28 V	20.63 V	20.90 V

The measured no-load back EMF waveforms are presented in Fig. 3-24. Fig. 3-24(a) shows the back EMF waveforms of the modulation winding at different speeds. The single turn area is 1.41mm^2, and when the current reaches 8.5A, the current density is 6A/ mm^2. The curves are sinusoidal and the amplitude and the frequency vary according to the speed of the two rotors, respectively. Fig. 3-24(b) shows the back EMF waveforms of the regular winding with different speeds. It can be revealed from Fig. 3-24(b) that the regular winding back EMF is only related to the speed of the outer rotor. The comparison of the FEM and experimental back EMF amplitude is added, presented in Table 3-7. The measured bank EMF results agree with the previous FEM results in Section 3.5, where the maximum deviation of the amplitude is less than 5%.

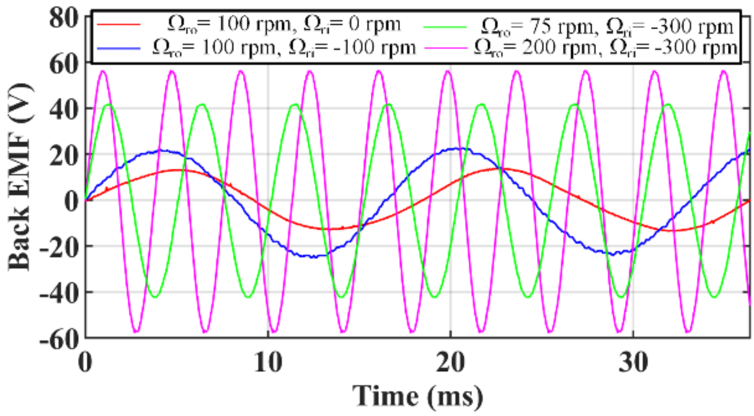

(a)

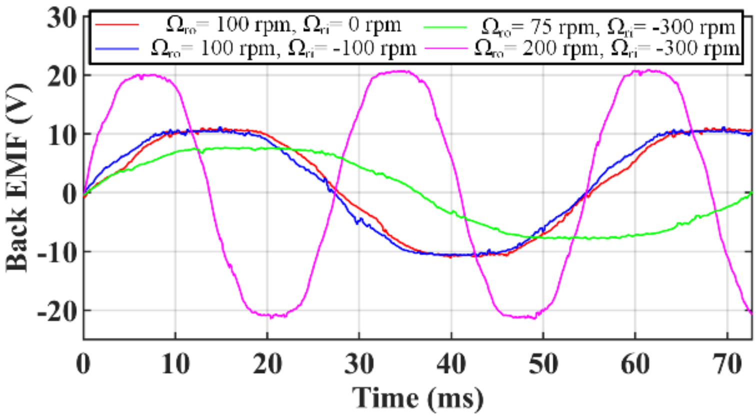

(b)

Fig. 3-24. Measured no-load back EMF waveforms. (a) Modulation winding. (b) Regular winding.

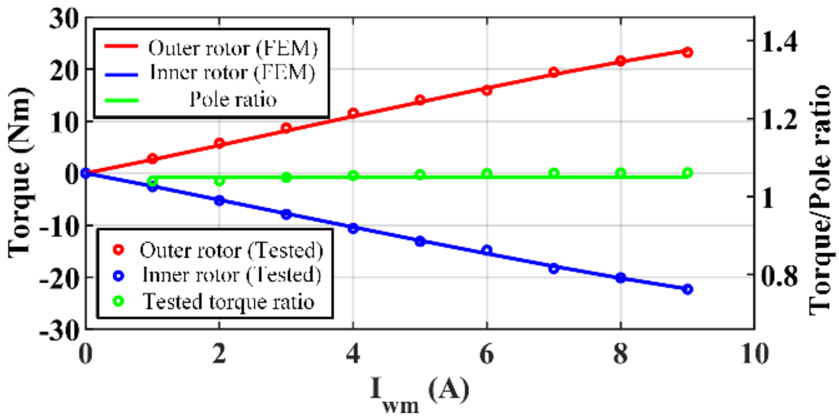

(a)

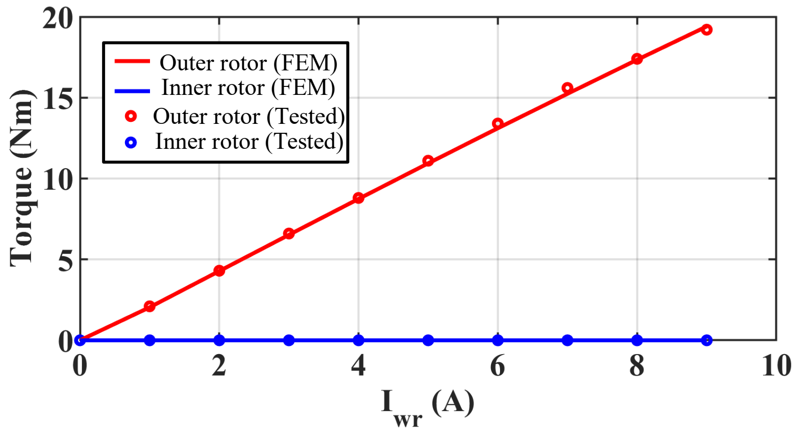

(b)

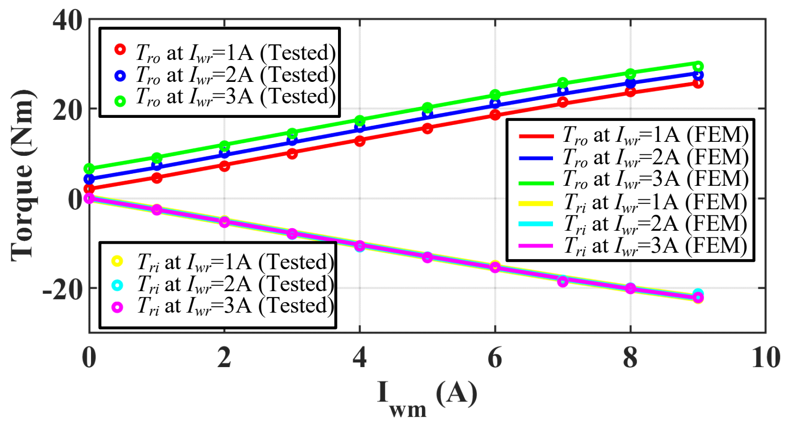

(c)

Fig. 3-25. Measured torque-current waveforms. (a) Only modulation winding excited. (b) Only regular winding excited. (c) Both winding excited.

The torque characteristics are presented in Fig. 3-25. When only the modulation winding is injected, the electromagnetic torque is produced on both rotors proportionally, as shown in Fig. 3-25(a). The torque ratio is also close to the pole ratio, which agrees with (3-26). When only the regular winding is injected, the torque is only produced on the outer rotor, shown in Fig. 3-25(b). Fig. 3-25(c) presents the torque of two rotors with different modulation winding currents when the regular winding current is set. The torque-current curves of the outer rotor are parallel to each other and increased proportionally according to the regular winding current. The curves of the inner rotor overlapped, which reveals that the regular winding current is unrelated to the inner rotor torque. The experiment results agree with the FEM simulations with a maximum deviation of 6.8%.

3.7 Summary

A novel BLDDM structure using a high-order harmonic modulation is proposed in this paper to further improve the torque density of the MGM portion of BLDDM. The key is that the outer rotor is artificially designed to enhance the third-harmonic component of airgap flux density in the inner airgap while remaining the fundamental component unchanged in the outer airgap. Both components can be fully used by two windings in this design. By analyzing the modulation effect with the analytical method and FEM, the flux density ratio of the third harmonic and the fundamental components is about 4.28, and the rotating speed ratio is 3, making it feasible to determine the PPN of modulation winding as $p_{wm} = 3p_{ro} - p_{ri}$. The prototype is optimized and compared with the conventional design with the same dimensions and PPN of two windings by FEM, whose result shows that the proposed design has 50% higher back EMF in modulation winding and 45.7% larger MGM portion torque. Finally, a prototype is manufactured and tested. The experiment results agree with the working principles and FEM simulations.

Chapter 4 A High-Order-Harmonic Compound Rotor Based Permanent Magnet Brushless Machine for Variable Speed Constant Frequency Wind Power Generation

4.1 Introduction

With escalating environmental concerns and the prevailing energy crisis, there has been a notable shift towards substituting power generation systems reliant on fossil fuels with renewable energy sources [122, 123]. Within this context, wind power generation systems have garnered significant attention within the industrial sector, experiencing rapid advancements over the past few decades due to their cost-effectiveness and sustainable nature.

Given the inherent variability of wind speeds due to natural factors, maintaining a consistent frequency in the electrical output port connected to the grid call for the development of specific technologies. These technologies, referred to as variable speed constant frequency (VSCF) operation, enable wind power generation systems to sustain a constant industrial frequency in the output electrical port, regardless of fluctuations in the input speed of the mechanical port. [124]

The doubly fed machine (DFM) is a commonly employed method in industrial applications to achieve VSCF operation. The initial development and widespread use of the doubly fed induction machine (DFIM) can be attributed to its cost-effectiveness and high controllability. However, conventional DFIMs rely on controlling the windings on the rotor to regulate the output frequency, necessitating the use of wound-rotor and slip rings. The slip ring mechanism presents challenges related to direct contact, which requires regular mechanical maintenance due to wear and tear.

To overcome the mechanical structure-related issues, several brushless doubly fed machine (BLDFM) have been proposed, including self-cascaded DFIM [125], dual-stator DFIMs [126, 127], nest-loop rotor based DFIM [128, 129], and brushless double fed reluctance machine (DFRM) [130, 131]. Nevertheless, many of these brushless structures suffer from drawbacks such as low power density and low efficiency.

Recent advancements in flux modulation theory have led to the development of brushless dual-electrical-port dual-mechanical-port DFMs (BLDD-DFMs). The commonly used magnetic-geared (MG) type BLDDM consists of a magnetic-geared machine (MGM) and a permanent magnet synchronous machine (PMSM) part. The PMSM part is responsible for power generation, while the MGM part maintains a constant output frequency. However, a design proposed in [132], where the stator and inner rotor form the PMSM part with the outer rotor placed between them, results in a considerably longer flux path for the PMSM part, leading to reduced performance. To address this issue, a dual-PM bidirectional flux modulation structure with two consequent-pole PM rotors is proposed and analyzed in [87, 101]. In this design, the stator and outer rotor form the PMSM part, significantly enhancing its performance. Furthermore, [91] and [115] replace the radial PM on the outer rotor with the spoke PM, further shortening the flux path and increasing the torque density of the PMSM part. Another design in [133] suggests substituting the PMSM part with a permanent magnet Vernier machine

(PMVM) part, further improving power generation performance. Unfortunately, the MGM part, responsible for frequency control in BLDFMs, typically suffers from low torque density due to limited utilization of flux harmonics, which is an aspect that has not received much attention in the industry. Enhancing the performance of the MGM part can lead to energy savings in the control system and overall system efficiency improvement.

In [117], a novel high-order harmonic winding design is proposed for the Vernier reluctance machine. The authors design a novel winding using the harmonics higher than the fundamental one, i.e., the high-order harmonic winding. A BLDDM based on the high-order harmonic is designed in [97] to further enhance the torque density of the MGM part while maintaining the same amount of PM material. Using the same concept, a BLDDM-based BLDFM using high-order harmonic winding can also be designed for VSCF applications.

This chapter presents an extension of the aforementioned concept in Chapter 3 by proposing a novel BLDD-DFM structure for VSCF wind power applications. The proposed structure incorporates high-order harmonic modulation to minimize energy consumption in the control winding. The primary focus is on artificially enhancing the third-harmonic component of the airgap flux density in the inner airgap, while maintaining the fundamental component unchanged in the outer airgap. Both components are effectively utilized by two windings in this design. The paper is organized as follows. In Section 4.2 and 4.3, the machine structure and the operating principle are introduced. In Section 4.4, the proposed BLDDM is compared with the conventional design in other literature in terms of the torque and working principle. In Section 4.5, a prototype is made, and the experiment results verify the feasibility and advantages of the proposed design. Finally, summary is concluded in Section 4.6.

4.2 Machine Structure

Fig. 4-1 shows the proposed doubly fed machine system, which is composed of two electrical ports and two mechanical ports, viz. two sets of winding and two concentric rotors. The stator has 24 slots, where the 2-pole-pair control winding and the 11-pole-pair power winding are placed inside. The inner rotor is connected with the wind turbine directly. It consists of only 31 iron teeth, which shows good mechanical robustness.

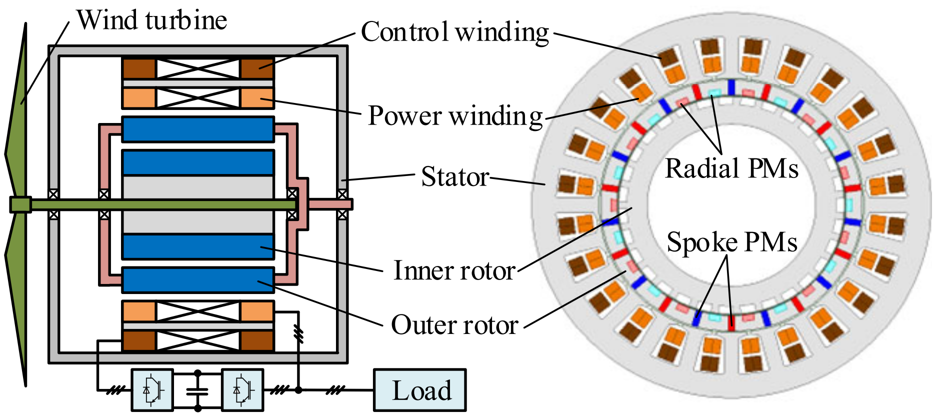

Fig. 4-1. The configuration of the BLDD-DFM system.

The outer rotor operates in idle. It has 11 pole pairs of spoke-type PMs and 11 pole pairs of radially-magnetized PMs, shown in Fig. 4-2. The iron core of the outer rotor is placed between two adjacent spoke PMs, and the radially-magnetized PM is placed in the duct along the inner side of the outer rotor. The radial-magnetized PMs are used to enhance the third harmonic component MMF in the inner airgap, while remaining the fundamental component in the outer airgap. As the MMF in the outer airgap is used for the interaction with the regular winding and the MMF in the inner airgap is used for the flux modulation with the inner rotor, the fundamental and its third harmonic components can all be fully used in this design.

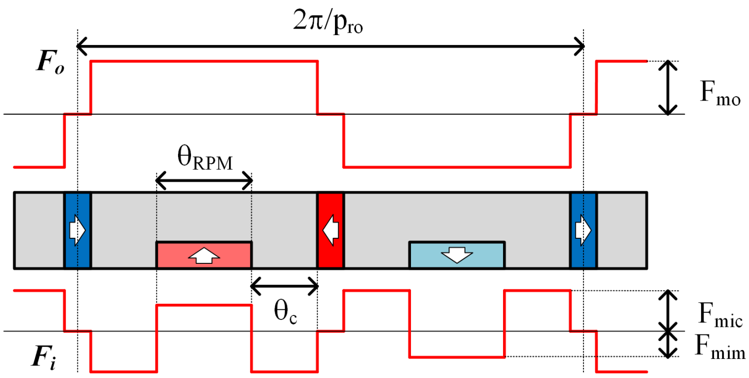

Fig. 4-2. The configuration of the outer rotor and the MMF in the inner and outer airgap.

The power winding connects to the grid directly, and the control winding connects to the grid via a converter. The BLDD-DFM system can be regarded as the combination of a magnetic-geared control machine (MGCM) and a PM synchronous generator (PMSG). The outer rotor, inner rotor, and control winding form the MGCM. By controlling the frequency of control winding, the outer rotor can rotate in a fixed speed with random inner rotor speed. The PMSG is composed of the outer rotor and the power winding, which outputs power in constant frequency. Therefore, the VSCF control is achieved.

4.3 Operating Principle

4.3.1 MEC analysis

The magnetomotive force (MMF) waveforms excited by the PMs in the inner and outer airgap with the notations are shown in Fig. 4-2. To quantitively analyze the MMF waveform, when neglecting the magnetic resistance in iron core, the magnetic equivalent circuit (MEC) can be drawn in Fig. 4-3 [94, 97], where R_o, R_{ic}, and R_{im} are the magnetic resistance of outer airgap, inner airgap under the iron core section, and inner airgap under the PM section, R_s and R_r are the internal magnetic resistance of spoke-type PM and radially-magnetized PM, F_s and F_r are the MMF of spoke-type PM and radially-magnetized PM.

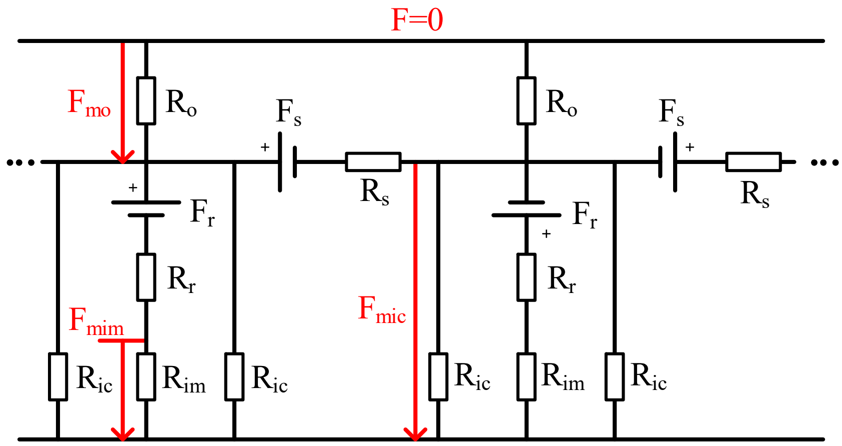

Fig. 4-3. The magnetic circuit of outer rotor.

For the convenience of analyzing, the magnetic potential of the outer iron ring is set as zero. Based on Kirchhoff's law, the following relationship can be written in the matrix form $\mathbf{AF} = \mathbf{B}$:

$$\begin{bmatrix} \frac{1}{R_0}+\frac{4}{R_s} & \frac{2}{R_{ic}} & -\frac{1}{R_{im}} \\ 0 & 1 & 1+\frac{R_r}{R_{im}} \\ 2 & -2 & 0 \end{bmatrix} \begin{bmatrix} F_{mo} \\ F_{mic} \\ F_{mim} \end{bmatrix} = \begin{bmatrix} \frac{2F_s}{R_s} \\ F_r \\ 0 \end{bmatrix} \tag{4-1}$$

Therefore, the amplitude matrix $\mathbf{F}$ can be calculated:

$$\mathbf{F} = \begin{bmatrix} F_{mo} \\ F_{mic} \\ F_{mim} \end{bmatrix} = \mathbf{A}^{-1}\mathbf{B} = \frac{1}{R_{sum}} \cdot \begin{bmatrix} R_{ic}R_o(2F_sR_{im}+F_rR_s+2F_sR_r) \\ R_{ic}R_o(2F_sR_{im}+F_rR_s+2F_sR_r) \\ R_{im}(4F_rR_{ic}R_o-2F_sR_{ic}R_o+F_rR_{ic}R_s+2F_rR_oR_s) \end{bmatrix} \tag{4-2}$$

$$R_{sum} = \frac{R_{ic}R_{im}R_oR_s}{2}\det(\mathbf{A}) \tag{4-3}$$

From Fig. 4-2, the MMF in the inner and outer airgap can be expressed by Fourier series as

$$F_i(\theta, t) = \sum_{n=1,odd}^{+\infty} F_{in}\cos(np_{ro}(\theta+\Omega_{ro}t)+\varphi) \tag{4-4}$$

$$F_o(\theta,t) = \sum_{m=1,odd}^{+\infty} F_{om}\cos(mp_{ro}(\theta+\Omega_{ro}t)+\varphi) \tag{4-5}$$

where p_{ro} is the pole pair number (PPN) of the outer rotor, which is also the PPN for both radially-magnetized and spoke-type PMs on the outer rotor, Ω_{ro} is the rotating speed of the outer rotor, φ is the initial angle of the outer rotor. F_{in} and F_{on} are the corresponding magnitude of the n-th and m-th MMF components, which can be further expressed by means of Fourier decomposition as

$$\begin{aligned} F_{in} = & \frac{8F_{mic}}{n\pi}\sin\left(np_{ro}\frac{\theta_c}{2}\right)\cos\left(np_{ro}\frac{\theta_{RPM}+\theta_c}{2}\right) \\ & -\frac{4F_{mim}}{n\pi}\sin\left(np_{ro}\frac{\theta_{RPM}}{2}\right) \end{aligned} \tag{4-6}$$

$$F_{om} = \frac{4F_{mo}}{m\pi}\sin\left(mp_{ro}\frac{2\theta_c+\theta_{RPM}}{2}\right) \tag{4-7}$$

4.3.2 MGCM part analysis

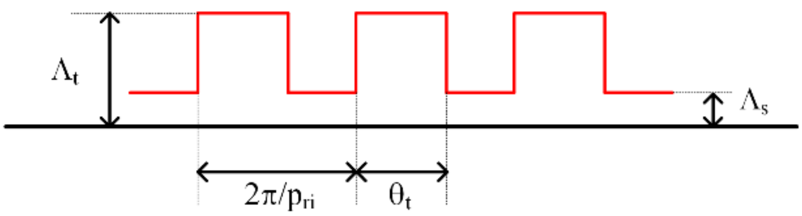

Fig. 4-4. Permeance waveform of the inner rotor.

The permeance waveform of the inner rotor in the inner airgap is shown in Fig. 4-4, which can be given as

$$\Lambda(\theta,t) = \frac{\Lambda_0}{2} + \sum_{k=1}^{+\infty} \Lambda_k\cos\left(kp_{ri}(\theta+\Omega_{ri}t)\right) \tag{4-8}$$

where p_{ri} is the number of the inner rotor's salient poles, Ω_{ri} is the rotating speed of the inner rotor, and Λ_k is the magnitude of the k-th permeance component, which can be expressed by Fourier decomposition as

$$\Lambda_k = \begin{cases} 2\Lambda_s + \frac{\theta_t p_{ri}}{\pi}(\Lambda_t-\Lambda_s), & k=0 \\ \frac{2(\Lambda_t-\Lambda_s)}{k\pi}\sin\left(\frac{kp_{ri}\theta_t}{2}\right), & k>0 \end{cases} \tag{4-9}$$

The airgap flux density of the MGCM part equals to the product of F_i and Λ, which can be expressed as

$$B_{MGCM}(\theta,t) = F_i(\theta,t)\Lambda(\theta,t)$$
$$= \sum_{n=1,odd}^{+\infty} \sum_{l=-\infty}^{+\infty} \frac{F_{in}\Lambda_l}{2} \cos((np_{ro} + lp_{ri}) \tag{4-10}$$
$$=\cdot \left(\theta + \frac{np_{ro}\Omega_{ro}+lp_{ri}\Omega_{ri}}{np_{ro}+lp_{ri}} t\right) + \varphi)$$

where

$$l = \pm k, \Lambda_l = \Lambda_{-l} \tag{4-11}$$

The PPN of the modulation winding p_{wc} should match the PPN of the modulated harmonic that generates the largest back EMF for maximum steady torque transformation. In the proposed design, p_{wc} is selected as the component that is modulated by the third harmonic, because the flux density and the speed of the third harmonic component are both higher than that of the fundamental one [97, 117]. According to (4-10), the PPN, speed, and the frequency of the control winding can be expressed as

$$p_{wc} = |np_{ro} + lp_{ri}|_{n=3,l=-1} = |3p_{ro} - p_{ri}| \tag{4-12}$$

$$\Omega_{wc} = \left(\frac{np_{ro}}{np_{ro}+lp_{ri}}\Omega_{ro} + \frac{lp_{ri}}{np_{ro}+lp_{ri}}\Omega_{ri}\right)_{n=3,l=-1}$$
$$= \frac{3p_{ro}\Omega_{ro}-p_{ri}\Omega_{ri}}{3p_{ro}-p_{ri}} \tag{4-13}$$

$$f_{wc} = \frac{3p_{ro}\Omega_{ro}-p_{ri}\Omega_{ri}}{60} \tag{4-14}$$

4.3.3 PMSG part analysis

The spoke-type PMs enable the magnetic circuit to get through only the outer airgap, which has greatly decreased the magnetic reluctance [94]. The configuration of PMs on the outer rotor also has the flux-focusing effect, which increases the flux density in the airgap.

As the stator can be considered as a slotless iron core, its permeance only consists of the average component Λ_{st0}, and the airgap flux density of the PMSG part can be expressed as the following based on (4-5):

$$B_{PMSG}(\theta,t) = \sum_{m=1,odd}^{+\infty} F_{om}\Lambda_{st0}\cos(mp_{ro}(\theta + \Omega_{ro}t) + \varphi) \tag{4-15}$$

From (4-15) and (4-7), the largest component can be obtained when $m = 1$. For generating the largest back EMF, the PPN, speed, and the frequency of the power winding should satisfy

$$p_{wp} = (mp_{ro})_{m=1} = p_{ro} \tag{4-16}$$

$$\Omega_{wp} = \Omega_{ro} \tag{4-17}$$

$$f_{wp} = \frac{p_{ro}\Omega_{ro}}{60} \tag{4-18}$$

From (4-14) and (4-18), by controlling the frequency of the control winding, the outer rotor speed can remain constant despite variations in the inner rotor speed, and the frequency of power winding can remain constant, which achieved VSCF operation.

For shortening the end winding and reducing the cogging torque, the fractional-slot configuration with coil pitch of one slot is often used, where the following relationship of p_{ro} and the slot number of stator Z is often used:

$$p_{ro} = p_{wp} = \frac{Z}{2} \pm 1 \tag{4-19}$$

4.3.4 Torque/Power distribution

Based on the torque balance equation and the law of energy conservation, the torque and power relationship of the MGCM part can be given as

$$T_{wc} + T_{roc} + T_{ri} = 0 \tag{4-20}$$

$$T_{wc}\Omega_{wc} + T_{roc}\Omega_{ro} + T_{ri}\Omega_{ri} = P_{wc} + P_{roc} + P_{ri} = 0 \tag{4-21}$$

where T_{wc} and T_{roc} are the electromagnetic torque and the outer rotor torque produced by the control winding, P_{wc} and P_{roc} are the electromagnetic power and the outer rotor power produced by the control winding, T_{ri} and P_{ri} are the inner rotor torque and power. With (4-12), (4-13), (4-20), and (4-21), the following torque-pole pair relationship can be obtained:

$$T_{wc}:T_{roc}:T_{ri} = p_{wc}:(-3p_{ro}):p_{ri} \tag{4-22}$$

Similarly, the torque and power relationship of the PMSG part can be expressed as

$$T_{wp} + T_{rop} = 0 \tag{4-23}$$

$$T_{wp}\Omega_{ro} + T_{rop}\Omega_{ro} = P_{wp} + P_{rop} = 0 \tag{4-24}$$

where T_{wp} and T_{rop} are the electromagnetic torque and the outer rotor torque produced by the power winding, P_{wp} and P_{rop} are the electromagnetic power and the outer rotor power produced by the power winding.

4.3.5 BLDFM analysis

For VSCF operation, the overall torque of the outer rotor T_{ro} should be 0, which can be given as

$$T_{ro} = T_{rop} + T_{roc} = 0 \tag{4-25}$$

Take (4-25) into (4-21) and (4-24), the following power relationship can be concluded:

$$P_{wc} + P_{ri} + P_{wp} = 0 \tag{4-26}$$

Here, defining the synchronous speed of inner rotor Ω_{ri0} as the speed when the control winding's input is direct current (DC), i.e., $f_{wc} = 0$, which can be expressed as

$$\Omega_{ri0} = \frac{3p_{ro}\Omega_{ro}}{p_{ri}} \tag{4-27}$$

From (4-12) - (4-18), and (4-27), the slip of the inner rotor can be given as

$$s = \frac{\Omega_{ri0} - \Omega_{ri}}{\Omega_{ri0}} = \frac{1}{3}\frac{p_{wc}\Omega_{wc}}{p_{wp}\Omega_{wp}} = \frac{1}{3}\frac{f_{wc}}{f_{wp}} \tag{4-28}$$

Take (4-22) and (4-23) into (4-28), the power of the control and power winding have the relationship of

$$\frac{P_{wc}}{P_{wp}} = \frac{T_{wc}\Omega_{wc}}{T_{wp}\Omega_{ro}} = \frac{p_{wc}\Omega_{wc}}{-3p_{ro}\Omega_{wp}} = -s \tag{4-29}$$

The negative sign shows the direction of control and power winding power is different, i.e., one input and one output. The mechanical input and output power for the BLDFM system are

$$P_{in\_mech} = P_{ri} \tag{4-30}$$

$$P_{out} = P_{wp} \tag{4-31}$$

Take (4-29)-(4-31) into (4-26), the relationship of input and output power can be given as

$$P_{in\_mech} = -(1-s)P_{out} \tag{4-32}$$

This shows the presented BLDFM system agrees with the concept of conventional DFM.

From (4-29), (4-31), and (4-32), the relationship of power winding and input power is

$$P_{wc} = -\mathrm{s}P_{out} = \frac{s}{1-s}P_{in\_mech} \tag{4-33}$$

For conventional BLDD-DFM in [133] whose control winding choose to modulate with fundamental harmonic, the slip of the inner rotor is

$$s' = \frac{f_{wc}}{f_{wp}} = 3s \tag{4-34}$$

From (4-34), it can be observed that the slip of conventional design is three times of the proposed one. Therefore, take (4-34) into (4-33), the ratio of power consumption for the conventional power winding P'_{wc} and proposed power winding can be expressed as

$$\frac{P'_{wc}}{P_{wc}} = 3\,\frac{1-s}{1-3s} \tag{4-35}$$

For normal condition, the slip of both conventional and proposed designs should be in the range of [0,1], i.e.,

$$\begin{cases} s' \in [0,1] \\ s \in [0,1] \end{cases} \Rightarrow s \in [0,\tfrac{1}{3}] \tag{4-36}$$

Take (4-36) to (4-35), we can get

$$\frac{P'_{wc}}{P_{wc}} \in [3, +\infty] \tag{4-37}$$

From (4-37), it can be observed that when the input power remain the same, to achieve the same performance, the power consumption of the conventional design is at least 3 times greater than that of the proposed design, which is more energy efficient.

4.4 Performance Comparison and Analysis

Table 4-1. Main dimensions of the proposed design and conventional design

Item	Prop. BLDD-DFM	Conv. BLDD-DFM
Stator outer diameter	210 mm	
Stack length	50 mm	
Airgap length	1 mm	
Slot number (Z)	24	18
PPN of outer rotor spoke-PMs (p_{ro})	11	15
PPN of outer rotor radial-PMs	11	N/A
No. of inner rotor teeth (p_{ri})	31	13
PPN of control winding	2	2
PPN of power winding	11	3
PM volume	79.2 cm ^{3}	
Outer rotor speed	300 rpm	
Inner rotor speed	50 rpm	
Net slot area	125 mm^2	
Rated current density	6 A/mm^2	
Magnet material	N40UH	
Silicon steel sheet	35WW300	

In order to demonstrate the enhancements provided by the proposed BLDD-DFM, two models were developed: the proposed model and a conventional model based on the design presented in [133]. The electromagnetic performances of these two machines were compared using FEM analysis. To ensure a fair and meaningful comparison, the net slot area, PM volume, and overall machine volume are kept identical for both designs. The key dimensions of the two models are provided in Table 4-1. In the subsequent tables and figures, the short terms "prop." and "conv." correspond to the proposed and conventional designs, respectively.

4.4.1 No-load Comparison and Analysis

The flux line distributions are depicted in the upper section of Fig. 4-5. In Fig. 4-5(a) and Fig. 4-5(b), a 2-pole-pair modulated field is observed in the inner rotor. The flux lines in the stator exhibit a combination of a 2-pole-pair and an 11-pole-pair field in Fig. 4-5(a), and a combination of a 2-pole-pair and a 3-pole-pair field is displayed in Fig. 4-5(b).

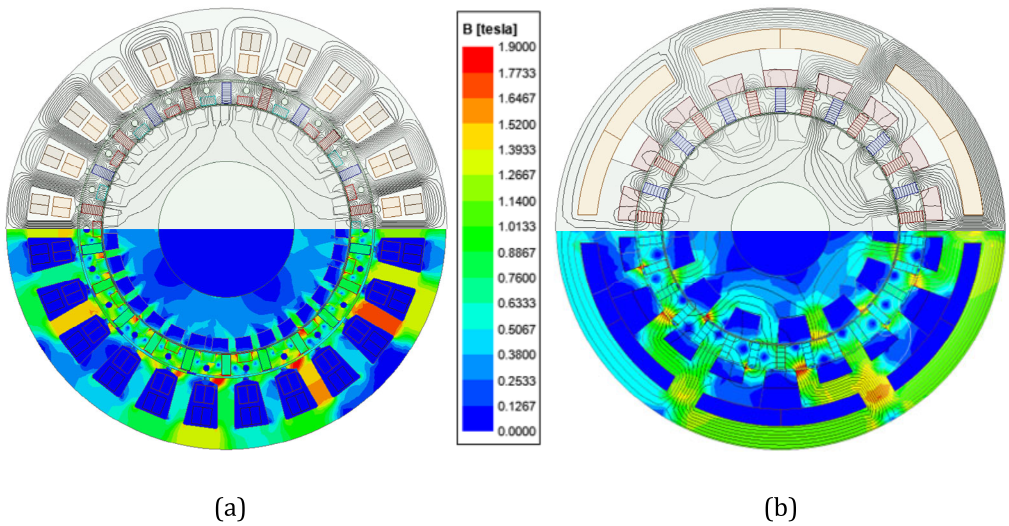

Fig. 4-5. Comparison of no-load flux line distribution and on-load flux density map. (a) Proposed design. (b) Conventional design.

Fig. 4-6 shows the airgap flux density waveforms and the harmonic distribution of the proposed and conventional designs in the outer airgap. The back EMF waveforms and their harmonic distributions of the proposed and conventional designs for the power and control windings are shown in Fig. 4-7 and Fig. 4-8, respectively.

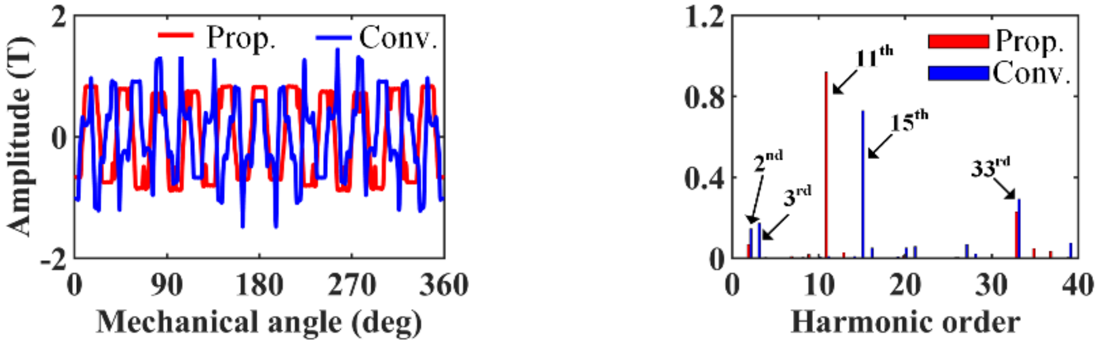

(a) (b)

Fig. 4-6. Comparison of the outer airgap flux density. (a) Waveform. (b) FFT spectrums.

Fig. 4-6 reveals that the dominant components that align with the control winding and power winding of the proposed design are the 2nd and 11th components, while the dominant components corresponding to the control winding and power winding of the conventional design are the 2nd and 3rd components. The 3rd component of flux density exhibits an amplitude of 0.17T. Although the 3rd component for the conventional design represents a flux modulated component with a higher frequency (five times the frequency of the proposed design due to the gear ratio of $G = \frac{p_{wp}}{p_{ro}} = 5$), its amplitude is comparatively lower. In contrast, the 11th component exhibits a significantly higher amplitude of 0.91T. In Fig. 4-7, the back EMF of the proposed design is 73% greater than that of the conventional design.

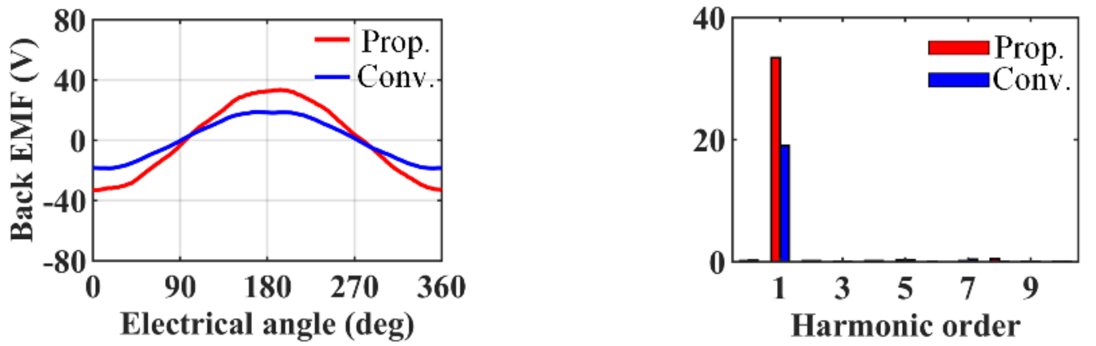

(a) (b)

Fig. 4-7. Comparison of power winding back EMF. (a) Waveform. (b) FFT spectrums.

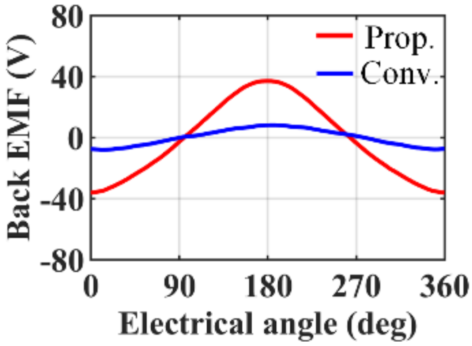

(a)

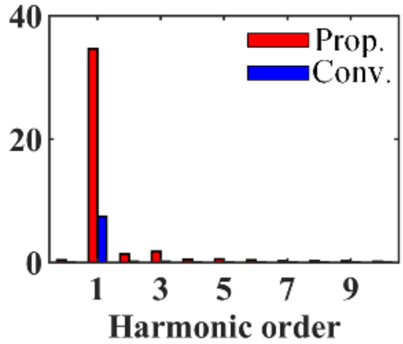

(b)

Fig. 4-8. Comparison of control winding back EMF. (a) Waveform. (b) FFT spectrums.

In the proposed design, the amplitude of the 2^{nd} component is 0.07T, which is lower than the conventional design's amplitude of 0.14T. However, it is important to note that the field rotation speed of the proposed design is three times higher compared to the conventional design. This is because the salient teeth modulation primarily affects the third-harmonic component. Additionally, the pole pair number of both the inner and outer rotor in the conventional design is considerably smaller than that of the proposed design. Consequently, the frequency of the control winding in the proposed design is significantly higher. Hence, the back EMF of the proposed design is approximately five times greater than that of the conventional design, as depicted in Fig. 4-8. This results also agrees with (4-37).

Although there is a relatively high 33^{rd} component for the proposed design, which is the third harmonic of the 11^{th} component, shown in Fig. 4-6, as the power winding is a three-phase Y-connected winding, all the $3k$-th components are eliminated. It will also not affect modulation winding due to winding factor filtering [97].

4.4.2 On-load Comparison and Analysis

The flux density map of the two designs is presented in the lower section of

Fig. 4-5. Both windings in both designs exhibit a current density of 6A/mm², which is suitable for air cooling. The maximum flux density observed in the stator teeth body and yoke of both designs remains below 1.7T, which is well below the knee point of the silicon steel sheet. It is worth noting that there are some localized areas of saturation on the tooth tips due to the trade-off between limited tip geometry size and larger slot area. However, the impact of these saturation areas on the main flux is relatively small and can be considered negligible, given their limited extent.

Fig. 4-9 to Fig. 4-12 display the torque density and the corresponding torque ripple of the outer and inner rotors for both the proposed and conventional designs under varying current in the power and control windings. In these figures, the current densities of the power and control windings are denoted as J_{wp} and J_{wc}, respectively. The torque density K_T and torque ripple T_{rip} are defined as

$$K_T = \frac{avg(T_r)}{V} \tag{4-38}$$

$$T_{rip} = \frac{pk2pk(T_r)}{avg(T_r)} \tag{4-39}$$

where $avg()$ is the function of calculation the average value, V is the electromagnetic part volume of the machine, and $pk2pk()$ is the function to compute the peak-to-peak value of the ripple.

Fig. 4-9 presents a comparison of the torque density for the outer rotor. In area 1, it is evident that the proposed design exhibits higher torque density than the conventional design under both rated and most operating conditions. The torque improvement variation reaches 23.03% under the rated condition, while the maximum variation reaches 122.59%. In area 2, the torque contribution from the MGCM portion is relatively small due to the low J_{wc} value. Consequently, the torque density of the proposed design is lower than that of the conventional design in this region. However, the maximum variation in area 2 is 21.69%, which is relatively smaller compared to the maximum variation observed in area 1.

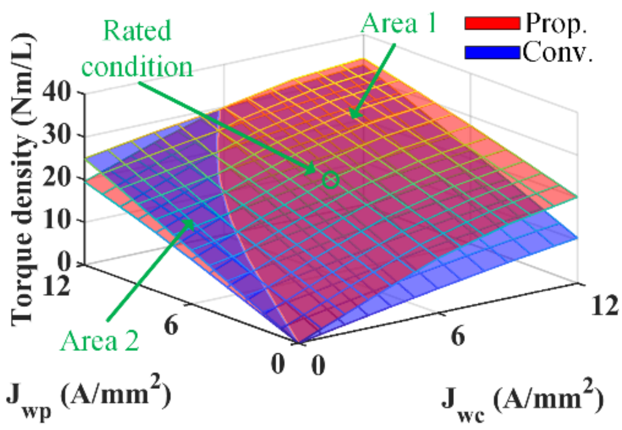

Fig. 4-9. Comparison of the outer rotor torque density.

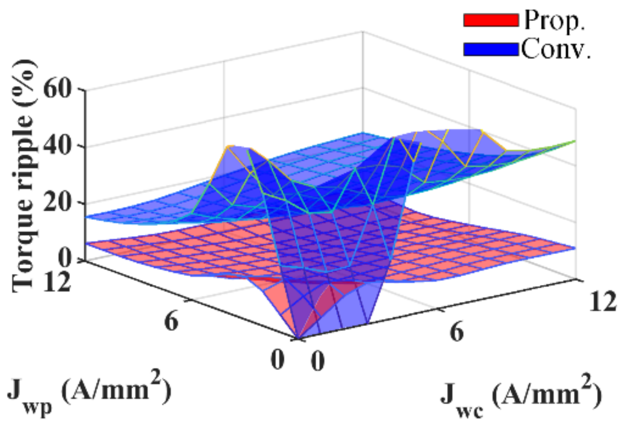

Fig. 4-10. Comparison of the outer rotor torque ripple.

Fig. 4-10 displays the torque ripple comparison for the outer rotor. In the proposed design, the mean torque ripple is 6.69%, with a value of 5.35% under the rated condition, and the maximum torque ripple reaches 15.15%. On the other hand, the conventional design exhibits a mean torque ripple of 28.89%, with a rated condition value of 23.83%, and a maximum torque ripple of 73.73%. The torque ripple of the proposed design is significantly lower than that of the conventional design, potentially attributed to factors such as the open-slot structure and the presence of abundant harmonics.

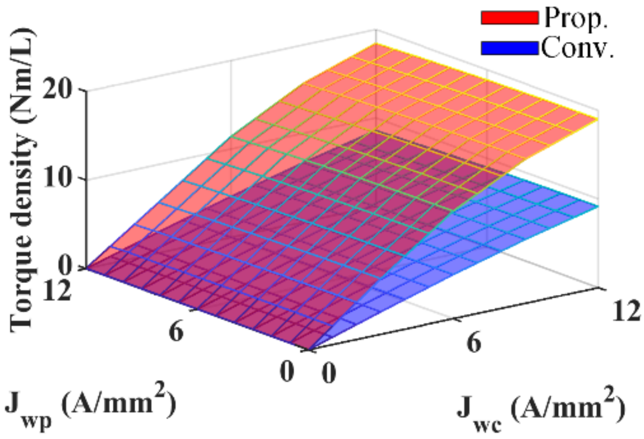

Fig. 4-11. Comparison of the inner rotor torque density.

From Fig. 4-11, it is evident that the torque density of the proposed design surpasses that of the conventional design across different J_{wc} values. It is important to note that J_{wp} solely affects the torque of the PMSG portion of the outer rotor and does not have any impact on the torque of the inner rotor. The torque improvement variation reaches 144.08% under the rated condition.

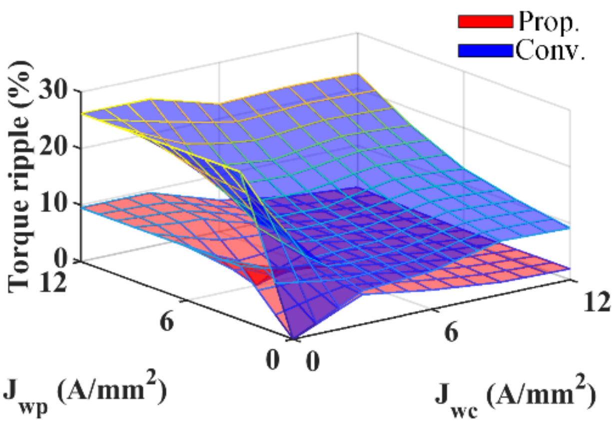

Fig. 4-12. Comparison of the inner rotor torque density.

Fig. 4-12 presents a comparison of the torque ripple for the inner rotor. In the proposed design, the mean torque ripple is 4.68%, with a maximum torque ripple of 9.53%. It is noteworthy that all torque ripple values of the proposed design remain below 10%. Conversely, the conventional design demonstrates a mean torque ripple of 15.46%, with a maximum torque ripple of 26.20%. The torque ripple of the proposed design is notably lower than that of the conventional design, even for the inner rotor.

4.5 Experiment Validation

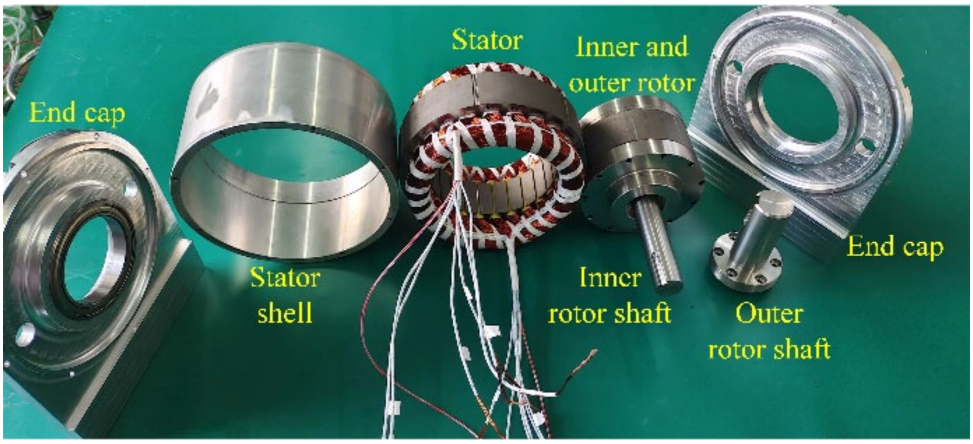

Fig. 4-13. The prototype assembly.

A prototype of the proposed BLDD-DFM is constructed to validate the feasibility, as depicted in Fig. 4-13. For VSCF operation, an experimental setup was prepared, as illustrated in Fig. 4-14. A servo motor was connected to the inner rotor to simulate the input from a wind turbine in this particular scenario. The outer rotor was suspended in the air, and its shaft was extended to enable position measurement. The power winding was linked to a three-phase resistance network with a resistance of 5Ω, serving as the load. The control winding was connected to an inverter, controlled by a dSPACE controller that adjusted the speed of the inner rotor. Fig. 4-15 presents the control diagram, which employed conventional field-oriented control. The reference speed of the control winding is dynamically calculated based on (4-13).

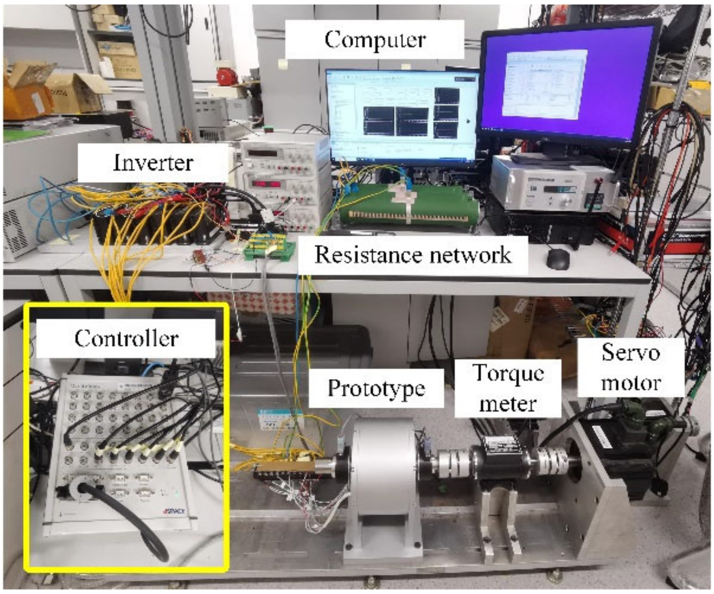

Fig. 4-14. Schematic of experiment setup.

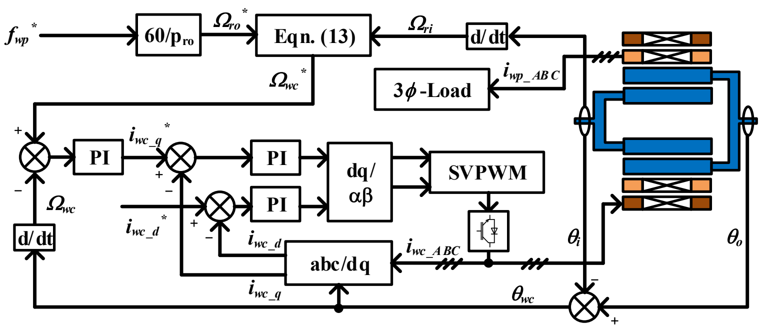

Fig. 4-15. Control diagram of the proposed BLDD-DFM.

Fig. 4-16 illustrates the noload back electromotive force (EMF) waveforms at an outer rotor speed of 300rpm and an inner rotor speed of 50rpm. Specifically, Fig. 4-16(a) and Fig. 4-16(b) present a comparison between the measured waveform (labelled "Exp.") and the finite element method (FEM) waveform for the control winding and power winding, respectively. The measured results obtained from the experiments are denoted as "Exp." in Fig. 4-16. The comparison demonstrates a good agreement between the experimental and FEM waveforms. The amplitude deviation is found to be 4.47% for the control winding and 1.83% for the power winding.

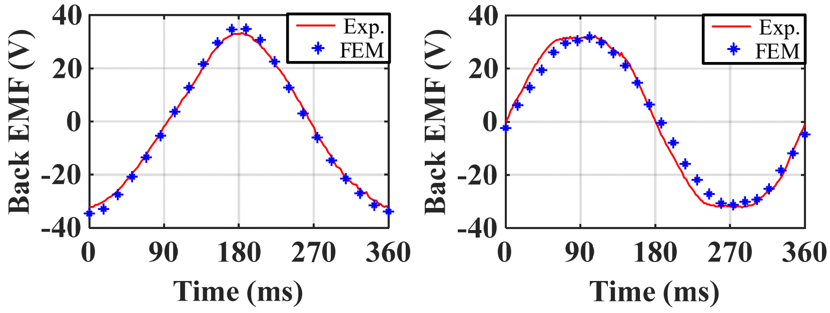

(a) (b)

Fig. 4-16. No-load back EMF waveforms. (a) Control winding. (b) Power winding.

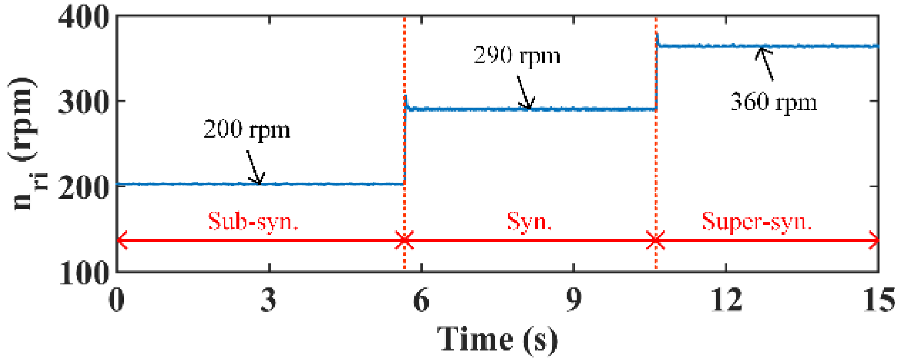

(a)

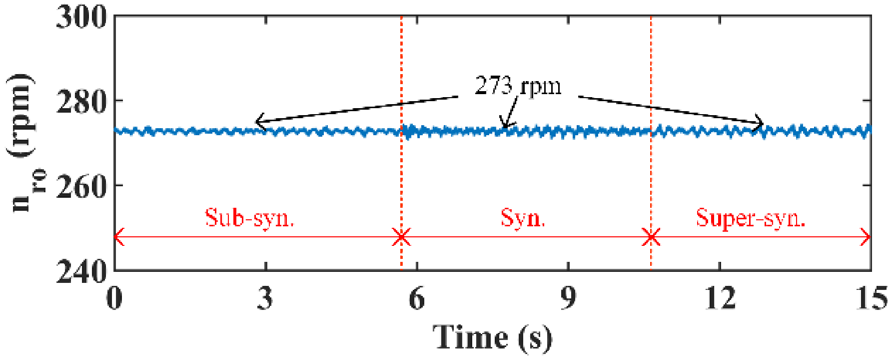

(b)

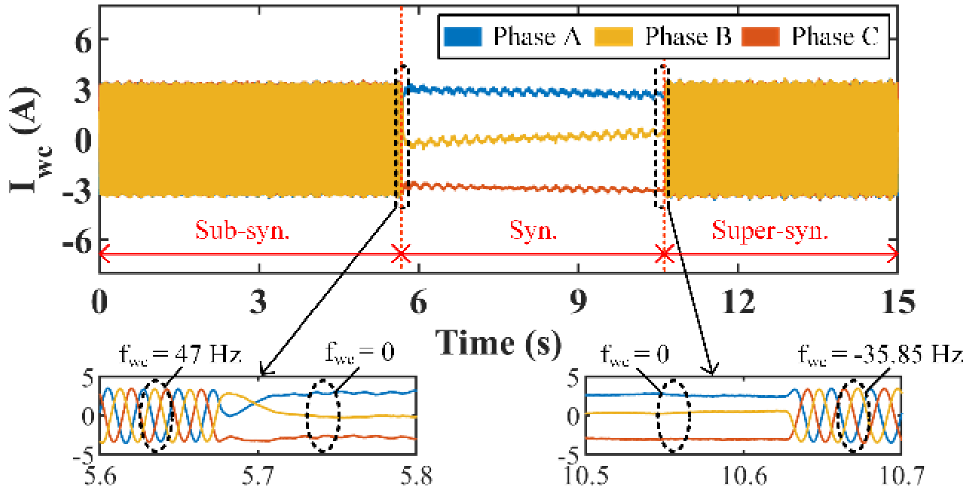

(c)

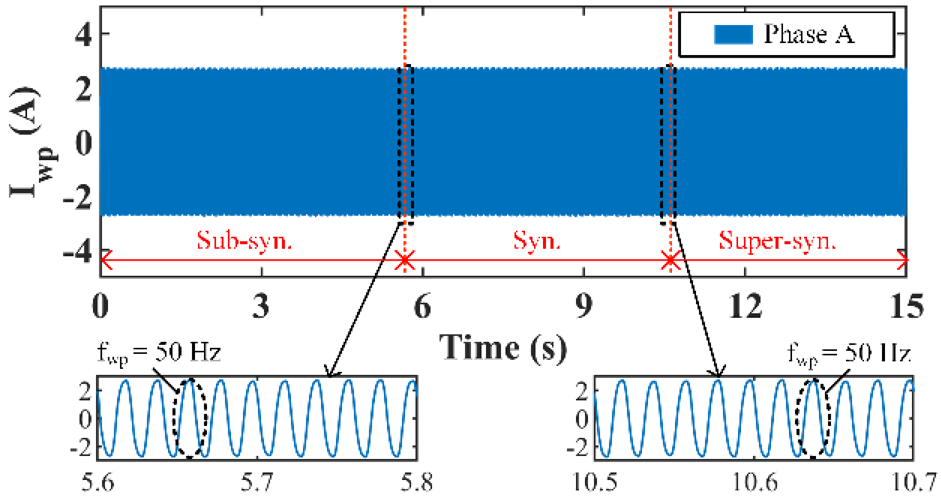

(d)

Fig. 4-17. The static VSCF experiment results. (a) Speed of inner rotor. (b) Speed of outer rotor. (c) Current of control winding. (d) Current of power winding.

The static VSCF experiment results are shown in Fig. 4-18, where “sub-syn.”, “syn.”, and “super-syn.” refers to the sub-synchronous mode, synchronous mode, and super-synchronous mode. According to (4-17), (4-18) and (4-27), the synchronous speed of the inner rotor can be calculated as 290rpm when the constant output frequency is set as 50Hz. When the inner rotor rotates at the speed of 200rpm, shown in Fig. 4-17(a), the control winding operates in sub-synchronous mode. The frequency of the winding is 47Hz with the positive sequence, i.e., Phase B leading Phase C by 120 electrical degrees, shown in the left subfigure of Fig. 4-17(c). When the inner rotor rotates at the synchronous speed, the frequency of the control winding changed to almost 0, shown in the middle part of Fig. 4-17(c). The control winding enters the super-synchronous mode when the inner rotor rotates at 360rpm. The frequency at this mode is -35.85Hz, where the negative sign refers to the negative sequence, shown in the right subfigure of Fig. 4-17(c). At this state, Phase B is lagging Phase C by 120 electrical degrees. By changing the frequency of the control winding, the speed of outer rotor and the frequency of power winding remain constant regardless the changing input rotor speed, shown in Fig. 4-17(b) and Fig. 4-17(d), respectively.

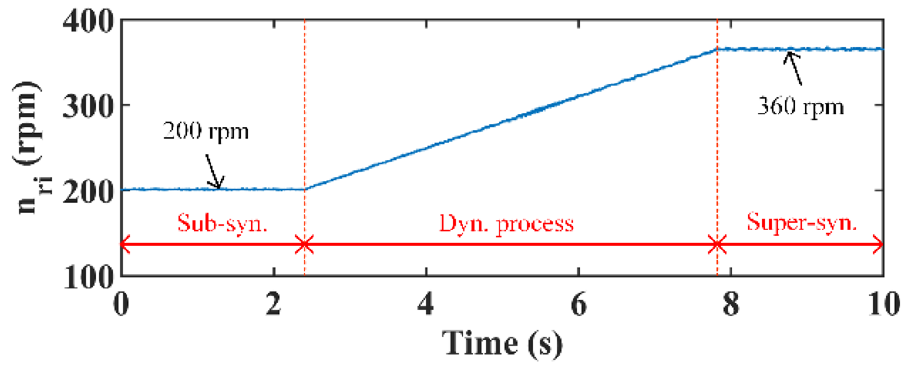

(a)

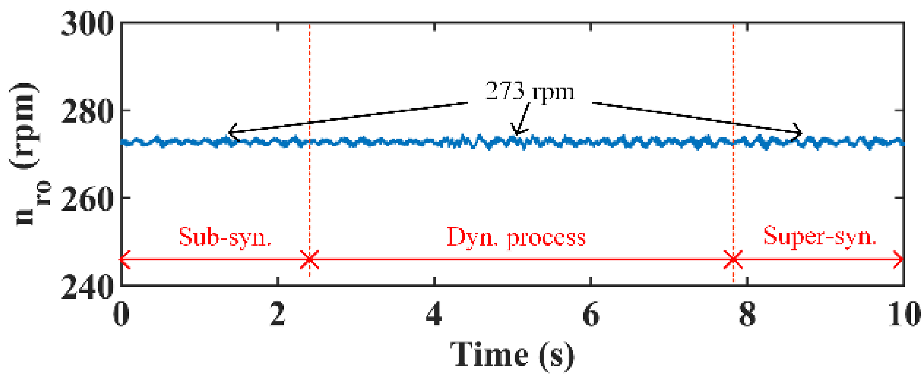

(b)

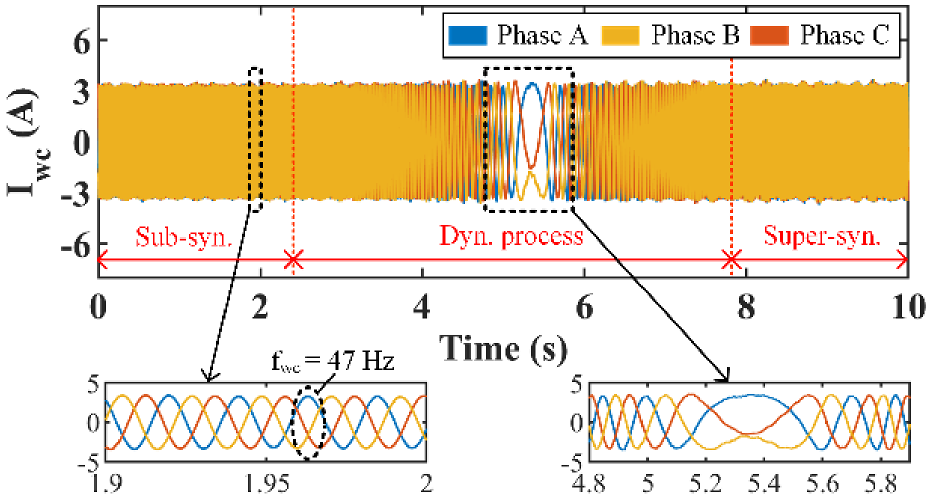

(c)

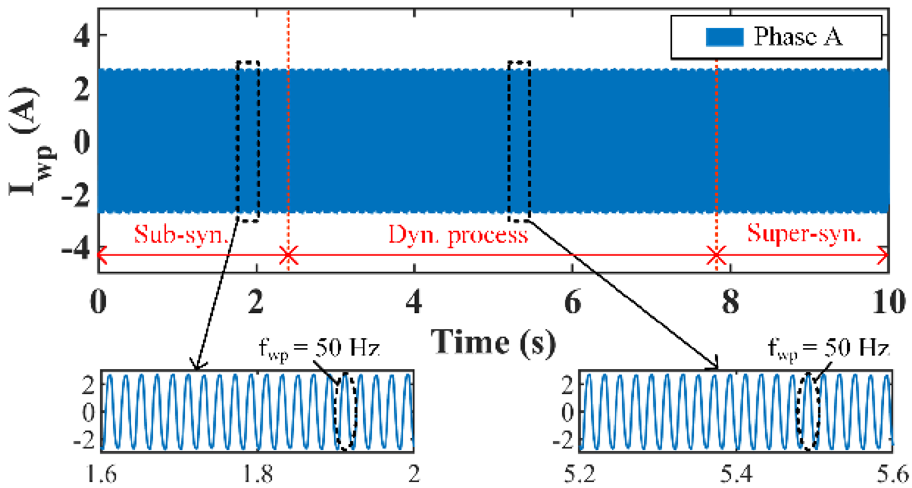

(d)

Fig. 4-18. The dynamic VSCF experiment results. (a) Speed of inner rotor. (b) Speed of outer rotor. (c) Current of control winding. (d) Current of power winding.

The dynamic VSCF experiment results are shown in Fig. 4-18, where "Dyn. process" refers to dynamic process. From Fig. 4-18(a), the inner rotor speed increases linearly from sub-synchronous mode to super-synchronous mode. Accordingly, the frequency of the control winding is changing continuously during the dynamic process, and the current sequence can be clearly observed to be altered at 5.38s, shown in the right subfigure of Fig. 4-18(c). The inner rotor speed and the frequency of power winding also remain constant under the dynamic process, shown in Fig. 4-18(b) and Fig. 4-18(d), respectively.

4.6 Summary

This paper presents a novel BLDD-DFM structure that employs high-order harmonic modulation to enhance torque density in the MGCM portion and minimize energy consumption in the control winding. The proposed design primarily focuses on artificially amplifying the third-harmonic component of the airgap flux density. Through the utilization of high-order modulation, the slip ratio of the proposed design substantially decreases, leading to a threefold reduction in energy consumption in the control winding compared to conventional designs. FEM simulations are conducted to compare the prototype with a conventional design having certain same dimensions. The results illustrate that the back EMF in the control winding of the proposed design is five times greater than that of the conventional design and 73% higher than the power winding in the conventional design. Under rated conditions, the torque improvement variation reaches a maximum of 23.03% for the outer rotor torque and 144.08% for the inner rotor torque in the proposed design compared to the conventional design. Furthermore, the torque ripple of both the outer and inner rotors in the proposed design is approximately half of the conventional design. A prototype is manufactured and tested, with the experimental results aligning with the working principles and FEM simulations. VSCF experiments are conducted in static and dynamic conditions, verifying its feasibility.

Chapter 5 Novel Mechanical Flux-weakening Design of a Spoke-type Permanent Magnet Generator for Stand-alone Power Supply

5.1 Introduction

Currently, more than 1.1 billion people are not accessible to the electrical grid. Most of these people live in rural areas or offshore islands, and expanding the power grid to these remote areas is neither economical nor effective [134]. A stand-alone wind energy generating system is a perspective method of providing electricity to regional grids and effectively solving the above-mentioned issues. Among all wind generators, the permanent magnet (PM) generator, with its high torque density and efficiency, is the most favored electrical generator. However, as the wind speed is not constant, the output voltage would remain constant if no control is introduced. For conventional PM generator, a fully rated matrix converter may be needed, which may be expensive and complex to control. To effectively control the output voltage, flux-weakening control is widely used for PM machines. Numerous methods of flux weakening have been proposed in the past 20 years, which can mainly be classified into two categories: Electrical and mechanical techniques.

For electrical flux-weakening techniques, the most conventional method is to inject a negative d-axis current, which produces a field that opposes the original PM field. This technique is relatively suitable for machines with a high saliency ratio, i.e., the difference between the d-axis and q-axis inductance is significant

[135-137]. However, additional external inductors are required for a machine with a small saliency ratio if the negative d-axis current injection flux-weakening technique is used [138], which adds more complexity to the system. In addition, over-injection of negative d-axis current may cause the demagnetization of the PMs. Moreover, for the generating system, using this method requires two sets of windings, and the coupling effect between two windings needs further consideration. Another electrical flux-weakening technique uses the variable flux method, which can be further categorized into hybrid excitation type and mnemonic material type. Hybrid excitation type machines generally need an extra set of DC excitation winding, which could enhance or weaken the field by injecting positive or negative DC. Typically, the DC excitation flux path is parallel to the PMs to prevent demagnetization of the PMs [139-142]. Nevertheless, two sets of windings are needed for this type of machine. The mnemonic material type machine, also known as a memory machine, uses the Alnico PM for parts or all excitations of the machine. The Alnico PM has low coercivity; therefore, its magnetization direction can be easily adjusted using excitation pulses in the d-axis direction of Alnico PMs [143, 144]. Nevertheless, the structure of the memory machine needs to be specially designed to prevent the interaction between the field generated by the armature and Alnico PMs, which is relatively complex. Otherwise, the unwanted demagnetization of Alnico PMs may occur.

With the electrical methods, considerable amounts of current would have to be consumed to weaken the strong flux from the PMs or maintain the excitation flux, which results in an efficiency decrease, while also having the risk of PM demagnetization. Conversely, mechanical methods adjust the linked flux by manipulating the position of certain machine parts, which avoids the current consumption. Therefore, mechanical methods might be more suitable for the application of a stand-alone generator, where a wide speed range and constant working condition is required. Mechanical flux-weakening techniques can be categorized into two categories: Self-actuated type and actively controlled type [145]. The self-actuated type generally uses the rotating speed-related force and the spring system to realize the movement of flux-adjusting elements by themselves. In [146], a spoke IPM machine with movable ferromagnetic yokes connected with the spring system is proposed. The yoke provides a leakage path that can move closer to the inner rotor rim when the centrifugal force is large, thus achieving flux regulation by itself. In [147], a double-rotor PM machine is proposed in which one rotor is directly connected to the shaft, and another rotor rotates with displacement relative to the shaft by the spring system. Depending on the rotational speed, two rotors will have a corresponding displacement angle. Therefore, the total flux linkage, which is the vector sum of two flux linkages, is adjustable. However, all the self-actuated mechanical flux-weakening methods cannot be controlled manually, which may be problematic when emergencies occur. Moreover, the spring system is difficult to calibrate and requires regular maintenance. The actively controlled mechanical flux-weakening method uses an external force to control the flux-adjusting elements. A switched flux machine with movable iron pieces outside of the stator that is controlled independently is introduced in [148]. When the iron piece is moved to the closed position, the PM flux is short-circuited, reducing 60% of the flux linkage compared to the conventional switched flux machine. An actively controlled version of the axial-flux PM machine in [149] is proposed and a radial-flux version is presented in

[150], which has the minimum flux linkage in the equilibrium position and the maximum flux linkage in the aligned position.

In [151], a dual-rotor PM machine based on bidirectional flux modulation is proposed for the standalone DC power supply. This design requires a conventional winding whose pole pair number is equal to the outer rotor, and a modulation winding. Two sets of windings are connected in series as their frequencies are the same. The inner rotor is connected to the servo motor. Therefore, the inner PM flux linkage vector is adjustable and the sum of modulated vector and the outer PM vector, namely the total flux linkage, is controllable. This active-controlled mechanical flux-weakening method suits the machine with a small saliency ratio. Nevertheless, two sets of windings are needed, which have the following shortcomings: First, two pairs of windings have different coil pitches, which are relatively complex to manufacture; second, the turn numbers of two pairs of windings are different for reaching the maximized flux controlling range.

This paper proposes a novel mechanical flux-weakening spoke-type PM generator. In only one set of windings, all three working harmonics have the same frequency, which can be added as vectors based on the flux modulation principle. By adjusting the modulator ring within a certain angle, the flux can be effectively controlled without the risk of PM demagnetization, and the variable-speed constant-amplitude voltage control (VSCAVC) can be achieved. A commercial servo system using the position control mode is sufficient for dynamic performance, which is also cost-efficient, robust, and easy to control. The principles of flux controlling and working harmonic selection are introduced. To investigate the influence of the pole pair number and the performance of the novel design, four cases with different rotor poles and winding configurations, i.e., 12/7, 12/8, 12/10, and 12/11 stator/rotor pole pair combinations, have been designed, optimized, and compared. Finally, the 12/7 design is selected, and its VSCAVC characteristics are analyzed.

5.2 Machine Configuration and Operating Principle

5.2.1 Machine Configuration

The configuration of the proposed generating system is shown in Fig. 5-1. The designed model consists of a stator, an adjustable modulator ring, and a rotor. A three-phase seven-pole-pair winding is placed inside twelve stator slots. A set of seven-pole-pair PMs is placed on the rotor. The PMs on the rotor are tangentially magnetized for flux concentration. The rotor is connected to the wind turbine through a gearbox. A twelve-pole-pair adjustable modulator ring is placed between the stator and rotor. The modulator is connected to the servo motor, which can be adjusted within a limited angle for flux weakening.

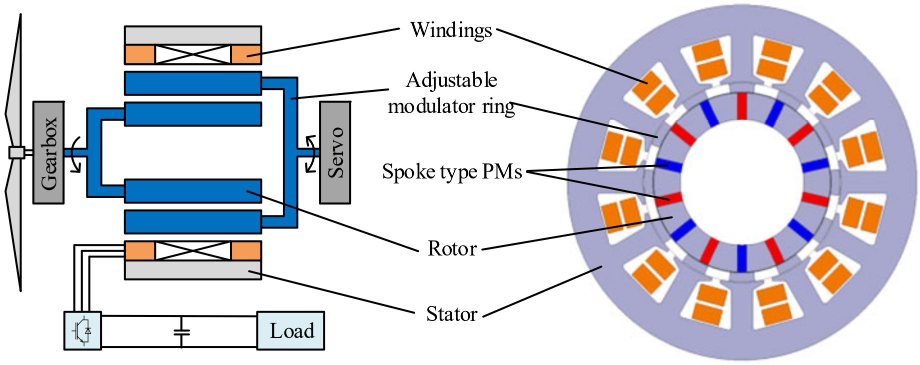

Fig. 5-1. Configuration of the mechanical flux-weakening design of the PM generating system.

5.2.2 Flux Modulation Principles

The parameter definition of the analytical model is shown in Fig. 5-2.

Suppose that the number of stator slots, the number of pole pair of the rotor, and the number of pole pair of modulators are Z, p_r, and p_m.

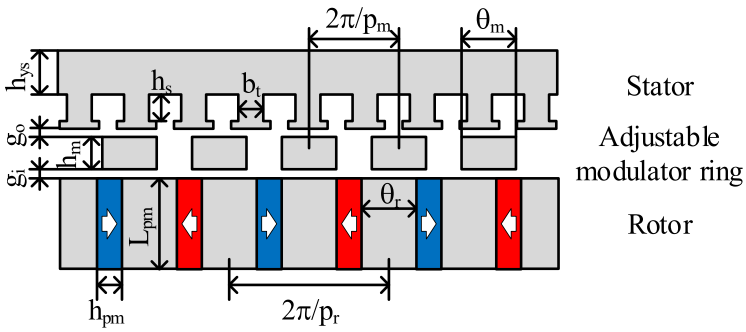

Fig. 5-2. Parameter definition of the analytical model.

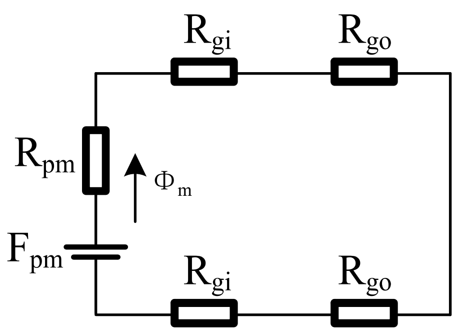

Fig. 5-3. Magnetic circuit of one pole.

When neglecting the magnetic resistance of the iron core, the slotting effect of the stator core, and the flux leakage, the magnetic circuit of one pole can be given in Fig. 5-3 [118]. The magnetomotive force (MMF) of one piece of PM can be expressed as follows:

$$F_{pm} = H_c h_{pm} \tag{5-1}$$

where H_c is the coercivity of the PM, and h_{pm} is the thickness of the PM, as shown in Fig. 5-2. The resistance of the PM airgap of one pole and the outer airgap of one pole can be given as follows:

$$R_{pm} = \frac{h_{pm}}{\mu_0 \mu_{pm} L_{pm} l_{stk}} \tag{5-2}$$

$$R_{gi} = \frac{2g_i}{\mu_0 \theta_r r_g l_{stk}} \tag{5-3}$$

$$R_{go} = \frac{2g_o}{\mu_0 \theta_r r_g l_{stk}} \tag{5-4}$$

where μ_0 is the magnetic permeability of the vacuum, μ_{pm} is the relative magnetic permeability of the PM material, g_o and g_i denote the length of the inner and outer airgap, θ_r is the thickness of the iron core of one pole, r_g is the radius of the airgap, and l_{stk} is the stack length. The flux of one pole can be calculated as follows:

$$\Phi_m = \frac{F_{pm}}{R_{pm}+2R_{gi}+2R_{go}} \tag{5-5}$$

The amplitude of one pole's MMF in the airgap can be expressed as follows:

$$F_m = 2\Phi_m\left(R_{gi} + R_{go}\right) \tag{5-6}$$

The waveform of the rotor in the airgap is shown in Fig. 5-4, which can be expressed as follows:

$$F_r(\theta, t) = \sum_{i=1,3,5\ldots} F_{ri}\cos\left(ip_r(\theta + \Omega t)\right) \tag{5-7}$$

where F_{ri} is the magnitude of the i-th rotor PM MMF component, which can be further derived as follows:

$$F_{ri} = \frac{4F_m}{i\pi}\sin\frac{ip_r\theta_r}{2} \tag{5-8}$$

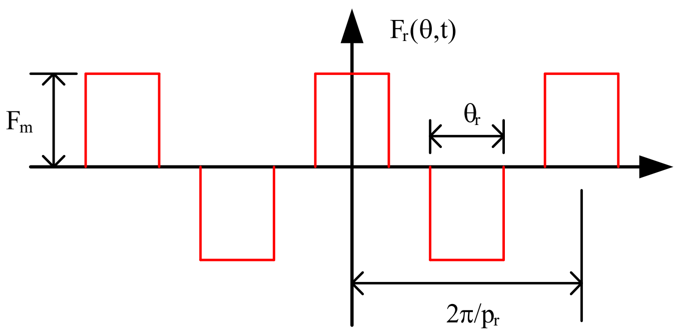

Fig. 5-4. MMF waveform of the rotor PMs.

The permeance of the modulator is presented in Fig. 5-5, which can be expressed as follows:

$$\Lambda(\theta, \phi) = \Lambda_0 + \sum_{j=1,2,3\ldots} \Lambda_j\cos\left(jp_m(\theta + \phi)\right) \tag{5-9}$$

where ϕ is the mechanical initial phase angle of the modulator, Λ_0 is the magnitude of the modulators' average permeance component, and Λ_j is the magnitude of the j-th permeance component, which can be expressed as follows:

$$\Lambda_j = \frac{2\Lambda_m}{j\pi}\sin\frac{jp_m\theta_m}{2} \tag{5-10}$$

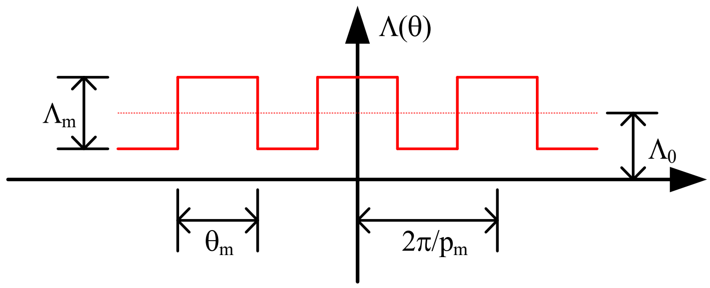

Fig. 5-5. Permeance waveform of the modulator.

The airgap flux density produced by the rotor PMs and the modulator teeth can be deduced by multiplying (5-7) and (5-9) and is expressed as follows:

$$B_r(\theta,t,\phi) = F_r(\theta,t)\Lambda(\theta,\phi) = B_{r1}(\theta,t) + \left(B_{r2}(\theta,t,\phi) + B_{r3}(\theta,t,\phi)\right) \tag{5-11}$$

where

$$B_{r1}(\theta,t) = \sum_{i=1,3,5\ldots} F_{ri}\Lambda_0\cos\left(ip_r(\theta+\Omega t)\right) \tag{5-12}$$

$$B_{r2}(\theta,t,\phi) = \sum_{i=1,3,5\ldots}\sum_{j=1,2,3\ldots}\frac{F_{ri}\Lambda_j}{2}\cos\left((jp_m+ip_r)\left(\theta+\frac{ip_r\Omega}{jp_m+ip_r}t\right)+jp_m\phi\right) \tag{5-13}$$

$$B_{r3}(\theta,t,\phi) = \sum_{i=1,3,5\ldots}\sum_{j=1,2,3\ldots}\frac{F_{ri}\Lambda_j}{2}\cos\left((jp_m-ip_r)\left(\theta-\frac{ip_r\Omega}{jp_m-ip_r}t\right)+jp_m\phi\right) \tag{5-14}$$

For convenience in further analysis, the coefficients of the components from (3-12) to (3-14) are sorted and listed in Table 5-1. Harmonic components can be categorized into the following three types:

- Type A components are unmodulated stationary components.
- Type B1 components are modulated components that rotate in the same direction as type A and can be adjusted mechanically.
- Type B2 components are modulated components that rotate in the opposite

direction from type A and can be adjusted mechanically.

Table 5-1. Coefficients of the PM harmonic components in the airgap.

Type	Components	Order	Speed	Frequency	Elec. Initial Phase Angle
A	B_{r1}	ip_r	Ω	$ip_r\Omega$	0
B1	B_{r2}	$ip_r + jp_m$	$\frac{ip_r\Omega}{jp_m + ip_r}$	$ip_r\Omega$	$jp_m\phi$
B2	B_{r3}	$\lvert ip_r - jp_m\rvert$	$-\frac{ip_r\Omega}{\lvert ip_r - jp_m\rvert}$	$ip_r\Omega$	$jp_m\phi$

The flux linkage of one phase can be calculated as follows:

$$\psi_{ph}(t,\phi) = r_g l_{stk} N_t k_d \int_{-\frac{\pi}{Z}y_{ph}}^{\frac{\pi}{Z}y_{ph}} B_r(\theta,t,\phi)d\theta = \psi_{phA}(t) + \psi_{phB1}(t,\phi) + \psi_{phB2}(t,\phi) \quad \text{(5-15)}$$

where N_t is the number of turns in one phase, k_d is the corresponding distribution factor, and y_{ph} is the corresponding coil pitch. By substituting (5-12)–(5-14) into (5-15), the ψ_{ph} components of the three types can be expressed as follows:

$$\begin{aligned}\psi_{phA}(t) &= r_g l_{stk} N_t k_{dA} \int_{-\frac{\pi}{Z}y_A}^{\frac{\pi}{Z}y_A} B_{r1}(\theta,t)d\theta \\ &= \sum_{i=1,3,5\ldots} \frac{2r_g l_{stk} N_t k_{dA} F_{ri}\Lambda_0}{ip_r} \sin\left(ip_r \frac{y_A\pi}{Z}\right)\cos(ip_r\Omega t)\end{aligned} \quad \text{(5-16)}$$

$$\begin{aligned}\psi_{phB1}(t,\phi) &= r_g l_{stk} N_t k_{dB1} \int_{-\frac{\pi}{Z}y_{B1}}^{\frac{\pi}{Z}y_{B1}} B_{r2}(\theta,t,\phi)d\theta \\ &= \sum_{i=1,3,5\ldots}\sum_{j=1,2,3\ldots} \frac{r_g l_{stk} N_t k_{dB1} F_{ri}\Lambda_j}{(jp_m+ip_r)} \sin\left((jp_m + ip_r)\frac{y_{B1}\pi}{Z}\right)\cos(ip_r\Omega t + jp_m\phi)\end{aligned} \quad \text{(5-17)}$$

$$\begin{aligned}\psi_{phB2}(t,\phi) &= r_g l_{stk} N_t k_{dB2} \int_{-\frac{\pi}{Z}y_{B2}}^{\frac{\pi}{Z}y_{B2}} B_{r3}(\theta,t,\phi)d\theta \\ &= \sum_{i=1,3,5\ldots}\sum_{j=1,2,3\ldots} \frac{r_g l_{stk} N_t k_{dB2} F_{ri}\Lambda_j}{(jp_m-ip_r)} \sin\left((jp_m - ip_r)\frac{y_{B2}\pi}{Z}\right)\cos(-ip_r\Omega t + jp_m\phi)\end{aligned} \quad \text{(5-18)}$$

The back EMF of one phase can be calculated as follows:

$$E_{ph}(t,\phi) = -\frac{d\psi_{ph}(t,\phi)}{dt} = E_{phA}(t) + E_{phB1}(t,\phi) + E_{phB2}(t,\phi) \quad \text{(5-19)}$$

By substituting (5-16)–(5-18) into (5-19), the E_{ph} components of three types can be expressed as follows:

$$E_{phA}(t) = \sum_{i=1,3,5\ldots} E_{mA(i)}\sin(ip_r\Omega t) \quad \text{(5-20)}$$

$$E_{phB1}(t,\phi) = \sum_{i=1,3,5\ldots}\sum_{j=1,2,3\ldots} E_{mB1(i,j)}\sin(ip_r\Omega t + jp_m\phi) \quad \text{(5-21)}$$

$$E_{phB2}(t,\phi) = \sum_{i=1,3,5\ldots}\sum_{j=1,2,3\ldots} E_{mB2(i,j)}\sin(ip_r\Omega t - jp_m\phi) \quad \text{(5-22)}$$

where $E_{mA(3-i)}$, $E_{mB1(3-i,j)}$, and $E_{mB2(3-i,j)}$ are the amplitudes of E_{ph_A}, $E_{ph_{B1}}$, and $E_{ph_{B2}}$, respectively. All E_m can be given as the following expression:

$$E_m = k_w r_g l_{stk} N_t \omega B_m = k_d k_p r_g l_{stk} N_t \omega B_m \tag{5-23}$$

where k_w is the winding factor, k_p is the pitch factor, ω is the corresponding angular speed, and B_m is the corresponding amplitude of the flux density. Therefore, $E_{mA(3-i)}$, $E_{mB1(3-i,j)}$, and $E_{mB2(3-i,j)}$ can be expressed as follows:

$$E_{mA(i)} = k_{dA} k_{pA} r_g l_{stk} N_t \omega_A B_{mA} = k_{dA} \sin\left(ip_r \frac{y_A \pi}{Z}\right) \; r_g l_{stk} N_t \Omega (2F_{ri} \Lambda_0) \tag{5-24}$$

$$\begin{aligned} E_{mB1(i,j)} &= k_{dB1} k_{pB1} r_g l_{stk} N_t \omega_{B1} B_{mB1} \\ &= k_{dB1} \sin\left((jp_m + ip_r) \frac{y_{B1} \pi}{Z}\right) \; r_g l_{stk} N_t \frac{ip_r \Omega}{jp_m + ip_r} \left(F_{ri} \Lambda_j\right) \end{aligned} \tag{5-25}$$

$$\begin{aligned} E_{mB2(i,j)} &= k_{dB2} k_{pB2} r_g l_{stk} N_t \omega_{B2} B_{mB2} \\ &= k_{dB2} \sin\left((jp_m - ip_r) \frac{y_{B2} \pi}{Z}\right) \; r_g l_{stk} N_t \frac{ip_r \Omega}{jp_m - ip_r} \left(F_{ri} \Lambda_j\right) \end{aligned} \tag{5-26}$$

5.2.3 Working Harmonic Selection

The amplitude of the harmonics in type B is lower than type A with the same i under the flux modulation effect. Therefore, to obtain higher back electromotive force (EMF) and associated electromagnetic torque, the number of the pair of winding poles should be designed according to the harmonic order of type A. According to (3-8), the highest value of F_{ri} can be obtained when $i = 1$. Therefore, the pair number of the winding should be designed as follows:

$$p_a = p_r \tag{5-27}$$

Under the abovementioned winding design, all the harmonics in types A and B with $i = 1$ are utilized as working harmonics. As all three types of working harmonics have the same frequency, the back EMF of the three types of harmonics can be added together.

According to (5-10), the highest value of Λ_j can be obtained when $j = 1$. Therefore, the harmonics with $j = 1$ in type B are used as the main working harmonics.

The slot angles of types A, B1, and B2 harmonics can be calculated as follows:

$$\alpha_A = \frac{2\pi p_r}{Z} \tag{5-28}$$

$$\alpha_{B1} = \frac{2\pi(p_r+p_m)}{Z} \tag{5-29}$$

$$\alpha_{B2} = \frac{2\pi|p_r-p_m|}{Z} \tag{5-30}$$

To fully utilize all three types of working harmonics, the number of the modulation segments should be as follows:

$$p_m = Z \tag{5-31}$$

Under (5-31), the slot angle of type B harmonic components are as follows:

$$\alpha_{B1} = \frac{2\pi(p_r+p_m)}{Z} = \frac{2\pi p_r}{Z} + 2\pi = \alpha_A \tag{5-32}$$

$$\alpha_{B2} = \frac{2\pi|p_r-p_m|}{Z} = 2\pi - \frac{2\pi p_r}{Z} = 2\pi - \alpha_A \tag{5-33}$$

From (5-28), (5-32), and (5-33), the following can be observed:

- First, α_A is equal to α_{B1}, which indicates that types A and B1 have the same winding arrangement sequence.
- The sum of α_A and α_{B2} is 2π, which indicates that the winding arrangement sequence for the flux density components of type B2 is identical to those of types A and B1, but in the reverse direction.

Since the back EMF frequency of type A, B1, and B2 is the same, all three types of harmonics can generate the back EMF in the same winding set.

Taking the proposed machine in Fig. 5-1 as an example, $\alpha_A = \alpha_{B1} = 210°$, $\alpha_{B2} = 150°$. Their armature back EMF vectors with the rotating directions are shown in Fig. 5-6. In Fig. 5-6(b), we can observe that the back EMF vector sequence and the rotating direction of type B2 are different from types A and B1, which can eventually become the same winding arrangement as types A and B1 by vertical flipping. As the frequency of three types of working harmonics is the same, all three types can produce a back EMF in the same set of winding. We can conclude the following:

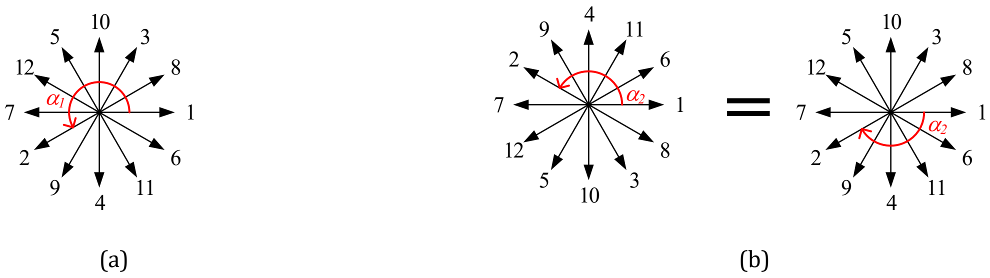

Fig. 5-6. Armature back EMF vectors of the proposed machine with the rotating direction. (a) $\alpha_A = \alpha_{B1} = 210°$; (b) $\alpha_{B2} = 150°$.

All three types of working harmonics have the same distribution factor and pitch factor, i.e.,

$$\begin{cases} k_{dA} = k_{dB1} = k_{dB2} = k_d \\ k_{pA} = k_{pB1} = k_{pB2} = k_p \end{cases} \tag{5-34}$$

The coil pitch of types A and B1 is opposite from type B2, i.e.,

$$\begin{cases} y_A = y_{B1} = y \\ y_{B2} = -y \end{cases} \tag{5-35}$$

5.2.4 Flux Controlling Principle

Total back EMF can be derived as the vector sum of the back EMF of types A, B1, and B2. From (5-24)–(5-26), we can conclude the vector graph of the back EMF, as shown in Fig. 5-7(a). Vector $\mathbf{E_A}$ is fixed, whereas $\mathbf{E_{B1}}$ and $\mathbf{E_{B2}}$ can rotate in the opposite direction. The total back EMF can change along the blue oval-shaped trajectory. When the electrical initial phase angle of the modulator $p_m\phi = 0°$, the components of types A, B1, and B2 have the same direction and the total back EMF reaches the maximum at this position, as shown in Fig. 5-7(b). When $p_m\phi = 180°$, both types B1 and B2 have the opposite direction from type A, and the total back EMF reaches the minimum at this position, as shown in Fig. 5-7(c). Therefore, although types B1 and B2 have different rotation directions, both type B components positively contribute to the control of the back EMF.

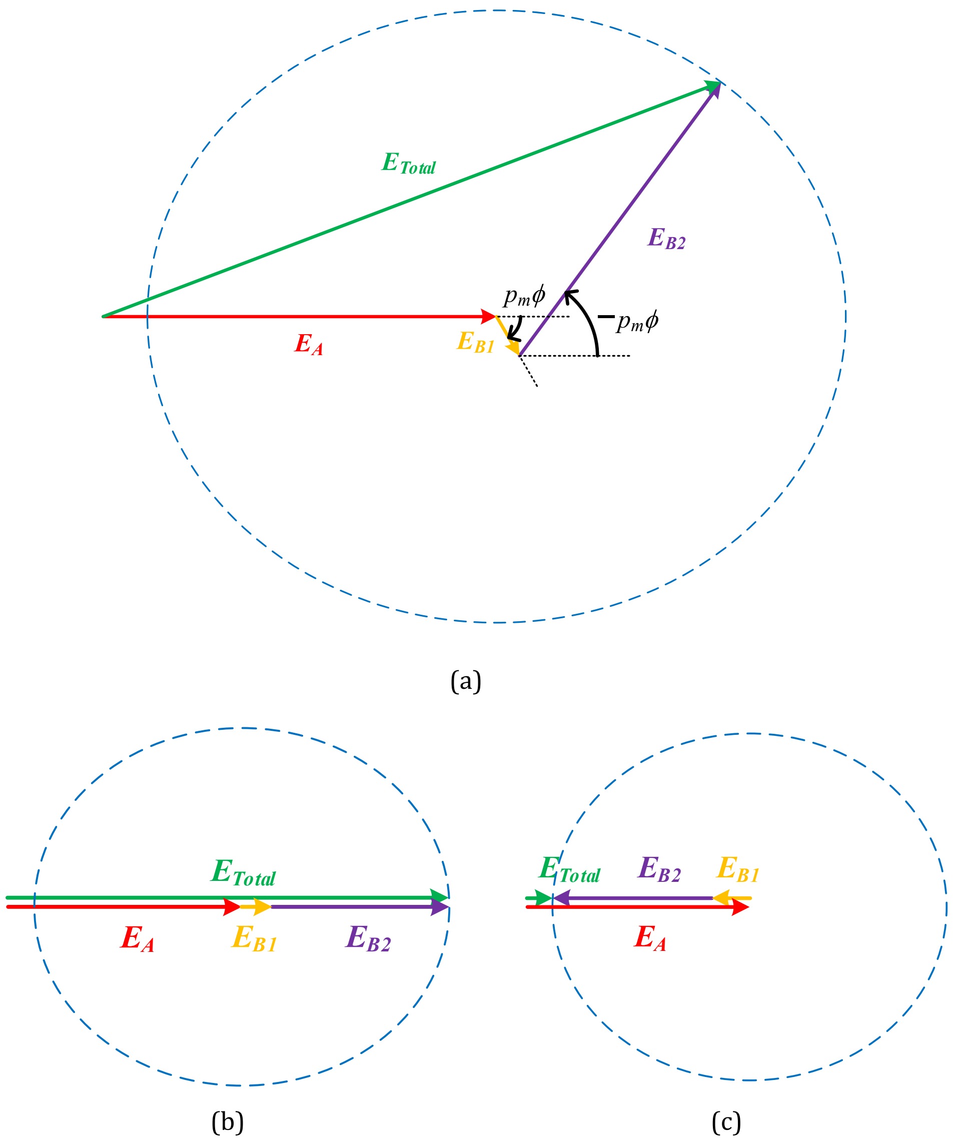

Fig. 5-7. Back EMF vector graph. (a) Showing diagram. (b) Maximum total back EMF position ($p_m\phi = 0°$). (c) Minimum total back EMF position ($p_m\phi = 180°$).

By adjusting the electrical initial phase angle of the modulator $p_m\phi$ from 0° to 180°, the total back EMF can vary with the range from $|E_{mA} - E_{mB1} - E_{mB2}|$ to $(E_{mA} + E_{mB1} + E_{mB2})$. Therefore, the total back EMF amplitude can be effectively controlled.

From (5-25) and (5-26), it should be observed that the amplitude of $\mathbf{E_{B1}}$ is significantly smaller than $\mathbf{E_{B2}}$. As the rotating speed of $\mathbf{E_{B1}}$ is $(\frac{p_r+p_m}{p_r-p_m})$ times higher than $\mathbf{E_{B2}}$; therefore, $\mathbf{E_{B2}}$ plays a major role in the control of the back EMF.

To obtain the widest control range of the back EMF, the amplitude of $\mathbf{E_{B2}}$ should be close to $\mathbf{E_A}$. From (5-24) and (5-26), we could observe that B_{mB2} is smaller than B_{mA}, as Λ_j is always smaller than $2\Lambda_0$. Therefore, ω_{B2} should be larger than ω_A, and the pole pair number of rotor should follow:

$$p_r > \frac{Z}{2} \tag{5-36}$$

5.3 Electromagnetic Performances Comparison and Analysis

5.3.1 Optimization Design

As mentioned in (5-36), four feasible stator/rotor pole pair combinations, i.e., the 12/7, 12/8, 12/10, and 12/11 have been designed for comparison. Four models are optimized independently by the nondominated sorted genetic algorithm-II (NSGA-II). The common design parameters of all models are listed in Table 5-2 and the variables to be optimized are listed in Table 5-3. The optimization goals are to maximize the output torque density K_T and minimize the maximum torque ripple ratio T_{rip} with the armature current density of 6 A/mm ^{2}. K_T and T_{rip} are defined as follows:

$$K_T = \frac{T_{avg}}{V} \tag{5-37}$$

$$T_{rip} = \frac{\max(T) - \min(T)}{T_{avg}} \cdot 100\% \tag{5-38}$$

where T_{avg} is the average torque of the outer rotor, and V is the volume of the electromagnetic part of the machine.

Table 5-2. The common design parameters of the optimized models

Item	12/7	12/8	12/10	12/11
Phase		3		
Number of slots		12		
Number of modulator segments		12		
Pole pair number of armature windings	7	8	10	11

Coil pitch (Slot)	1	1	2	5
Pole pair number of the rotor PMs	7	8	10	11
Outer diameter of the stator (mm)	190			
Axial length (mm)	50			
Length of the inner airgap (mm)	0.7			
Length of the outer airgap (mm)	0.5			
Rated armature current density (A/mm^2)	6			
Rated speed (rpm)	500			

Table 5-3. The optimizing variables of models

Item	Notation	Range			
		12/7	12/8	12/10	12/11
Width of the PMs (mm)	L_{pm}	[10,20]	[10,20]	[10,20]	[10,20]
Width of the modulator segments (°)	θ_m	[7.5,22.5]	[7.5,22.5]	[7.5,22.5]	[7.5,22.5]
Width of the stator teeth (mm)	b_t	[10,20]	[10,20]	[10,20]	[10,20]
Thickness of the PMs (mm)	h_{pm}	[3,8]	[3,7]	[3,5]	[3,5]
Thickness of the modulator segments (mm)	h_m	[5,10]	[5,10]	[5,10]	[5,10]
Height of stator slots (mm)	h_s	[10,18]	[10,18]	[10,18]	[10,18]
Height of stator yoke (mm)	h_{ys}	[8,20]	[8,20]	[8,20]	[8,20]

The optimization process flow chart is shown in Fig. 5-8. The optimization in this paper has 20 generations, with 100 designs in each generation. The Pareto fronts of four designs are presented in Fig. 5-9. The designs indicated by the red arrow in Fig. 5-9 are the final optimized designs. All final designs have the highest torque density when the torque ripple is below 10%.

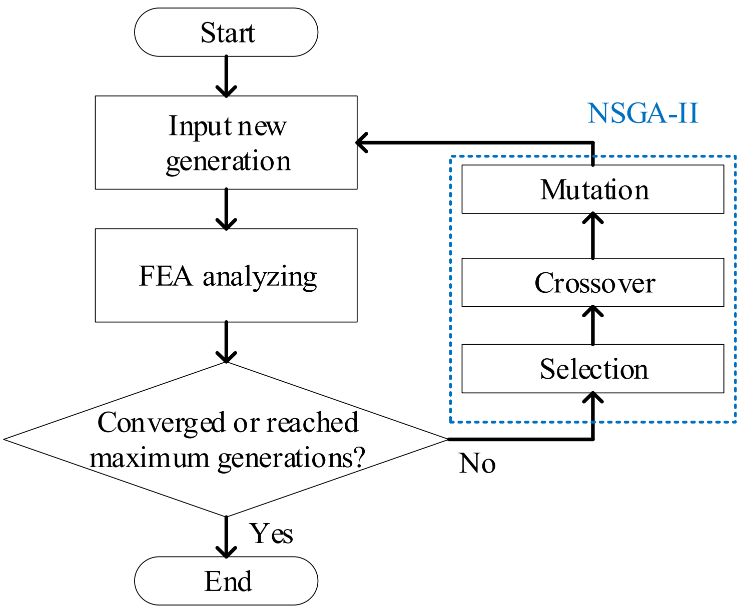

Fig. 5-8. The optimization flowchart using FEA and NSGA-II.

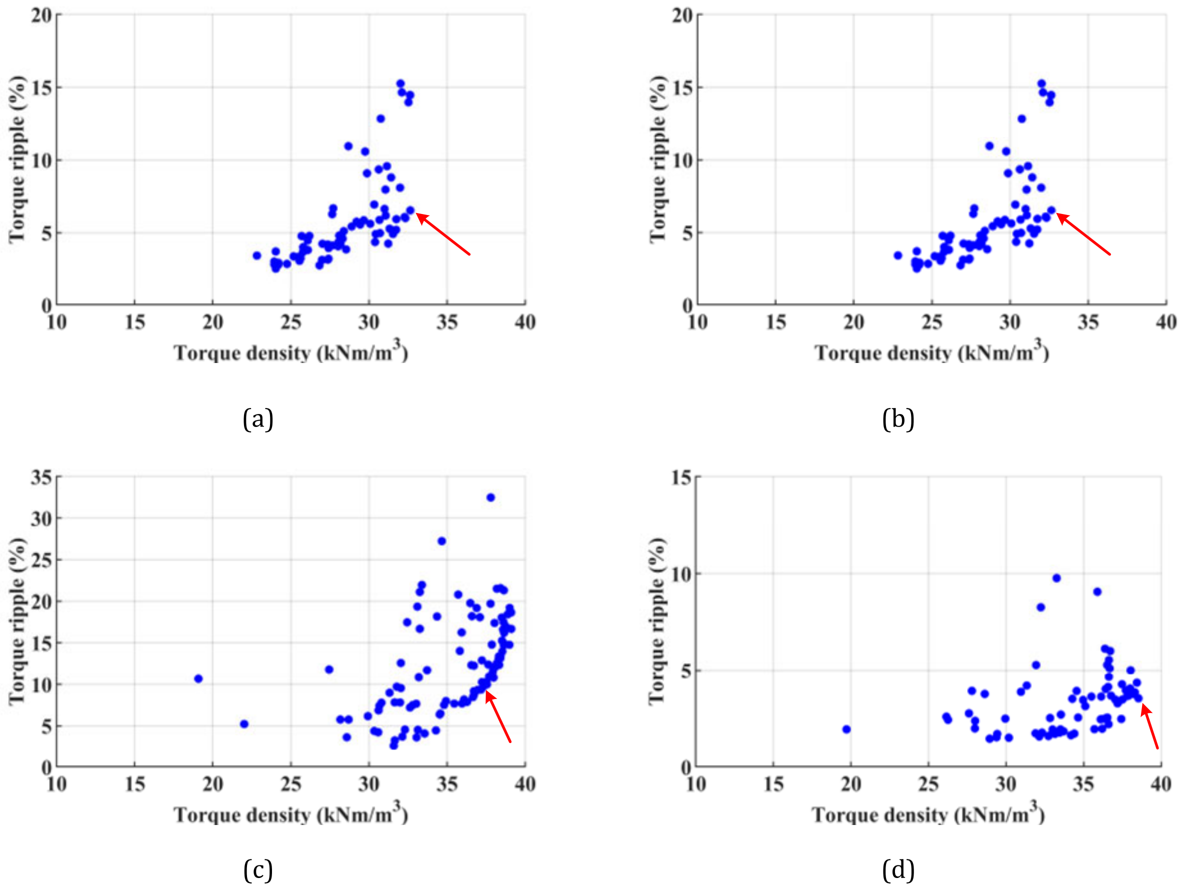

Fig. 5-9. The Pareto fronts of the GA. (a) 12/7. (b) 12/8. (c) 12/10. (d) 12/11.

5.3.2 Torque Performance

The curve of torque production and torque density per volume with different current densities under the rated speed is shown in Fig. 5-10. At the rated current density, the 12/11 design has the highest torque density, which is 38.4 kNm/m ^{3}. The torque density of the 12/7 design is 32.1 kNm/m ^{3}, which is 16% lower than the 12/11 design. However, it is worth mentioning that although the 12/7 design torque density is the lowest among the four cases, its torque density is still considered high compared to conventional PM machines, which are generally under 20 kNm/m ^{3}.

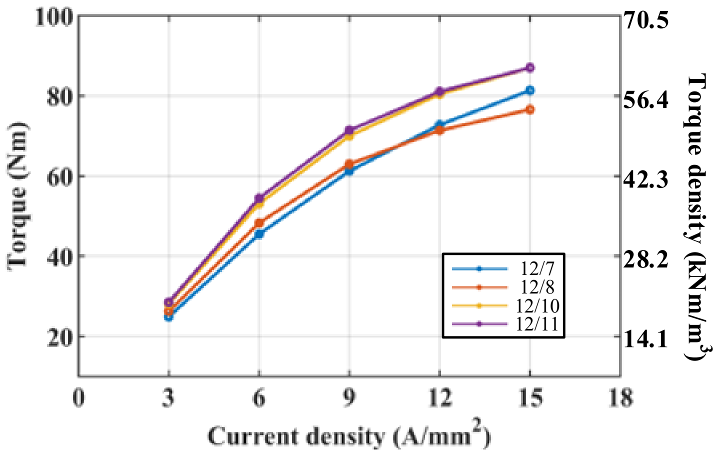

Fig. 5-10. The curve of current density vs. torque and torque density.

5.3.3 Harmonic Distribution

The calculated flux density distribution and the fast Fourier transform (3-FFT) analysis in the airgap of four cases are shown in Fig. 5-11. It can be observed that types A and B2 components are significantly higher than the other harmonics. To quantitatively analyze the contribution of each type of harmonic component, the back EMF contribution of the main working harmonics is calculated and shown in Table 5-4 using the analytical method based on (5-23). The amplitudes of types A and B2 components are significantly higher than type B1, which agrees with the FEM results. The amplitude of type B2 is significantly higher than type B1, which also agrees with the operation principles.

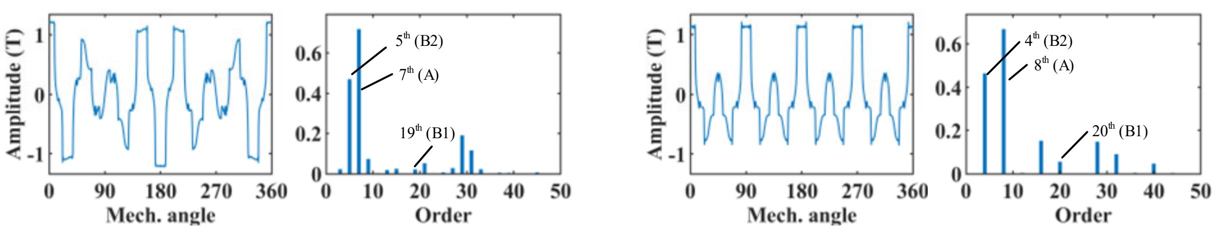

(a) (b)

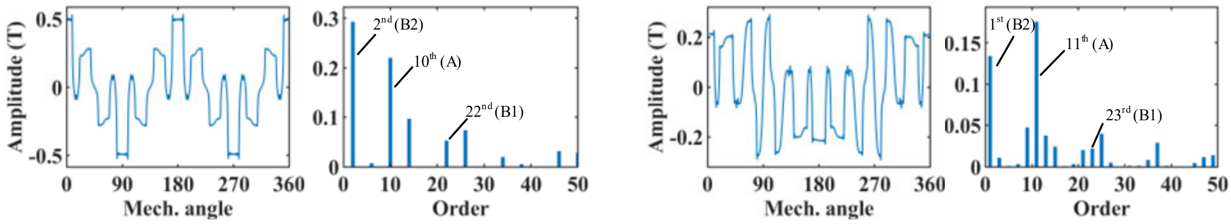

(c) (d)

Fig. 5-11. The flux density distribution and their FFT analysis in the airgap of four cases. (a) 12/7. (b) 12/8. (c) 12/10. (d) 12/11.

Table 5-4. Contribution of the harmonic components to back EMF by the analytical method.

Case	Type	Order	Flux Density $B_m(3-T)$	Winding Factor k_w	Angular Speed ω	Induced Voltage $E \propto B_m k_w \omega$
12/7	A	7	0.7178	0.933	Ω	0.6697Ω
	B1	19	0.0221	0.933	0.3864Ω	0.0076Ω
	B2	5	0.4704	0.933	1.4Ω	0.6144Ω
12/8	A	8	0.6679	0.866	Ω	0.5784Ω
	B1	20	0.0560	0.866	0.4Ω	0.0194Ω
	B2	4	0.4642	0.866	2Ω	0.8040Ω
12/10	A	10	0.2203	0.866	Ω	0.1907Ω
	B1	22	0.0528	0.866	0.4545Ω	0.0208Ω
	B2	2	0.2929	0.866	5Ω	1.2683Ω
12/11	A	11	0.1753	0.933	Ω	0.1636Ω
	B1	23	0.0220	0.933	0.4783Ω	0.0098Ω
	B2	1	0.1342	0.933	11Ω	1.3770Ω

In Table 5-4, it can be observed that for 12/7 design, the amplitude of type A induced voltage is almost equal to type B (3-i.e., the sum of the amplitude of types B1 and B2). For 12/8, 12/10, and 12/11 designs, their type B amplitude is higher than type A.

5.3.4 Voltage Regulation Ratio

The back EMF vector trajectory of four cases using FEM is shown in Fig. 5-12, and the curves of back EMF amplitude with the change in the initial phase angle are shown in Fig. 5-13.

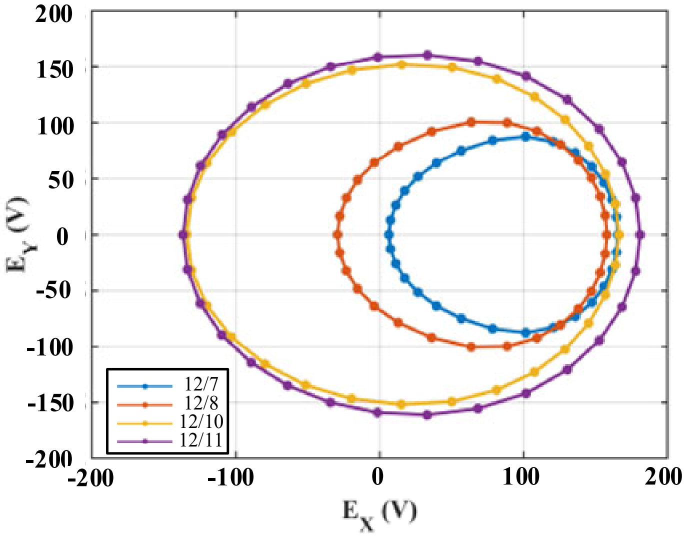

Fig. 5-12. Back EMF vector trajectory of four cases by FEM.

In Fig. 5-13, it can be observed that the 12/7 design has relatively the best flux controlling ability, as its types A and B component's amplitude are the closest among all four cases, as shown in Table 5-4. The 12/8 design is similar to the 12/7 configuration with notable drawbacks: Its type B component's amplitude is higher than the type A component, which makes the vector trajectory have a specific portion on the left side of y-axis, as shown in Fig. 5-12. For the 12/10 and 12/11 designs, in Table 5-4, it can be observed that the amplitude of the type B component is significantly higher than type A. As a result, although the type B component vector can rotate, the variation of the total back EMF amplitude is significantly smaller, which causes these two designs to have relatively weak flux controllability, as shown in Fig. 5-13.

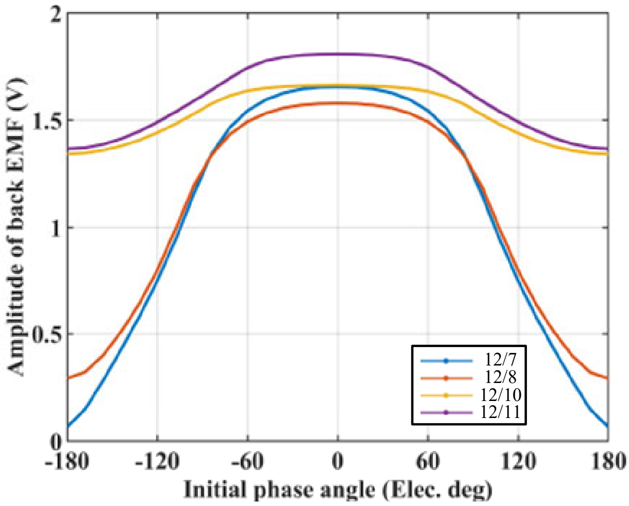

Fig. 5-13. The curves of back EMF amplitude vs. the initial phase angle.

To value the ability of flux control, the voltage regulation ratio (VRR) is introduced in this paper. The voltage regulation ratio of the analytical method and FEM is summarized and compared in Table 5-5, where E_A and E_B denote the back EMF amplitude of types A and B components, and E_{max} and E_{min} denote the maximum and the minimum of the back EMF amplitude. The voltage regulation ratio is defined as follows:

$$VRR = \frac{E_{max} - E_{min}}{E_{max}} \cdot 100\% \qquad (5\text{-}39)$$

Table 5-5. Analytical and FEM results of back EMF voltage regulation ratio.

Case	Analytical Method			FEM		
	$E_{min} = \lvert E_A - E_B \rvert$	$E_{max} = E_A + E_B$	VRR	$E_{min}\ (V)$	$E_{max}\ (V)$	VRR
12/7	0.0477 Ω	1.2917 Ω	96.3%	0.0644	1.6539	96.1%
12/8	|−0.2450Ω|	1.4018 Ω	82.5%	0.2924	1.5781	81.5%
12/10	|−1.0984Ω|	1.4799 Ω	25.8%	1.2410	1.6632	25.4%
12/11	|−1.2233Ω|	1.5504 Ω	21.1%	1.3855	1.8090	23.4%

The larger the VRR, the better the flux controllability that the design has. In Table 5-5, it can be found that the results of the analytical method agree with the results of the FEM, thus proving the validity of the operating principles. The VRR of the 12/7 design is significantly higher than its counterparts.

From the above analysis, a design guideline can be given: The best flux controllability can be obtained when the rotor pole pair number is slightly higher than half of the stator teeth number.

5.3.5 Overall Comparison

The overall comparison of four cases is listed in Table 5-6. The torque variation range is significantly smaller than the flux voltage regulation ratio. In Table 5-6, the 12/7 design has the best flux voltage regulation ratio and has a torque density of over 20 kNm/m ^{3}. Therefore, the 12/7 design is selected as the best design among the four cases.

Table 5-6. Overall comparison of the four cases.

Case	Torque Density at the Rated Current Density (kNm/m ^{3})	Voltage Regulation Ratio
12/7	32.1	96.1%
12/8	34.1	81.5%
12/10	37.4	25.4%
12/11	38.4	23.4%

5.4 VSCAVC Characteristics of the Selected Design

The design parameters and dimensions of the selected optimized 12/7 model are shown in Table 5-7.

Table 5-7. Design parameters and dimensions of the selected model.

Item	Value	Item	Value
Phase	3	Pole pair number of windings	7
Number of slots	12	Number of modulator blocks	12
Pole pair number of the rotor PMs	7	Outer diameter of the stator	190 mm
Inner diameter of the stator	122 mm	Length of the outer airgap	0.5 mm
Length of the inner airgap	0.7 mm	Length of the model	50 mm
Thickness of the modulator	4 mm	Embrace of the modulator	0.63
Thickness of the spoke PM	10 mm	Length of the spoke PM	20 mm
Number of turns	100	Rated speed	500 rpm

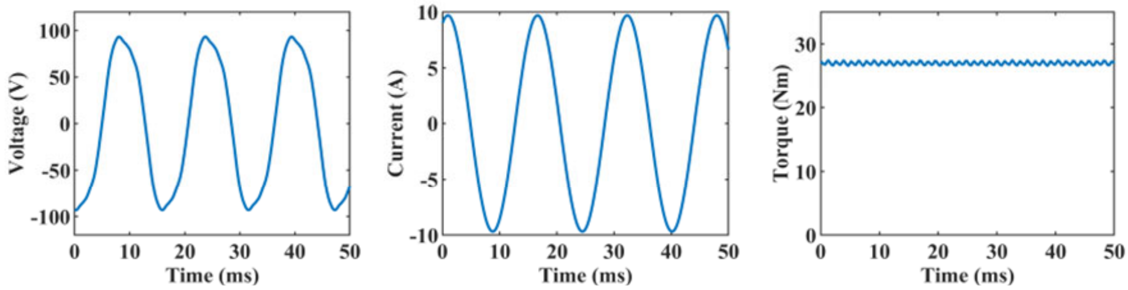

(a)

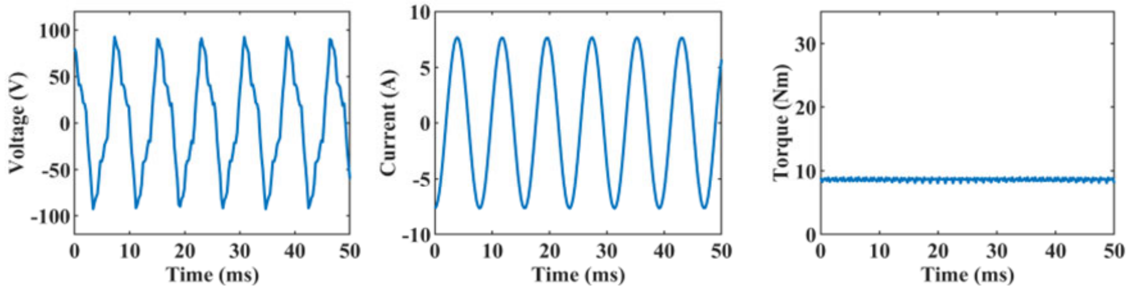

(b)

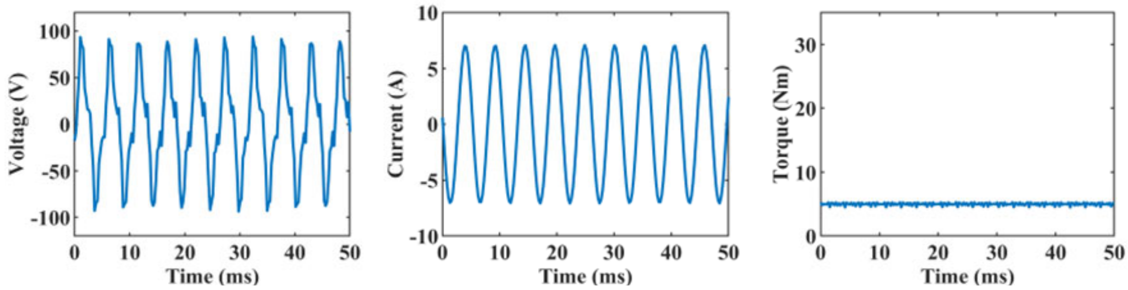

(c)

Fig. 5-14. VSCAVC steady-state characteristics of the selected 12/7 design with different rotor speeds and initial phase angles (in electrical degree). (a) $\Omega = 500$ rpm, $\phi = 0°$. (b) $\Omega = 1000$ rpm, $\phi = 108°$. (c) $\Omega = 1500$ rpm, $\phi = 120°$.

The VSCAVC steady-state characteristics of the 12/7 design are shown in Fig. 5-14. The generator operates at a speed of 500 rpm in the beginning, and the initial phase angle of the modulator is fixed at 0°. The amplitude of the voltage is 91 V. When the generator runs at 1000 and 1500 rpm to maintain amplitude, the modulator simultaneously adjusts to 108° and 120° in electrical degree. The simulation shows that the design model has good control over the voltage amplitude. The current curve is sinusoidal, and the torque curve is smooth, with a ripple under 5% of the average.

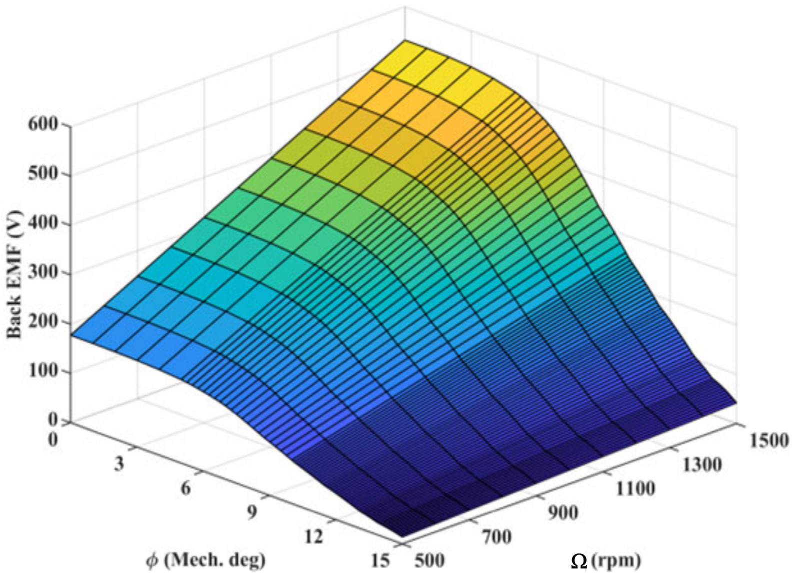

Fig. 5-15. The relationship of back EMF, initial phase angle, and rotating speed of the rotor.

5.5 Summary

This paper presents a novel mechanical flux-weakening design of spoke-type permanent magnet generator for a stand-alone power supply. The back EMF of all three working harmonics can obtain the same frequency and can be summed as vectors. By controlling the position of the adjustable modulator ring and using the modulation effect, the sum of the back EMF vector can be regulated, and the flux weakening can be smoothly achieved. With special pole pair selection, only one set of windings is needed, which simplifies manufacturing. Compared to conventional PMSMs, the mechanical method can have a wide range of flux weakening without the risk of PM demagnetization. VSCAVC can be applied to this machine.

The analytical model and operating principles are illustrated in this paper, and four optimized cases with different stator/rotor pole pairs are compared to show the advantageous performance of the proposed design. The 12/7 design with a voltage regulation ratio of 96.1% and a torque density of 32.1 kNm/m^3 is selected. The VSCAVC characteristics of the 12/7 design are analyzed, showing the outstanding performance of the selected design.

Chapter 6 A Novel Consequent-Pole Contra-Rotating Machine with Zero-Sequence Current Excitation

6.1 Introduction

Nowadays, people's concerns about environmental protection keep growing. Electric drives for the propulsion system of the ship are prevalent. Contra-rotating machines have high potential applications in direct driving of two counter-rotating propellers, which may be used in ship propulsion systems to effectively recover energy from the main propeller slipstream rotational flow [56].

Generally, there are two types of contra-rotating machines, namely the winding configured type and the magnetic geared type. For the winding configured type, in recent studies, most designs have two rotors with the same pole pair number and a stator with two layers. By shifting two phases of windings on the stator's upper layer and down layer, these designs achieve the goal of contra-rotating function [152]. However, their windings in this design intersect, making manufacturing relatively difficult.

For the magnetic geared type, the machine is composed of a stator, a concentrical inner and outer rotor. Two rotors can rotate at different speeds by controlling the stator winding based on flux modulation theory [87, 102]. When two rotors are used as output, using only one set of windings is insufficient. An auxiliary winding that controls the outer rotor alone is needed to get full control. Two-windings-based magnetic geared type machines have caused control strategies to be complex. In addition, when one winding is not working, a certain slot area is wasted. An integrated winding structure has been proposed to eliminate this issue [98, 116]. Nevertheless, two inverters are still needed for this topology.

All the abovementioned structures are rare-earth permanent magnet (PM) excited due to their high power density, high efficiency, and high reliability. However, conventional PM machines have the drawback of limited control ability because of the fixed PM excitation, which results in a narrow speed range. Conventionally, PM machines use control methods like d-q transformation to use the direct axis current to partially demagnetize the magnets for achieving field control. These approaches have the problems like irreversible PM demagnetization and significant temperature rise [153-155]. For easy flux weakening methods, many structures have been investigated. In [156], a consequent-pole PM (CPPM) machine with a circumferential DC field winding in the stator was proposed. This structure enables the flux in the air gap to be controlled in a wide range without the risk of PMs' demagnetization, as the DC flux path for field controlling is parallel to the PM flux path. Using this construction can significantly simplify the control of flux weakening. Other variants include axial flux type CPPM machines [157, 158] and vernier type CPPM machines [159, 160]. Nevertheless, the armature winding and the DC windings are separated, making the structure bulky.

In [161] and [162], an integrated field and its armature control are proposed for a variable reluctance machine. This machine's drive current is biased, including both AC and DC components. The direct current generates the exciting field, while the alternating current produces the rotating armature field. Because this drive system could remove the original DC exciting windings, the system cost and copper loss could be reduced, and the efficiency could be improved. In [163], a zero-sequence winding structure is proposed, which combines the DC excitation winding and the AC armature winding through the zero-sequence winding control strategy.

In this paper, a novel hybrid excitation PM-assisted consequent-pole contra-rotating machine (HECP-CRM) is proposed. The flux can be enhanced or weakened by adjusting the zero-sequence current. PMs have no risk of demagnetization because the PM and DC flux paths are parallel. The zero-sequence current based armature winding replace the original DC and AC windings, making the structure more compact. The segmented stator can reduce iron loss and simplify the manufacturing process.

This paper is organized as follows: Section 6.2 presents the configuration of the proposed machine. The operating principles are introduced in Section 6.3. The performances of the proposed machine are analyzed in Section 6.4. Finally, the conclusions are drawn in Section 6.5.

6.2 Machine Configuration

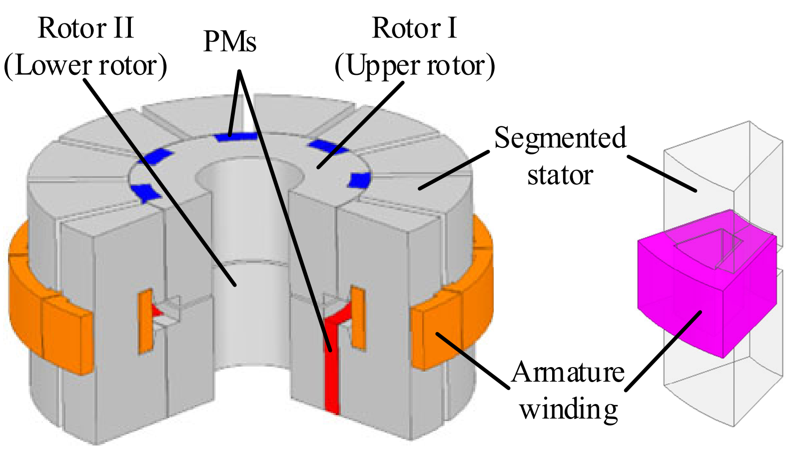

Fig. 6-1. The 3D view of the proposed HECP-CRM.

The configuration of the HECP-CRM is shown in Fig. 6-1. The design involves 12 C-shaped stator segments. The segmented stator does not have a common yoke, which can effectively reduce the iron loss. The concentrated zero-sequence armature windings are wounded on each stator segment.

A 7 pole-pair upper rotor (rotor I) and a 5 pole-pair lower rotor (rotor II) are placed inside the stator segments, shown in Fig. 6-2(a) and Fig. 6-2(b), where the ferrite PMs on two rotors are in opposite radial magnetization directions. Two rotors have the consequent pole structure and rotate in opposite directions. An axial air gap between two rotors allows the DC flux to path through axially.

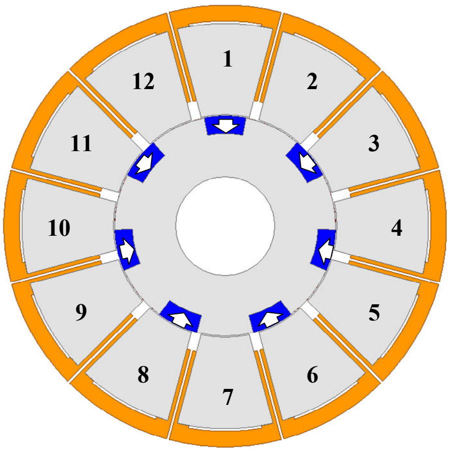

(a)

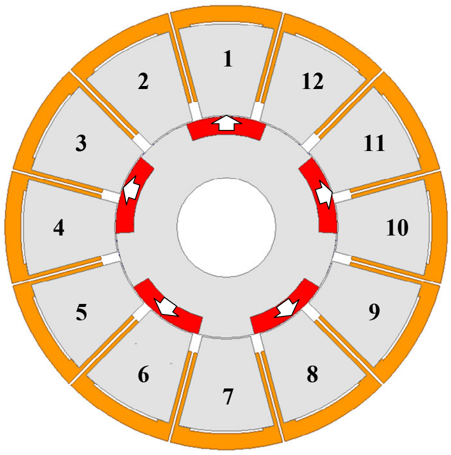

(b)

Fig. 6-2. The 2D views of HECP-CRM. (a) Rotor I. (b) Rotor II.

6.3 Operating Principles

6.3.1 Rotor Pole Pair Selection

To make two rotors rotate in different directions with the same set of winding, two rotors should have the following relationship:

$$p_u + p_d = kZ, \ k = 1,2,3 \dots \tag{6-1}$$

where p_u and p_d are the pole pair number (PPN) of the upper and Rotor II, respectively. For the proposed design, $k = 1$. Under (6-1), the slot angle of the

Rotor I α_u and Rotor II α_d can be calculated as:

$$\alpha_u = \frac{2\pi p_u}{Z} \tag{6-2}$$

$$\alpha_d = \frac{2\pi p_d}{Z} = 2\pi - \alpha_u \tag{6-3}$$

From (6-3), as the slot angles' sum of two rotors equals 2π, two flux components with reversed directions are generated in the airgap while the winding arrangement is the same [164]. For the proposed design, the phasor diagram is shown in Fig. 6-3, where we can observe the two winding arrangements can become the same by vertical flipping.

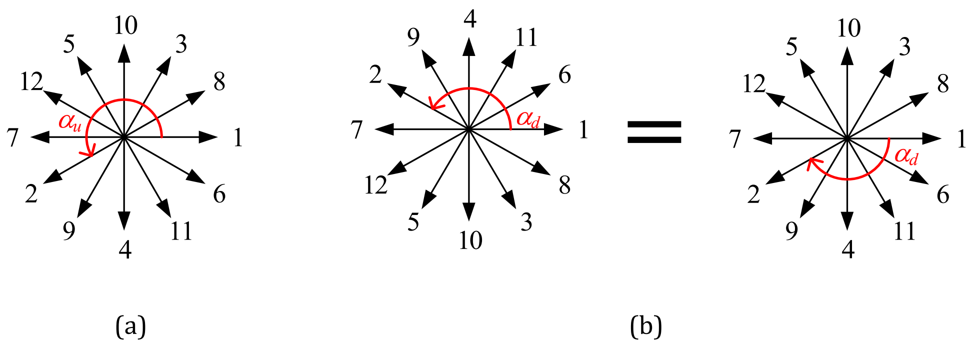

Fig. 6-3. The phasor diagram of two rotors. (a) Rotor I. (b) Rotor II.

The winding frequency can be calculated as

$$f = \frac{p_u n_u}{60} = -\frac{p_d n_d}{60} \tag{6-4}$$

where n_u and n_d are the speed of the upper and Rotor II, respectively. To make the speed of the two rotors closer and let the winding be concentrated, the PPN of the two rotors in the proposed model is designed as

$$\begin{cases} p_u = \frac{Z}{2} + 1 \\ p_d = \frac{Z}{2} - 1 \end{cases} \tag{6-5}$$

6.3.2 Flux Controlling

Based on the biased DC current direction of the armature coils, the machine has two working modes. The flux path of two different modes is shown in Fig. 6-4.

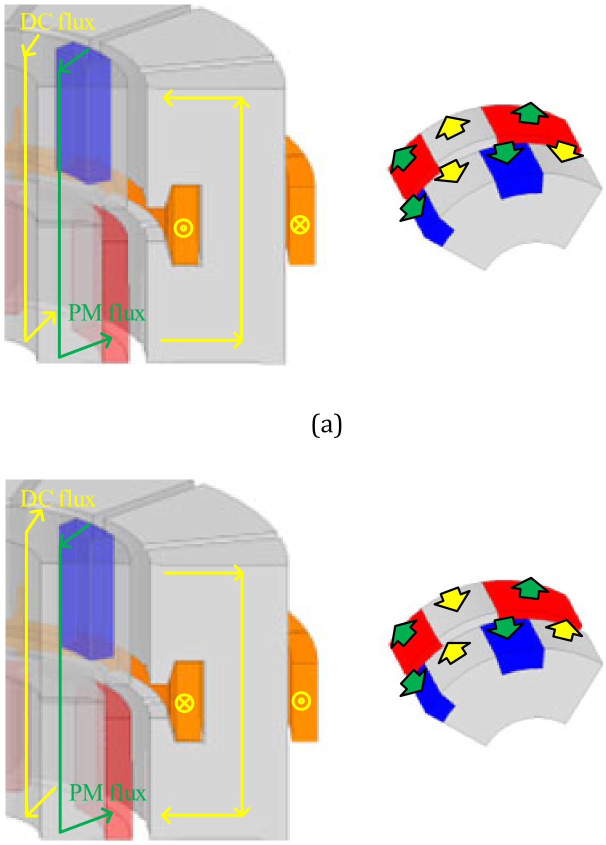

(a)

(b)

Fig. 6-4. The flux control principle. (a) Flux-weakened mode. (b) Flux-enhanced mode.

In the flux-weakened mode, the biased-DC current is injected into the armature winding, as shown in Fig. 6-4(a). The iron poles have the same polarity as the PMs on the same rotor. This makes the flux variation smaller than in normal mode, making the armature hard to generate back electromotive force (EMF), thus realizing the flux weakening.

Fig. 6-4(b) shows the flux-enhanced mode. On the same rotor, the iron poles and the PMs' directions are different. The flux variation in this mode is more significant than in the normal mode. Hence the flux linkage of the rotor is enhanced.

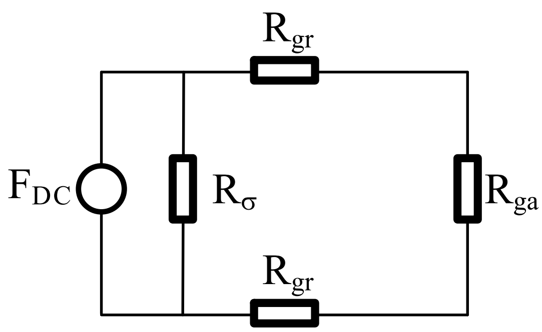

Fig. 6-5. Magnetic circuit of the DC biased excitation.

The magnetic circuit of the DC-biased excitation is shown in Fig. 6-5. In Fig. 6-5, F_{DC} is the magnetomotive force of the DC-biased current, which can be calculated as

$$F_{DC} = NI_{DC} \tag{6-6}$$

where N is the number of turns, and I_{DC} is the DC-biased current. R_σ, R_{gr}, and R_{ga} are the magnetic resistance of leakage, radial airgap, and axial airgap, which can be calculated as

$$R_\sigma = \frac{l_\sigma}{\mu_0 S_\sigma} \tag{6-7}$$

$$R_{gr} = \frac{g_r}{\mu_0 S_r} \tag{6-8}$$

$$R_{ga} = \frac{g_a}{\mu_0 S_a} \tag{6-9}$$

where l_σ is the length of stator teeth tips, g_r and g_a are the length of radial and axial airgap, respectively.μ_0 is the magnetic permeability of the vacuum. S_σ is the area of stator teeth tips, S_r is the radial surface area of iron poles, and S_a is the axial area of two rotors.

6.3.3 Winding Configuration

The winding configuration and the drive circuit are shown in Fig. 6-6. The coils are divided into two groups, winding A1, B1 and C1 as group I, and winding A2, B2, and C2, as group II. Group I and II's neutral points are connected, enabling the zero-sequence current to pass through the windings. When defining the zero-sequence current that passing through the winding to the neutral point as positive, the current of each winding can be expressed as

$$\begin{cases} I_{A1} = I_m \cos(2\pi f t) + I_0 \\ I_{B1} = I_m \cos(2\pi f t + 2\pi/3) + I_0 \\ I_{C1} = I_m \cos(2\pi f t - 2\pi/3) + I_0 \\ I_{A2} = I_m \cos(2\pi f t) - I_0 \\ I_{B2} = I_m \cos(2\pi f t + 2\pi/3) - I_0 \\ I_{C2} = I_m \cos(2\pi f t - 2\pi/3) - I_0 \end{cases} \tag{6-10}$$

where I_m is the maximum amplitude of AC current, and I_0 is the zero-sequence current:

$$I_0 = I_{DC} \tag{6-11}$$

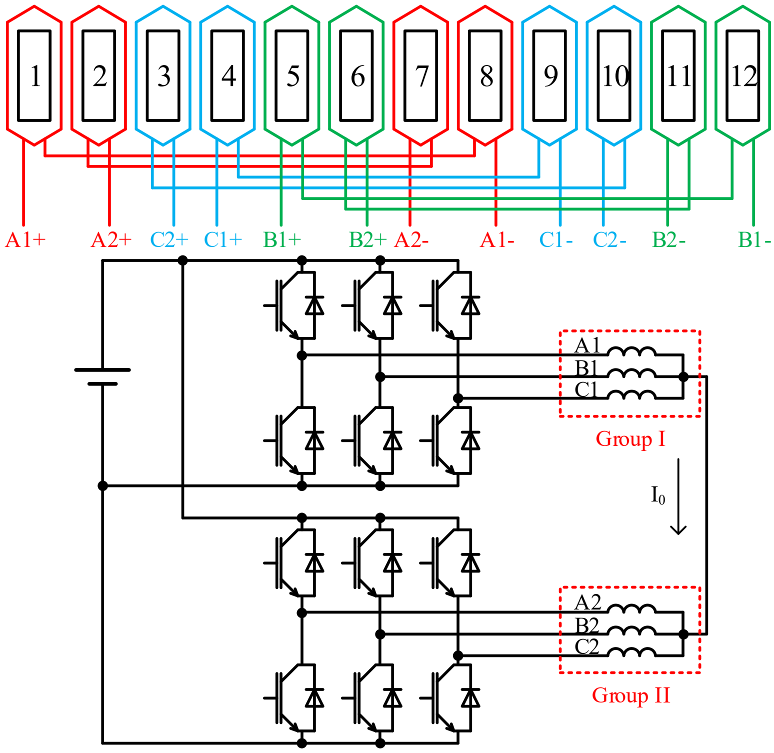

Fig. 6-6. The zero-sequent current based winding configuration and the drive circuit.

With this configuration, the AC armature winding is the same, i.e., winding A1 and A2 have no phase difference, which create the same rotating magnetic field. The DC zero-sequence current directions of the two groups are different, i.e., when the zero-sequence current for group I is positive, then that for group II is negative. This enables the DC flux of all stator segments to be in the same direction in this design. The flux generated by the DC zero-sequence current can be liberally adjusted and used for the flux controlling without extra circumferential auxiliary winding as in [156].

The DC-biased and AC winding can be combined using this winding configuration, making the whole structure more compact. Furthermore, the DC and AC current ratio can be freely adjusted, which increases the utilization rate of the slot area.

6.4 Performance Analysis

The model has been analyzed by the 3D finite element method (3D-FEM). The specifications of the model are shown in Table 6-1. As shown in Table 6-1, the PM material used here is Y30BH, whose residual flux density is just 0.33T, which makes it possible to couple with the zero-sequence winding for flux weakening by using pure electricity excitation.

Table 6-1. The specification of the proposed model

Parameter	Value
Number of stator segments	12
PPN of Rotor I	7
PPN of Rotor II	5
Stator outer diameter	164mm
Stator inner diameter	90mm
Rotor inner diameter	40mm
Radial air gap length	0.5mm
Axial air gap length	0.5mm
Core length	80mm
Pole axial length	35mm
Number of turns	80
PM thickness	7mm
Material of PM	Y30BH

Fig. 6-7 presents the airgap flux distribution in normal mode. From Fig. 6-7, when no DC-biased current is injected, the air gap flux over the ferrite PMs remains constant and in different directions. A 5-pole-pair and a 7-pole-pair field can be clearly observed.

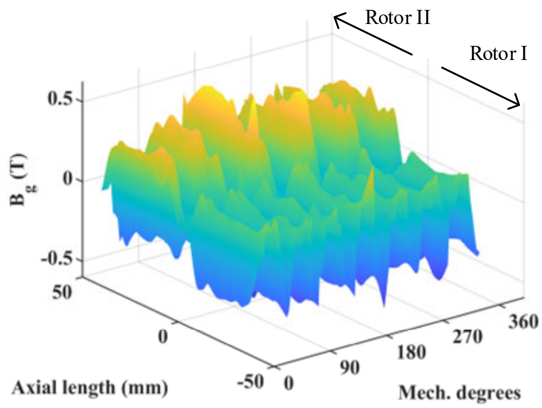

Fig. 6-7. Air gap flux distribution in normal mode ($J_{DC} = 0$).

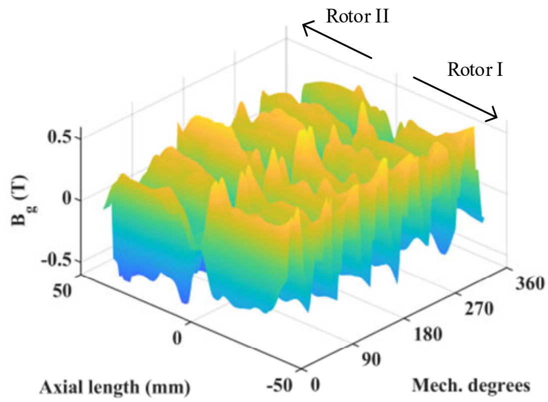

Fig. 6-8. Air gap flux distribution in flux-enhanced mode ($J_{DC} = 6A/mm^2$).

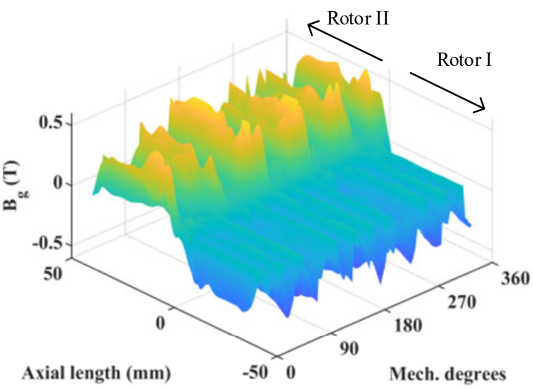

Fig. 6-9. Air gap flux distribution in flux-weakened mode ($J_{DC} = -6A/mm^2$).

Fig. 6-8 and Fig. 6-9 present the airgap flux distribution in flux weakening and enhancing mode. When the DC-biased excitation is injected in different directions, the polarity of the flux in the iron pole area changes accordingly. Compared to the normal mode, the flux density variation is much bigger in the flux-enhanced mode, shown in Fig. 6-8. In Fig. 6-9, the flux variation under one rotor area is much smaller. The flux distribution shown in Fig. 6-8 and Fig. 6-9 match the operating principles.

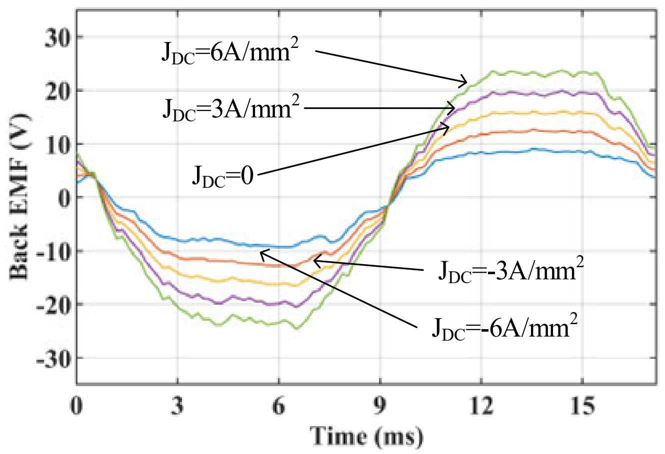

(a)

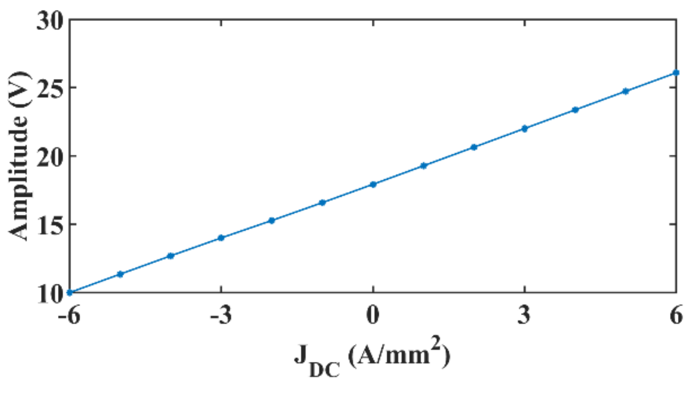

(b)

Fig. 6-10. The relationship of back EMF and zero-sequence current excitation current. (a) Waveforms. (b) Amplitude vs. DC-biased current density.

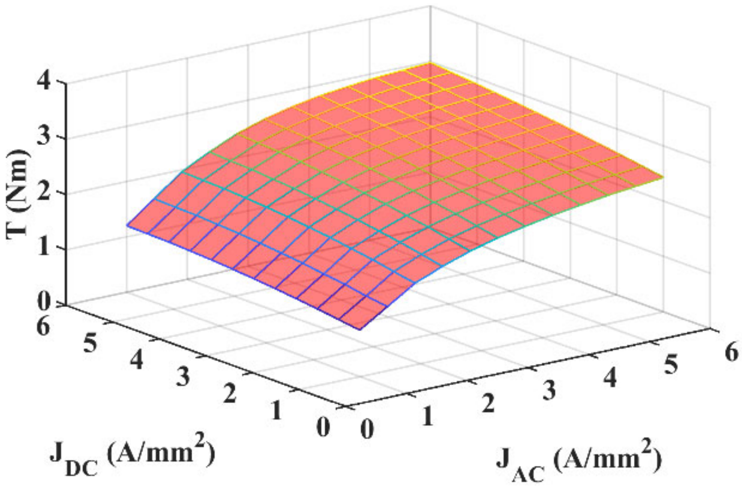

(a)

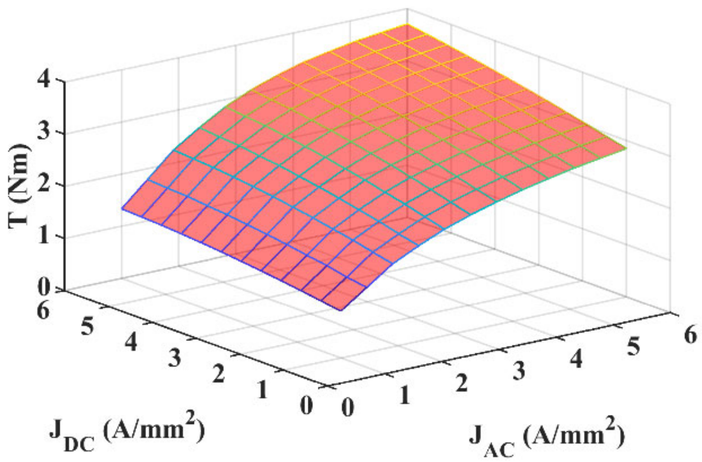

(b)

Fig. 6-11. The loaded torque (a) Rotor I. (b) Rotor II.

When rotor I rotates at 500 rpm and rotor II rotates at 700 rpm, the frequency of the armature is 58.3Hz. Under this state, the relationship between back electromotive force (EMF) and the DC-biased current density J_{DC} is shown in Fig. 6-10. The waveforms shown in Fig. 6-10(a) are relatively sinusoidal. The amplitude of the back EMF varies with DC-biased current density, shown in Fig. 6-10(b). The back EMF can change with a variation of $\pm$40%, which achieves good field controllability.

The loaded torque of both rotors is shown in Fig. 6-11. For both rotors, compared to DC-biased current, the increase in AC current has a greater incremental effect on the torque. As the flux density of rotor I is slightly higher than that of the rotor II field, the torque of the rotor II is higher than that of the rotor I.

6.5 Summary

A novel hybrid-excitation PM-assisted consequent-pole contra-rotating machine is proposed in this paper, which shows good field controllability. The proposed model has the following merits:

- The zero-sequence armature winding integrates the DC and AC winding, eliminating the conventional circumferential auxiliary winding and making the structure more compact.
- The integrated winding enables the ratio of AC and DC current to be freely adjusted, making the slot area further utilized.
- The flux can be regulated effectively with a wide range by changing the zero-sequence current excitation.
- As the flux path of the PM and DC are in parallel, PMs have no risk of demagnetization.
- The segmented stator can reduce iron loss and simplify manufacturing processing.

A 3-phase 12-coil model with a 7 pole-pair rotor and a 5 pole-pair rotor has been designed. Three working modes of the proposed machine have been analyzed by the 3D-FEM. The onload and noload status have been investigated. The analysis results have proved the model to have field controllability of $\pm$40%.

Chapter 7 Conclusion and Future Work

7.1 Conclusion

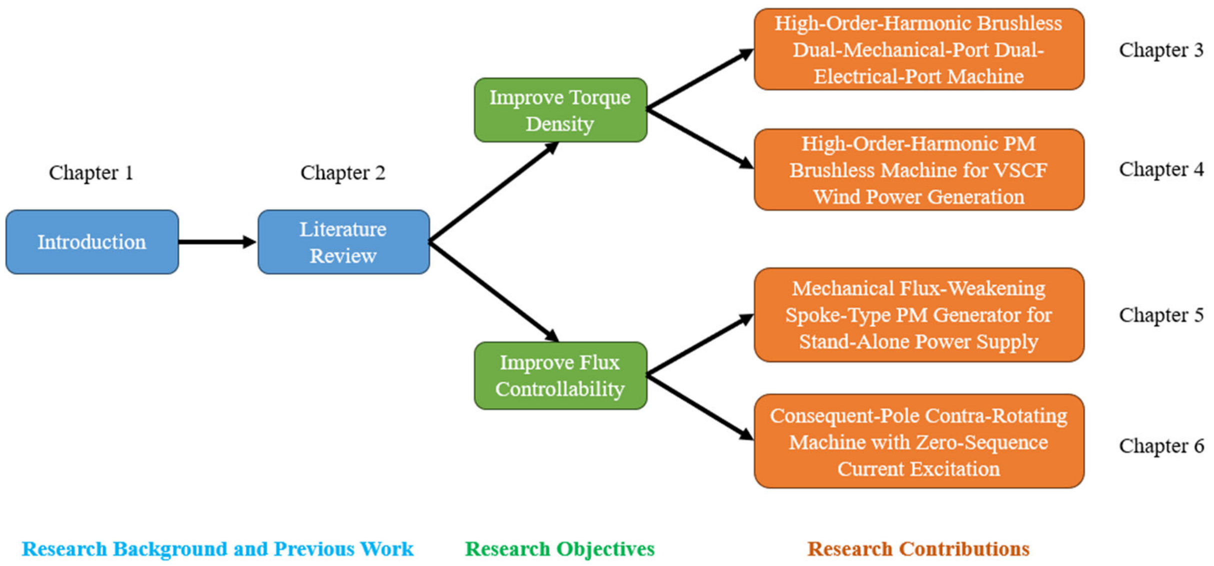

Fig. 7-1. The outline of the thesis.

This thesis focuses on improving the torque density and flux controllability of multiport machines. Various topologies of multiport machines are designed and analyzed, and their potential industrial applications are investigated. The outline of this thesis is shown in Fig. 7-1, which is structured and summarized as follows:

Chapter 2 provides an extensive literature review of multiport machines from the perspective of dual-mechanical-port (DMP) machines, discussing their working principles and different topologies. The three types of multiport machines based on power flow relationships, namely single-power-flow DMP (SPF-DMP), parallel-power-flow DMP (PPF-DMP), and hybrid-power-flow DMP (HPF-DMP), are examined in terms of their advantages and challenges.

This literature review identifies research gaps that serve as the research objectives for this thesis.

In Chapter 3, a novel brushless dual-electrical-port dual-mechanical-port machine (BLDDM) structure is proposed to further enhance torque density. This design utilizes high-order harmonic modulation to artificially enhance the third-harmonic component of the airgap flux density in the inner airgap while keeping the fundamental component unchanged in the outer airgap. Two windings fully utilize both components in this design. Analytical and finite element method (FEM) analysis are employed to determine the flux density ratio between the third harmonic and the fundamental components, which is approximately 4.28, with a rotating speed ratio of 3. The pole pair number (PPN) of the modulation winding is determined as $p_{wm} = 3p_{ro} - p_{ri}$. FEM simulations compare the optimized prototype with a conventional design of the same dimensions and PPN for both windings, demonstrating a 50% increase in back electromotive force (EMF) in the modulation winding and a 45.7% larger torque in the magnetic-geared machine (MGM) portion. A prototype is manufactured and tested, validating the working principles and FEM simulations.

Chapter 4 introduces a novel brushless dual-electrical-port dual-mechanical-port doubly fed machine (BLDD-DFM) aimed at minimizing energy consumption in the control winding and improving overall efficiency, specifically for variable speed constant frequency (VSCF) applications. This design utilizes high-order harmonic modulation to amplify the third-harmonic component of the airgap flux density. By reducing the slip ratio through high-order modulation, energy consumption in the control winding is reduced by threefold compared to conventional designs. FEM simulations compare the prototype with a conventional design of the same dimensions, revealing a fivefold increase in back EMF in the control winding and a 73% higher back EMF compared to the power winding in the conventional design. Under rated conditions, the proposed design exhibits maximum torque improvements of 23.03% for the outer rotor and 144.08% for the inner rotor compared to the conventional design, with reduced torque ripple. Experimental results from a prototype confirm the feasibility of the design, and VSCF experiments validate its performance under static and dynamic conditions.

In Chapter 5, a novel mechanical flux-weakening design of a spoke-type permanent magnet generator for stand-alone power supply is presented. This design regulates the back EMF vector by controlling the position of a mechanical adjustable modulator ring and utilizing the modulation effect, enabling smooth flux weakening. Special pole pair selection allows for the use of only one set of windings, simplifying manufacturing. The proposed design, with a voltage regulation ratio of 96.1% and a torque density of 32.1 kNm/m^3, is analyzed for its variable speed constant amplitude voltage control (VSCAVC) characteristics, demonstrating outstanding performance.

Chapter 6 proposes a hybrid-excitation consequent-pole contra-rotating machine. This design integrates the DC and AC windings using a zero-sequence armature winding, eliminating the need for a conventional circumferential auxiliary winding and resulting in a more compact structure. The integrated winding allows for flexible adjustment of the AC and DC current ratio, effectively utilizing the slot area. Flux regulation is achieved by changing the zero-sequence current excitation, and the parallel flux path of the permanent magnets and DC winding eliminates the risk of demagnetization. The segmented stator reduces iron loss and simplifies manufacturing. A 3-phase 12-coil model with a 7 pole-pair rotor and a 5 pole-pair rotor is designed, and the three working modes are analyzed using 3D-FEM. The study confirms the field controllability of the model, with a range of ±40%, through analysis of the no-load and load conditions.

7.2 Future Work

The future work of the research basically includes the following parts:

1) Prototype manufacturing: The prototypes that designed in Chapter 5 and 6 will be built for further studying, which are the mechanical flux-weakening spoke-type PM generator and the hybrid-excitation consequent-pole contra-rotating machine. The manufacturing error, the winding ending issue, and large prototype issue should be taken into special consideration.
2) Power factor issue: Other from the manufacturing complexity, as the proposed multiport machines are mostly based on flux modulation, the low power factor is also a common shortage for the multiport machine. More structures that can reduce the flux leakage should be tried on the multiport machines.
3) Pole-changing multiport machine: A pole-changing multiport machine can be designed based on high-order modulation with an extended speed range, utilizing the inherent fundamental and third harmonics of the PMs. The proposed design effectively utilizes both components by employing flux modulation using the fundamental and third harmonics of the PM excitation. Specifically, the third harmonic modulation increases the back EMF at low speeds, while the fundamental

modulation allows for a decrease in the inverter frequency at high speeds. This design incorporates three sets of windings: two modulation windings for speed control and one set for torque control. The adoption of the integrated winding design for the modulation windings can be used for reducing the number of windings sets and optimizes coil space utilization.

4) Hybrid-excited multiport machine: The “AC+DC” integrated winding design can be further developed for the hybrid-excited MGM type multiport machine. This design combines zero-sequence DC excitation and consequent-pole PM excitation as the hybrid excitation source. However, overcoming the high magnetic resistance of the two-layer airgap in the MGM-type structure remains a challenge, given the relatively weak MMF of the DC excitation.
5) Multi-set integrated winding: The current integrated "AC+AC" winding design only allows for the integration of two winding sets. To achieve the integration of more winding sets, such as all three windings for pole-changing multiport machine, the utilization of coil space can be significantly improved, leading to enhanced overall efficiency. However, the challenge lies in reducing the number of inverters required for the multi-set integrated winding.

References

[1] A. E. Fitzgerald, C. Kingsley, and S. D. Umans, *Electric machinery*. McGraw-Hill, 2003.

[2] M. Cheng, P. Han, G. Buja, and M. G. Jovanovic, "Emerging Multiport Electrical Machines and Systems: Past Developments, Current Challenges, and Future Prospects," *IEEE Transactions on Industrial Electronics,* vol. 65, no. 7, pp. 5422-5435, 2018, doi: 10.1109/tie.2017.2777388.

[3] F. Punga and L. Schon, "Der neue kollektorlose einphasenmotor der Firma Krupp," *Elektrotechnische Zeitschrift,* vol. 47, no. 29, pp. 877-881, 1926.

[4] S. Eriksson and C. Sadarangani, "A four-quadrant HEV drive system," in *Proceedings IEEE 56th Vehicular Technology Conference*, 2002, vol. 3: IEEE, pp. 1510-1514.

[5] L. Xu, "A new breed of electric machines-basic analysis and applications of dual mechanical port electric machines," in *2005 International Conference on Electrical Machines and Systems*, 2005, vol. 1: IEEE, pp. 24-31.

[6] K. Atallah, S. Calverley, R. Clark, J. Rens, and D. Howe, "A new PM machine topology for low-speed, high-torque drives," in *2008 18th International Conference on Electrical Machines*, 2008: IEEE, pp. 1-4.

[7] X. Luo and S. Niu, "A Novel Contra-Rotating Power Split Transmission System for Wind Power Generation and Its Dual MPPT Control Strategy," *IEEE Transactions on Power Electronics,* vol. 32, no. 9, pp. 6924-6935, 2017, doi: 10.1109/tpel.2016.2629021.

[8] Y. Wang, S. Niu, and W. Fu, "Sensitivity Analysis and Optimal Design of a Dual Mechanical Port Bidirectional Flux-Modulated Machine," *IEEE Transactions on Industrial Electronics,* vol. 65, no. 1, pp. 211-220, 2018, doi: 10.1109/tie.2017.2719620.

[9] H. Zhao, C. Liu, Z. Song, and W. Wang, "Analytical Modeling of a Double-Rotor Multiwinding Machine for Hybrid Aircraft Propulsion," *IEEE Transactions on Transportation Electrification,* vol. 6, no. 4, pp. 1537-1550, 2020, doi: 10.1109/tte.2020.2997607.

[10] J. F. Douglas, "Characteristics of induction motors with permanent-magnet excitation," *Transactions of the American Institute of Electrical Engineers. Part III: Power Apparatus and Systems,* vol. 78, no. 3, pp. 221-225, 1959.

[11] J. K. Sedivy, "Induction motor with free-rotating DC excitation," *IEEE Transactions on*

Power Apparatus and Systems, no. 4, pp. 463-469, 1967.

[12] B. Ackermann, "Single-phase induction motor with permanent magnet excitation," *IEEE transactions on magnetics,* vol. 36, no. 5, pp. 3530-3532, 2000.

[13] A. M. Gazdac, C. S. Martis, A. M. Mabwe, and K. Biro, "Analysis of material influence on the performance of the dual-rotor Permanent Magnet Induction Machine," in *2012 13th International Conference on Optimization of Electrical and Electronic Equipment (OPTIM)*, 2012: IEEE, pp. 453-459.

[14] A. Gazdac, A. M. Mabwe, C. Martis, F. Betin, and K. Biro, "Analytical design algorithm and FEM analysis of the dual-rotor Permanent Magnet Induction Machine," in *2012 XXth International Conference on Electrical Machines*, 2012: IEEE, pp. 1185-1191.

[15] M. Cheng, X. Sun, F. Yu, and W. Hua, "Design and analysis of permanent magnet induction generator for grid-connected direct-driven wind power application," in *2015 Tenth International Conference on Ecological Vehicles and Renewable Energies (EVER)*, 2015: IEEE, pp. 1-8.

[16] M. Venturini and F. Leonardi, "High torque, low speed joint actuator based on PM brushless motor and magnetic gearing," in *Conference Record of the 1993 IEEE Industry Applications Conference Twenty-Eighth IAS Annual Meeting*, 1993: IEEE, pp. 37-42.

[17] K. Atallah and D. Howe, "A novel high-performance magnetic gear," *IEEE Transactions on magnetics,* vol. 37, no. 4, pp. 2844-2846, 2001.

[18] K. T. Chau, D. Zhang, J. Z. Jiang, C. Liu, and Y. Zhang, "Design of a Magnetic-Geared Outer-Rotor Permanent-Magnet Brushless Motor for Electric Vehicles," *IEEE Transactions on Magnetics,* vol. 43, no. 6, pp. 2504-2506, 2007, doi: 10.1109/tmag.2007.893714.

[19] T. V. Frandsen, P. O. Rasmussen, and K. K. Jensen, "Improved motor intergrated permanent magnet gear for traction applications," in *2012 IEEE energy conversion congress and exposition (ECCE)*, 2012: IEEE, pp. 3332-3339.

[20] P. O. Rasmussen, T. V. Frandsen, K. K. Jensen, and K. Jessen, "Experimental Evaluation of a Motor-Integrated Permanent-Magnet Gear," *IEEE Transactions on Industry Applications,* vol. 49, no. 2, pp. 850-859, 2013, doi: 10.1109/tia.2013.2242423.

[21] T. V. Frandsen *et al.*, "Motor Integrated Permanent Magnet Gear in a Battery Electrical Vehicle," *IEEE Transactions on Industry Applications,* vol. 51, no. 2, pp. 1516-1525, 2015, doi: 10.1109/tia.2014.2360016.

[22] S. S. Nielsen, R. K. Holm, and P. O. Rasmussen, "Conveyor System With a Highly Integrated Permanent Magnet Gear and Motor," *IEEE Transactions on Industry*

Applications, vol. 56, no. 3, pp. 2550-2559, 2020, doi: 10.1109/tia.2020.2977877.

[23] K. Atallah, J. Rens, S. Mezani, and D. Howe, "A Novel “Pseudo” Direct-Drive Brushless Permanent Magnet Machine," *IEEE Transactions on Magnetics,* vol. 44, no. 11, pp. 4349-4352, 2008, doi: 10.1109/tmag.2008.2001509.

[24] L. Wang, J. Shen, and M. Jin, "Design of a multi-power-terminals permanent magnet machine with magnetic field modulation," in *2011 International Conference on Electrical Machines and Systems*, 2011: IEEE, pp. 1-6.

[25] Z. Deng, L. Jian, G. Peng, Y. Shi, and J. Wei, "Modeling of Magnetic-Geared Permanent Magnet Machines with Sandwiched Armature Stator," in *2016 IEEE Vehicle Power and Propulsion Conference (VPPC)*, 2016: IEEE, pp. 1-6.

[26] H. Zhao, C. Liu, Z. Dong, R. Huang, and X. Li, "Design and Optimization of a Magnetic-Geared Direct-Drive Machine With V-Shaped Permanent Magnets for Ship Propulsion," *IEEE Transactions on Transportation Electrification,* vol. 8, no. 2, pp. 1619-1633, 2022, doi: 10.1109/tte.2021.3124891.

[27] N. Niguchi and K. Hirata, "Torque-Speed Characteristics Analysis of a Magnetic-Geared Motor Using Finite Element Method Coupled With Vector Control," *IEEE Transactions on Magnetics,* vol. 49, no. 5, pp. 2401-2404, 2013, doi: 10.1109/tmag.2013.2239271.

[28] N. Niguchi, P. Slawomir Wiak, and K. Hirata, "Magnetic-geared motors with high transmission torque density," *COMPEL: The International Journal for Computation and Mathematics in Electrical and Electronic Engineering,* vol. 34, no. 2, pp. 428-438, 2015, doi: 10.1108/compel-07-2014-0182.

[29] A. Penzkofer, G. Cooke, M. Odavic, and K. Atallah, "Coil Excited Pseudo Direct Drive Electrical Machines," *IEEE Transactions on Magnetics,* vol. 53, no. 1, pp. 1-11, 2017, doi: 10.1109/tmag.2016.2603966.

[30] G. Cooke and K. Atallah, "“Pseudo” Direct Drive Electrical Machines With Alternative Winding Configurations," *IEEE Transactions on Magnetics,* vol. 53, no. 11, pp. 1-8, 2017, doi: 10.1109/tmag.2017.2703662.

[31] X. Yin, Y. Fang, X. Huang, and P.-D. Pfister, "Analytical Modeling of a Novel Vernier Pseudo-Direct-Drive Permanent-Magnet Machine," *IEEE Transactions on Magnetics,* vol. 53, no. 6, pp. 1-4, 2017, doi: 10.1109/tmag.2017.2660241.

[32] Q. Gan, Y. Fang, and P.-D. Pfister, "A Novel Concentrated-Winding Vernier Pseudo-Direct-Drive Permanent-Magnet Machine," *IEEE Transactions on Magnetics,* vol. 58, no. 2, pp. 1-5, 2022, doi: 10.1109/tmag.2021.3100058.

[33] Q. Wang, X. Qin, and P.-D. Pfister, "A Vernier pseudo-direct-drive permanent-magnet machine," in *2018 XIII International Conference on Electrical Machines (ICEM)*, 2018: IEEE, pp. 2023-2029.

[34] W. Li, K. T. Chau, and J. Z. Jiang, "Application of Linear Magnetic Gears for Pseudo-Direct-Drive Oceanic Wave Energy Harvesting," *IEEE Transactions on Magnetics,* vol. 47, no. 10, pp. 2624-2627, 2011, doi: 10.1109/tmag.2011.2146233.

[35] X. Yin, Y. Fang, and P. D. Pfister, "High-torque-density pseudo-direct-drive permanent-magnet machine with less magnet," *IET Electric Power Applications,* vol. 12, no. 1, pp. 37-44, 2017, doi: 10.1049/iet-epa.2017.0297.

[36] H. Huang, D. Li, W. Kong, and R. Qu, "Torque performance of pseudo direct-drive machine with Halbach consequent pole," in *2018 IEEE Energy Conversion Congress and Exposition (ECCE)*, 2018: IEEE, pp. 3286-3293.

[37] M. Bouheraoua, J. Wang, and K. Atallah, "Speed control for a pseudo direct drive permanent-magnet machine with one position sensor on low-speed rotor," *IEEE transactions on industry applications,* vol. 50, no. 6, pp. 3825-3833, 2014.

[38] J. Wang and K. Atallah, "Modeling and control of ‘pseudo’direct-drive brushless permanent magnet machines," in *2009 IEEE International Electric Machines and Drives Conference*, 2009: IEEE, pp. 870-875.

[39] M. Bouheraoua, J. Wang, and K. Atallah, "Observer based state feedback controller design for pseudo direct drive® using genetic algorithm," in *6th IET International Conference on Power Electronics, Machines and Drives (PEMD 2012)*, 2012: IET, pp. 1-6.

[40] R. Qu and T. A. Lipo, "Dual-rotor, radial-flux, toroidally wound, permanent-magnet machines," *IEEE Transactions on Industry Applications,* vol. 39, no. 6, pp. 1665-1673, 2003.

[41] R. Qu and T. Lipo, "Design and optimization of dual-rotor, radial-flux, toroidally-wound, permanent-magnet machines," in *38th IAS Annual Meeting on Conference Record of the Industry Applications Conference, 2003.*, 2003, vol. 2: IEEE, pp. 1397-1404.

[42] R. Qu, M. Aydin, and T. A. Lipo, "Performance comparison of dual-rotor radial-flux and axial-flux permanent-magnet BLDC machines," in *IEEE International Electric Machines and Drives Conference, 2003. IEMDC'03.*, 2003, vol. 3: IEEE, pp. 1948-1954.

[43] R. Qu and T. A. Lipo, "Design and Parameter Effect Analysis of Dual-Rotor, Radial-Flux, Toroidally Wound, Permanent-Magnet Machines," *IEEE Transactions on Industry Applications,* vol. 40, no. 3, pp. 771-779, 2004, doi: 10.1109/tia.2004.827444.

[44] Y.-H. Yeh, M.-F. Hsieh, and D. G. Dorrell, "Different arrangements for dual-rotor dual-output radial-flux motors," *IEEE Transactions on Industry Applications,* vol. 48, no. 2, pp. 612-622, 2011.

[45] B. R. Kumar and K. S. Kumar, "Design of a new Dual Rotor Radial Flux BLDC motor with Halbach array magnets for an electric vehicle," in *2016 IEEE International Conference on Power Electronics, Drives and Energy Systems (PEDES)*, 2016: IEEE, pp. 1-5.

[46] S. Song, Y. Xu, H. Tian, and X. Gong, "Design and simulation of dual rotor permanent magnet brushless DC motor," in *2014 17th International Conference on Electrical Machines and Systems (ICEMS)*, 2014: IEEE, pp. 1591-1595.

[47] Y. Yang, N. Schofield, and A. Emadi, "Double-Rotor Switched Reluctance Machine (DRSRM)," *IEEE Transactions on Energy Conversion,* vol. 30, no. 2, pp. 671-680, 2015, doi: 10.1109/tec.2014.2378211.

[48] S. Niu, S. L. Ho, W. N. Fu, and L. L. Wang, "Quantitative Comparison of Novel Vernier Permanent Magnet Machines," *IEEE Transactions on Magnetics,* vol. 46, no. 6, pp. 2032-2035, 2010, doi: 10.1109/tmag.2010.2042429.

[49] T. J. Woolmer and M. McCulloch, "Analysis of the yokeless and segmented armature machine," in *2007 IEEE International Electric Machines & Drives Conference*, 2007, vol. 1: IEEE, pp. 704-708.

[50] R. Madhavan and B. G. Fernandes, "Axial Flux Segmented SRM With a Higher Number of Rotor Segments for Electric Vehicles," *IEEE Transactions on Energy Conversion,* vol. 28, no. 1, pp. 203-213, 2013, doi: 10.1109/tec.2012.2235068.

[51] M. Jiang, W. Fu, and S. Niu, "Design and Analysis of a Novel Dual-Airgap Dual Permanent Magnet Vernier Machine," *IEEE Access,* vol. 9, pp. 57188-57197, 2021, doi: 10.1109/access.2021.3072918.

[52] T. Zou, D. Li, R. Qu, J. Li, and D. Jiang, "Analysis of a Dual-Rotor, Toroidal-Winding, Axial-Flux Vernier Permanent Magnet Machine," *IEEE Transactions on Industry Applications,* vol. 53, no. 3, pp. 1920-1930, 2017, doi: 10.1109/tia.2017.2657493.

[53] D. Winterborne, N. Stannard, L. Sjoberg, and G. Atkinson, "An Air-Cooled YASA Motor for in-Wheel Electric Vehicle Applications," *IEEE Transactions on Industry Applications,* vol. 56, no. 6, pp. 6448-6455, 2020, doi: 10.1109/tia.2020.3025267.

[54] B. Cheng, G. Pan, and Z. Mao, "Analytical Calculation and Optimization of the Segmented-Stator Dual-Rotor Axial Flux Permanent Magnet Motors," *IEEE Transactions on Magnetics,* vol. 56, no. 11, pp. 1-9, 2020, doi: 10.1109/tmag.2020.3020589.

[55] K.-S. Min, B.-J. Chang, and H.-W. Seo, "Study on the Contra-Rotating Propeller system design and full-scale performance prediction method," *International Journal of Naval Architecture and Ocean Engineering,* vol. 1, no. 1, pp. 29-38, 2009.

[56] F. Caricchi, F. Crescimbini, and E. Santini, "Basic principle and design criteria of axial-flux PM machines having counterrotating rotors," *IEEE Transactions on Industry Applications,* vol. 31, no. 5, pp. 1062-1068, 1995.

[57] G. Liu, G. Qiu, J. Shi, and F. Zhang, "Study on Counter-Rotating Dual-Rotor Permanent Magnet Motor for Underwater Vehicle Propulsion," *IEEE Transactions on Applied Superconductivity,* vol. 28, no. 3, pp. 1-5, 2018, doi: 10.1109/tasc.2018.2802482.

[58] D. Luo, R. He, S. Huang, and X. Su, "Optimized Vector Control strategy for Contrarotating Permanent Magnet Synchronous Motor under serious unbalanced load adopting torque compensation," in *2019 22nd International Conference on Electrical Machines and Systems (ICEMS)*, 2019: IEEE, pp. 1-6.

[59] F. Zhang, G. Liu, Y. Shen, and F. Wang, "Characteristic study on a novel PMSM with opposite-rotation dual rotors," in *2007 International Conference on Electrical Machines and Systems (ICEMS)*, 2007: IEEE, pp. 805-809.

[60] M. Ranlof, G. Connor, and U. Lundin, "Simulation of a radial flux permanent magnet generator with two contra-rotating rotors," in *2008 18th International Conference on Electrical Machines*, 2008: IEEE, pp. 1-6.

[61] M. Ranlöf and U. Lundin, "Finite Element Analysis of a Permanent Magnet Machine with Two Contra-rotating Rotors," *Electric Power Components and Systems,* vol. 37, no. 12, pp. 1334-1347, 2009, doi: 10.1080/15325000903055271.

[62] M. J. Hoeijmakers and M. Rondel, "The electrical variable transmission in a city bus," in *2004 IEEE 35th Annual Power Electronics Specialists Conference (IEEE Cat. No. 04CH37551)*, 2004, vol. 4: IEEE, pp. 2773-2778.

[63] X. Zhu, D. Fan, L. Mo, Y. Chen, and L. Quan, "Multiobjective Optimization Design of a Double-Rotor Flux-Switching Permanent Magnet Machine Considering Multimode Operation," *IEEE Transactions on Industrial Electronics,* vol. 66, no. 1, pp. 641-653, 2019, doi: 10.1109/tie.2018.2818643.

[64] L. Xu, "Dual-mechanical-port electric machines-a new concept in design and analysis of electric machines," in *Fourtieth IAS Annual Meeting. Conference Record of the 2005 Industry Applications Conference, 2005.*, 2005, vol. 4: IEEE, pp. 2828-2834.

[65] L. Xu, Y. Zhang, and X. Wen, "Multioperational Modes and Control Strategies of Dual-

Mechanical-Port Machine for Hybrid Electrical Vehicles," *IEEE Transactions on Industry Applications,* vol. 45, no. 2, pp. 747-755, 2009, doi: 10.1109/tia.2009.2013575.

[66] A. V. Sant, V. Khadkikar, W. Xiao, and H. H. Zeineldin, "Four-Axis Vector-Controlled Dual-Rotor PMSM for Plug-in Electric Vehicles," *IEEE Transactions on Industrial Electronics,* vol. 62, no. 5, pp. 3202-3212, 2015, doi: 10.1109/tie.2014.2387094.

[67] Y. Liu, D. Cheng, Y. Sui, J. Bai, C. Tong, and W. Tong, "Magnetic System Study of a Compound-Structure Permanent-Magnet Synchronous Machine for HEVs," *IEEE Transactions on Industry Applications,* vol. 48, no. 6, pp. 1797-1807, 2012, doi: 10.1109/tia.2012.2221451.

[68] P. Zheng, E. Nordlund, P. Thelin, and C. Sadarangani, "Investigation of the winding current distribution in a 4-quadrant-transducer prototype machine," *IEEE transactions on magnetics,* vol. 41, no. 5, pp. 1972-1975, 2005.

[69] E. Nordlund and S. Eriksson, "Test and verification of a four-quadrant transducer for HEV applications," in *2005 IEEE Vehicle Power and Propulsion Conference*, 2005: IEEE, p. 5 pp.

[70] X. Sun and M. Cheng, "Thermal analysis and cooling system design of dual mechanical port machine for wind power application," *IEEE Transactions on Industrial Electronics,* vol. 60, no. 5, pp. 1724-1733, 2012.

[71] P. Zheng, R. Liu, P. Thelin, E. Nordlund, and C. Sadarangani, "Research on the cooling system of a 4QT prototype machine used for HEV," *IEEE transactions on energy conversion,* vol. 23, no. 1, pp. 61-67, 2008.

[72] S. Zhu, M. Cheng, and X. Sun, "Mechanical design of outer-rotor structure for dual mechanical port machine," in *2011 International Conference on Electrical Machines and Systems*, 2011: IEEE, pp. 1-6.

[73] X. Sun, M. Cheng, S. Zhu, and J. Zhang, "Coupled electromagnetic-thermal-mechanical analysis for accurate prediction of dual-mechanical-port machine performance," *IEEE Transactions on Industry Applications,* vol. 48, no. 6, pp. 2240-2248, 2012.

[74] J. Wang, K. Atallah, and S. D. Carvley, "A Magnetic Continuously Variable Transmission Device," *IEEE Transactions on Magnetics,* vol. 47, no. 10, pp. 2815-2818, 2011, doi: 10.1109/tmag.2011.2157470.

[75] K. Atallah, J. Wang, S. D. Calverley, and S. Duggan, "Design and Operation of a Magnetic Continuously Variable Transmission," *IEEE Transactions on Industry Applications,* vol. 48, no. 4, pp. 1288-1295, 2012, doi: 10.1109/tia.2012.2199451.

[76] P. Zheng, J. Bai, C. Tong, Y. Sui, Z. Song, and Q. Zhao, "Investigation of a Novel Radial Magnetic-Field-Modulated Brushless Double-Rotor Machine Used for HEVs," *IEEE Transactions on Magnetics,* vol. 49, no. 3, pp. 1231-1241, 2013, doi: 10.1109/tmag.2012.2217347.

[77] H. Zhao, C. Liu, and Z. Song, "Design of an Effective Double-Rotor Machine With Robust Mechanical Structure," *IEEE Transactions on Magnetics,* vol. 56, no. 1, pp. 1-7, 2020, doi: 10.1109/tmag.2019.2951107.

[78] J. Bai, J. Liu, P. Zheng, Y. Liu, H. Gao, and Y. Sui, "Low-Loss Design and Analysis of Magnetic-Field Modulated Brushless Double-Rotor Machine," *IEEE Transactions on Magnetics,* vol. 54, no. 11, pp. 1-5, 2018, doi: 10.1109/tmag.2018.2847330.

[79] M. Wang, C. Tong, Z. Song, J. Liu, and P. Zheng, "Performance Analysis of an Axial Magnetic-Field-Modulated Brushless Double-Rotor Machine for Hybrid Electric Vehicles," *IEEE Transactions on Industrial Electronics,* vol. 66, no. 1, pp. 806-817, 2019, doi: 10.1109/tie.2018.2844810.

[80] H. Zhao, C. Liu, Z. Song, and J. Yu, "Analytical Modeling and Comparison of Two Consequent-Pole Magnetic-Geared Machines for Hybrid Electric Vehicles," *Energies,* vol. 12, no. 10, 2019, doi: 10.3390/en12101888.

[81] C. Tong, P. Zheng, Q. Wu, J. Bai, and Q. Zhao, "A Brushless Claw-Pole Double-Rotor Machine for Power-Split Hybrid Electric Vehicles," *IEEE Transactions on Industrial Electronics,* vol. 61, no. 8, pp. 4295-4305, 2014, doi: 10.1109/tie.2013.2281169.

[82] M. Wang, P. Zheng, C. Tong, Q. Zhao, and G. Qiao, "Research on a transverse-flux brushless double-rotor machine for hybrid electric vehicles," *IEEE Transactions on Industrial Electronics,* vol. 66, no. 2, pp. 1032-1043, 2018.

[83] L. Jian and K.-T. Chau, "Design and analysis of a magnetic-geared electronic-continuously variable transmission system using finite element method," *Progress In Electromagnetics Research,* vol. 107, pp. 47-61, 2010.

[84] L. Jing, W. Tang, T. Wang, T. Ben, and R. Qu, "Performance analysis of magnetically geared permanent magnet brushless motor for hybrid electric vehicles," *IEEE Transactions on Transportation Electrification,* vol. 8, no. 2, pp. 2874-2883, 2022.

[85] S. Niu, S. L. Ho, and W. N. Fu, "A Novel Double-Stator Double-Rotor Brushless Electrical Continuously Variable Transmission System," *IEEE Transactions on Magnetics,* vol. 49, no. 7, pp. 3909-3912, 2013, doi: 10.1109/tmag.2013.2248347.

[86] S. Niu, S. L. Ho, and W. N. Fu, "Design of a Novel Electrical Continuously Variable

Transmission System Based on Harmonic Spectra Analysis of Magnetic Field," *IEEE Transactions on Magnetics,* vol. 49, no. 5, pp. 2161-2164, 2013, doi: 10.1109/tmag.2013.2243116.

[87] Y. Wang, S. Niu, and W. Fu, "Sensitivity analysis and optimal design of a dual mechanical port bidirectional flux-modulated machine," *IEEE Transactions on Industrial Electronics,* vol. 65, no. 1, pp. 211-220, 2017.

[88] S. Niu, Y. Liu, S. L. Ho, and W. N. Fu, "Development of a Novel Brushless Power Split Transmission System for Wind Power Generation Application," *IEEE Transactions on Magnetics,* vol. 50, no. 11, pp. 1-4, 2014, doi: 10.1109/tmag.2014.2331075.

[89] L. Sun, M. Cheng, J. Zhang, and L. Song, "Analysis and Control of Complementary Magnetic-Geared Dual-Rotor Motor," *IEEE Transactions on Industrial Electronics,* vol. 63, no. 11, pp. 6715-6725, 2016, doi: 10.1109/tie.2016.2581768.

[90] L. Sun, M. Cheng, H. Wen, and L. Song, "Motion Control and Performance Evaluation of a Magnetic-Geared Dual-Rotor Motor in Hybrid Powertrain," *IEEE Transactions on Industrial Electronics,* vol. 64, no. 3, pp. 1863-1872, 2017, doi: 10.1109/tie.2016.2627018.

[91] X. Ren, D. Li, R. Qu, and T. Zou, "A brushless dual-mechanical-port dual-electrical-port machine with spoke array magnets in flux modulator," *IEEE Transactions on Magnetics,* vol. 53, no. 11, pp. 1-6, 2017.

[92] X. Ren, D. Li, R. Qu, W. Kong, X. Han, and T. Pei, "Analysis of Spoke-Type Brushless Dual-Electrical-Port Dual-Mechanical-Port Machine With Decoupled Windings," *IEEE Transactions on Industrial Electronics,* vol. 66, no. 8, pp. 6128-6140, 2019, doi: 10.1109/tie.2018.2870395.

[93] J. Liu, J. Bai, G. Liu, Y. Wang, and P. Zheng, "Investigation of an Integrated Magnetic-Field-Modulated Brushless Double-Rotor Machine With an Improved PM Rotor," *IEEE Transactions on Magnetics,* vol. 57, no. 2, pp. 1-6, 2021, doi: 10.1109/tmag.2020.3015249.

[94] Z. Liang, X. Ren, D. Li, R. Qu, and X. Han, "Analysis of a Spoke-Array Brushless Dual-Electrical-Port Dual-Mechanical-Port Machine With Reluctance Rotor," *IEEE Transactions on Industrial Electronics,* vol. 68, no. 4, pp. 2999-3011, 2021, doi: 10.1109/tie.2020.2982084.

[95] Z. Liang, R. Xiang, D. Li, and R. Qu, "Design process of spoke-array brushless dual-electrical-port dual-mechanical-port machine," in *2020 International Conference on Electrical Machines (ICEM)*, 2020, vol. 1: IEEE, pp. 1978-1984.

[96] H. Chen, A. M. El-Refaie, Y. Zuo, S. Cai, L. Cao, and C. H. T. Lee, "Comparative Study

and Design Optimization of a Dual-Mechanical-Port Electric Machine for Hybrid Electric Vehicle Applications," *IEEE Transactions on Vehicular Technology,* vol. 71, no. 8, pp. 8341-8353, 2022, doi: 10.1109/tvt.2022.3175476.

[97] M. Jiang and S. Niu, "A High-Order Harmonic Compound Rotor Based Brushless Dual-Electrical-Port Dual-Mechanical-Port Machine," *IEEE Transactions on Industrial Electronics,* pp. 1-11, 2023, doi: 10.1109/tie.2023.3294574.

[98] X. Ren, D. Li, R. Qu, X. Han, and Z. Liang, "A Brushless Dual-Electrical-Port Dual-Mechanical-Port Machine With Integrated Winding Configuration," *IEEE Transactions on Industrial Electronics,* vol. 68, no. 4, pp. 3022-3032, 2021, doi: 10.1109/tie.2020.2978725.

[99] Z. Liang, X. Ren, D. Li, and R. Qu, "Analysis of Integrated Winding Configuration in Dual-Electrical-Port Machine," *IEEE Journal of Emerging and Selected Topics in Power Electronics,* vol. 10, no. 2, pp. 1891-1901, 2022, doi: 10.1109/jestpe.2021.3061695.

[100] X. Han *et al.*, "Modeling and Drive Control of a Brushless Dual-Mechanical-Port Machine With Integrated Winding," *IEEE Transactions on Industrial Electronics,* vol. 68, no. 3, pp. 2059-2071, 2021, doi: 10.1109/tie.2020.2972457.

[101] Y. Liu, S. Niu, and W. Fu, "Design of an electrical continuously variable transmission based wind energy conversion system," *IEEE Transactions on Industrial Electronics,* vol. 63, no. 11, pp. 6745-6755, 2016.

[102] Y. Wang, S. Niu, and W. Fu, "Electrical-Continuously Variable Transmission System Based on Doubly Fed Flux-Bidirectional Modulation," *IEEE Transactions on Industrial Electronics,* vol. 64, no. 4, pp. 2722-2731, 2017, doi: 10.1109/tie.2016.2637885.

[103] D. Li, R. Qu, X. Ren, and Y. Gao, "Brushless dual-electrical-port, dual mechanical port machines based on the flux modulation principle," in *2016 IEEE Energy Conversion Congress and Exposition (ECCE)*, 2016: IEEE, pp. 1-8.

[104] J. Bai, J. Liu, P. Zheng, and C. Tong, "Design and Analysis of a Magnetic-Field Modulated Brushless Double-Rotor Machine—Part I: Pole Pair Combination of Stator, PM Rotor and Magnetic Blocks," *IEEE Transactions on Industrial Electronics,* vol. 66, no. 4, pp. 2540-2549, 2019, doi: 10.1109/tie.2018.2842739.

[105] J. Bai, P. Zheng, C. Tong, Z. Song, and Q. Zhao, "Characteristic Analysis and Verification of the Magnetic-Field-Modulated Brushless Double-Rotor Machine," *IEEE Transactions on Industrial Electronics,* vol. 62, no. 7, pp. 4023-4033, 2015, doi: 10.1109/tie.2014.2381159.

[106] J. Bai, J. Liu, G. Liu, Y. Liu, and P. Zheng, "Investigation of the Power Factor of Magnetic-Field Modulated Brushless Double-Rotor Machine," *IEEE Transactions on Power*

Electronics, vol. 36, no. 1, pp. 423-432, 2021, doi: 10.1109/tpel.2020.2998188.

[107] H. Chen, A. M. El-Refaie, Y. Zuo, S. Cai, S. Xie, and C. H. Lee, "Evaluation of a Contra-Rotating Flux-Modulated Machine Featured With Dual Flux-Modulation for Wind Power Generation," *IEEE Transactions on Industrial Electronics,* vol. 69, no. 9, pp. 8770-8781, 2021.

[108] L. Cao, Y. Zhou, G. Yang, Y. He, S. Xie, and C. H. Lee, "Decoupling Analysis of Brushless Dual-Mechanical-Port Dual-Electrical-Port Machines," *IEEE Transactions on Industrial Electronics,* 2023.

[109] Y. Wang, S. Niu, W. Fu, and S. L. Ho, "A novel dual rotor flux-bidirectional-modulation machine for hybrid electrical vehicles," in *2016 IEEE Vehicle Power and Propulsion Conference (VPPC)*, 2016: IEEE, pp. 1-6.

[110] Y. Wang and S. Niu, "Optimal Design and control of Double-Rotor Flux-Bidirectional Modulation Machine," in *2019 22nd International Conference on Electrical Machines and Systems (ICEMS)*, 2019: IEEE, pp. 1-6.

[111] L. Qifang, S. Niu, H. Wu, and W. Fu, "Design and optimisation of a bidirectional flux modulation machine for AC and DC power supplies," *IET Renewable Power Generation,* vol. 15, no. 9, pp. 1996-2006, 2021, doi: 10.1049/rpg2.12122.

[112] Y. Mao, S. Niu, and Y. Yang, "A new parameter identification method of a dual-rotor flux-modulation machine based on an adaptive differential evolution algorithm," *IET Renewable Power Generation,* vol. 15, no. 9, pp. 1888-1897, 2021, doi: 10.1049/rpg2.12112.

[113] X. Han *et al.*, "Flexible Energy Conversion Control Strategy for Brushless Dual-Mechanical-Port Dual-Electrical-Port Machine in Hybrid Vehicles," *IEEE Transactions on Power Electronics,* vol. 34, no. 4, pp. 3910-3920, 2019, doi: 10.1109/tpel.2018.2854767.

[114] C. Tong, P. Zheng, Q. Wu, J. Bai, and Q. Zhao, "A brushless claw-pole double-rotor machine for power-split hybrid electric vehicles," *IEEE Transactions on Industrial Electronics,* vol. 61, no. 8, pp. 4295-4305, 2013.

[115] X. Ren, D. Li, R. Qu, W. Kong, X. Han, and T. Pei, "Analysis of spoke-type brushless dual-electrical-port dual-mechanical-port machine with decoupled windings," *IEEE Transactions on Industrial Electronics,* vol. 66, no. 8, pp. 6128-6140, 2018.

[116] X. Han *et al.*, "Modeling and drive control of a brushless dual-mechanical-port machine with integrated winding," *IEEE Transactions on Industrial Electronics,* vol. 68, no. 3, pp. 2059-2071, 2020.

[117] X. Zhao, S. Wang, S. Niu, W. Fu, and X. Zhang, "A Novel High-Order-Harmonic Winding

Design Method for Vernier Reluctance Machine With DC Coils Across Two Stator Teeth," *IEEE Transactions on Industrial Electronics,* vol. 69, no. 8, pp. 7696-7707, 2022, doi: 10.1109/tie.2021.3104589.

[118] M. Cheng, P. Han, and W. Hua, "General airgap field modulation theory for electrical machines," *IEEE Transactions on Industrial Electronics,* vol. 64, no. 8, pp. 6063-6074, 2017.

[119] H. Zhao, C. Liu, Z. Song, and S. Liu, "Design and Control of a New Compound Double-Rotor Electric Machine for Hybrid Propulsion System," *IEEE Transactions on Power Electronics,* vol. 37, no. 3, pp. 3283-3296, 2022, doi: 10.1109/tpel.2021.3111815.

[120] X. Ren, D. Li, R. Qu, Z. Yu, and Y. Gao, "Investigation of spoke array permanent magnet vernier machine with alternate flux bridges," *IEEE Transactions on Energy Conversion,* vol. 33, no. 4, pp. 2112-2121, 2018.

[121] Y. Zhang, D. Li, P. Yan, X. Ren, R. Qu, and J. Ma, "A High Torque Density Claw-Pole Permanent-Magnets Vernier Machine," *IEEE Journal of Emerging and Selected Topics in Power Electronics,* vol. 10, no. 2, pp. 1756-1765, 2021.

[122] S. A. Vargas, G. R. T. Esteves, P. M. Maçaira, B. Q. Bastos, F. L. C. Oliveira, and R. C. Souza, "Wind power generation: A review and a research agenda," *Journal of Cleaner Production,* vol. 218, pp. 850-870, 2019.

[123] H. Polinder, J. A. Ferreira, B. B. Jensen, A. B. Abrahamsen, K. Atallah, and R. A. McMahon, "Trends in wind turbine generator systems," *IEEE Journal of emerging and selected topics in power electronics,* vol. 1, no. 3, pp. 174-185, 2013.

[124] Y. Tang and L. Xu, "A flexible active and reactive power control strategy for a variable speed constant frequency generating system," *IEEE Transactions on power electronics,* vol. 10, no. 4, pp. 472-478, 1995.

[125] A. Broadway and L. Burbridge, "Self-cascaded machine: a low-speed motor or high-frequency brushless alternator," in *Proceedings of the Institution of Electrical Engineers*, 1970, vol. 117, no. 7: IET, pp. 1277-1290.

[126] Y. Wang, S. L. Ho, W. Fu, and J. Shen, "A novel brushless doubly fed generator for wind power generation," *IEEE transactions on magnetics,* vol. 48, no. 11, pp. 4172-4175, 2012.

[127] P. Han, M. Cheng, Y. Jiang, and Z. Chen, "Torque/power density optimization of a dual-stator brushless doubly-fed induction generator for wind power application," *IEEE Transactions on Industrial electronics,* vol. 64, no. 12, pp. 9864-9875, 2017.

[128] M. Afshar, A. Tabesh, M. Ebrahimi, and S. A. Khajehoddin, "Stator short-circuit fault

detection and location methods for brushless DFIMs using nested-loop rotor slot harmonics," *IEEE Transactions on Power Electronics,* vol. 35, no. 8, pp. 8559-8568, 2019.

[129] F. Barati, S. Shao, E. Abdi, H. Oraee, and R. McMahon, "Generalized vector model for the brushless doubly-fed machine with a nested-loop rotor," *IEEE Transactions on Industrial Electronics,* vol. 58, no. 6, pp. 2313-2321, 2010.

[130] A. Broadway, "Cageless induction machine," in *Proceedings of the Institution of Electrical Engineers*, 1971, vol. 118, no. 11: IET, pp. 1593-1600.

[131] P. Han, J. Zhang, and M. Cheng, "Analytical analysis and performance characterization of brushless doubly fed machines with multibarrier rotors," *IEEE Transactions on Industry Applications,* vol. 55, no. 6, pp. 5758-5767, 2019.

[132] J. Zhang, Y. Jiang, X. Hu, and S. Xu, "A Brushless Doubly Fed Generator Based on Permanent Magnet Field Modulation," *IEEE Transactions on Industrial Electronics,* vol. 67, no. 5, pp. 3505-3516, 2020, doi: 10.1109/tie.2019.2916381.

[133] H. Chen *et al.*, "A Permanent Magnet Brushless Doubly Fed Electric Machine for Variable-Speed Constant-Frequency Wind Turbines," *IEEE Transactions on Industrial Electronics,* vol. 70, no. 7, pp. 6663-6674, 2023, doi: 10.1109/tie.2022.3201306.

[134] F. Almeshqab and T. S. Ustun, "Lessons learned from rural electrification initiatives in developing countries: Insights for technical, social, financial and public policy aspects," *Renewable and Sustainable Energy Reviews,* vol. 102, pp. 35-53, 2019.

[135] T. M. Jahns, "Flux-weakening regime operation of an interior permanent-magnet synchronous motor drive," *IEEE Transactions on Industry Applications,* no. 4, pp. 681-689, 1987.

[136] T. M. Jahns, G. B. Kliman, and T. W. Neumann, "Interior permanent-magnet synchronous motors for adjustable-speed drives," *IEEE Transactions on Industry Applications,* no. 4, pp. 738-747, 1986.

[137] R. F. Schiferl and T. A. Lipo, "Power capability of salient pole permanent magnet synchronous motors in variable speed drive applications," *IEEE Transactions on Industry Applications,* vol. 26, no. 1, pp. 115-123, 1990.

[138] W. L. Soong, D. A. Staton, and T. J. Miller, "Design of a new axially-laminated interior permanent magnet motor," *IEEE Transactions on Industry Applications,* vol. 31, no. 2, pp. 358-367, 1995.

[139] Y. Amara, L. Vido, M. Gabsi, E. Hoang, A. H. B. Ahmed, and M. Lecrivain, "Hybrid excitation synchronous machines: Energy-efficient solution for vehicles propulsion," *IEEE*

Transactions on vehicular technology, vol. 58, no. 5, pp. 2137-2149, 2008.

[140] Y. Amara, S. Hlioui, R. Belfkira, G. Barakat, and M. Gabsi, "Comparison of open circuit flux control capability of a series double excitation machine and a parallel double excitation machine," *IEEE Transactions on Vehicular Technology,* vol. 60, no. 9, pp. 4194-4207, 2011.

[141] Y. Wang and Z. Deng, "Parallel hybrid excitation machines and their control schemes for DC generation system," *IET electric power applications,* vol. 6, no. 9, pp. 669-680, 2012.

[142] J. S. Hsu, "Direct control of air-gap flux in permanent-magnet machines," *IEEE Transactions on Energy Conversion,* vol. 15, no. 4, pp. 361-365, 2000.

[143] V. Ostovic, "Memory motors," *IEEE Industry Applications Magazine,* vol. 9, no. 1, pp. 52-61, 2003.

[144] C. Yu, K. Chau, X. Liu, and J. Jiang, "A flux-mnemonic permanent magnet brushless motor for electric vehicles," *Journal of Applied Physics,* vol. 103, no. 7, p. 07F103, 2008.

[145] J. Cekani, F. G. Capponi, G. De Donato, and F. Caricchi, "Mechanical flux weakening methods for the achievement of a very wide constant power speed range in automotive applications," *IEEE Journal of Emerging and Selected Topics in Power Electronics,* vol. 10, no. 3, pp. 3443-3458, 2021.

[146] N. Elloumi, M. Bortolozzi, A. Masmoudi, M. Mezzarobba, M. Olivo, and A. Tessarolo, "Numerical and analytical approaches to the modeling of a spoke type IPM machine with enhanced flux weakening capability," *IEEE Transactions on Industry Applications,* vol. 55, no. 5, pp. 4702-4714, 2019.

[147] F. Caricchi, F. Crescimbini, F. G. Capponi, and L. Solero, "Permanent-magnet, direct-drive, starter/alternator machine with weakened flux linkage for constant-power operation over extremely wide speed range," in *Conference Record of the 2001 IEEE Industry Applications Conference. 36th IAS Annual Meeting (Cat. No. 01CH37248)*, 2001, vol. 3: IEEE, pp. 1626-1633.

[148] Z. Q. Zhu, M. Al-Ani, X. Liu, and B. Lee, "A mechanical flux weakening method for switched flux permanent magnet machines," *IEEE Transactions on Energy Conversion,* vol. 30, no. 2, pp. 806-815, 2014.

[149] F. G. Capponi, R. Terrigi, F. Caricchi, and L. Del Ferraro, "Active output voltage regulation for an ironless axial-flux PM automotive alternator with electromechanical flux weakening," *IEEE Transactions on Industry Applications,* vol. 45, no. 5, pp. 1785-1793, 2009.

[150] M. C. Kulan, N. J. Baker, and S. Turvey, "Split rotor concept for permanent magnet electrical machines," in *2019 IEEE International Electric Machines & Drives Conference (IEMDC)*, 2019: IEEE, pp. 700-707.

[151] Y. Wang, S. Niu, and W. Fu, "A Novel Dual-Rotor Bidirectional Flux-Modulation PM Generator for Stand-Alone DC Power Supply," *IEEE Transactions on Industrial Electronics,* vol. 66, no. 1, pp. 818-828, 2019, doi: 10.1109/tie.2018.2849970.

[152] B. Cheng, G. Pan, and Z. Mao, "An Axial Flux Double-Rotor Counter-Rotating Permanent Magnet Machine for Underwater Vehicles," presented at the 2019 IEEE 8th International Conference on Advanced Power System Automation and Protection (APAP), 2019.

[153] S. R. Macminn and T. M. Jahns, "Control techniques for improved high-speed performance of interior PM synchronous motor drives," presented at the IEEE Trans. Ind. Applicat., 1991.

[154] W. L. Soong and T. J. Miller, "Field-weakening performance of brushless synchronous AC motor drives," presented at the Proc. IEE-Elect. Power Applicat., Sept./Oct. , 1994.

[155] Y. Sozer and D. A. Torrey, "Adaptive flux weakening control of permanent magnet synchronous motor," presented at the Conf. Rec. IEEE-IAS Annu. Meeting, 1998.

[156] J. A. Tapia, F. Leonardi, and T. A. Lipo, "Consequent-pole permanent-magnet machine with extended field-weakening capability," *IEEE Transactions on Industry Applications,* vol. 39, no. 6, pp. 1704-1709, 2003, doi: 10.1109/tia.2003.818993.

[157] M. Aydin, S. Huang, and T. A. Lipo, "A new axial flux surface mounted permanent magnet machine capable of field control," presented at the 37th IAS Annual Meeting (Cat. No.02CH37344), 2002.

[158] M. Aydin, S. Huang, and T. A. Lipo, "Design, Analysis, and Control of a Hybrid Field-Controlled Axial-Flux Permanent-Magnet Motor," *IEEE Transactions on Industrial Electronics,* vol. 57, no. 1, pp. 78-87, 2010, doi: 10.1109/tie.2009.2028294.

[159] T. W. Ching, K. T. Chau, and W. Li, "Power Factor Improvement of a Linear Vernier Permanent-Magnet Machine Using Auxiliary DC Field Excitation," *IEEE Transactions on Magnetics,* vol. 52, no. 7, pp. 1-4, 2016, doi: 10.1109/tmag.2016.2524533.

[160] W. Li, T. W. Ching, and K. T. Chau, "A New High-Temperature Superconducting Vernier Permanent-Magnet Machine for Wind Turbines," *IEEE Transactions on Applied Superconductivity,* vol. 27, no. 4, pp. 1-5, 2017, doi: 10.1109/tasc.2017.2669138.

[161] Z. Zhu, B. Lee, and X. Liu, "Integrated Field and Armature Current Control Strategy for Variable Flux Reluctance Machine using Open Winding," *IEEE Transactions on Industry*

Applications, pp. 1-1, 2015, doi: 10.1109/tia.2015.2490041.

[162] Z. Q. Zhu and B. Lee, "Integrated Field and Armature Current Control for Dual Three-Phase Variable Flux Reluctance Machine Drives," *IEEE Transactions on Energy Conversion,* vol. 32, no. 2, pp. 447-457, 2017, doi: 10.1109/tec.2016.2637311.

[163] T. Sheng and S. Niu, "A Novel Zero-Sequence-Current-Based Dual-Stator Biased-Flux Machine," *IEEE Transactions on Energy Conversion,* vol. 33, no. 4, pp. 1934-1942, 2018, doi: 10.1109/tec.2018.2843775.

[164] M. Jiang and S. Niu, "Novel Mechanical Flux-Weakening Design of a Spoke-Type Permanent Magnet Generator for Stand-Alone Power Supply," *Applied Sciences,* vol. 13, no. 4, 2023, doi: 10.3390/app13042689.